The Role of Advection in Early Diagenesis: From Seeps to Nearshore and Coastal Margin Sediments

by

Jurjen Rooze

(Under the Direction of Christof Meile)

Abstract

This dissertation investigates the effect of various modes of advective transport on early diagenesis in a diverse array of marine environments using reaction-transport models.

In cold seep environments, variation in pressure over a tidal cycle can compress gas in the sediment, leading to peak and throughs in the emission of gas and efflux of porewater. The induced oscillatory flow can be significant compared to the mean flow velocities, depending on environmental parameters. Over longer timescales, we constrain porewater flow using ^{226}Ra as a novel tracer, with inferred velocities ranging between 0 and 0.25 m y^{-1}. Further analyses showed that the flow estimates are sensitive to both the sediment tortuosity and the natural variability in sediment permeability.

In coastal sediments, porewater movement is often driven by the activity of burrowing organisms, and we assess the effect of bioirrigation on sediment nitrogen cycling and isotopic signatures. The results indicate that the N isotope effect is strongly dependent on the redox conditions in the sediment. The main factors controlling redox conditions are bioirrigation and the deposition of organic matter. By using correlations between these two parameters, the global average N isotope effect of benthic fixed N removal is estimated to be ~ -3‰.

In deltaic environments, movement relative to the sediment surface can be driven by the deposition of new material. The impact of changing sedimentation on early diagenetic processes over the last 27,400 years was studied in the Zambezi delta. ^{14}C-dating of the sediment core shows that sea-level rise since the last glacial maximum have generally decreased sedimentation rates at the study site. A model reproduces measured porewater profiles and solid-phase data. Changes in organic matter deposition and burial velocities controlled the depth of the sulfate-methane transition zone, and the simulations show how this is recorded by pyrite formation. The study emphasizes the importance of legacy effects, as methane that is oxidized today has been formed 1000s of years ago.

Index words: [Early Diagenesis, Reaction-Transport Modeling, Advection, Marine Sediments]

The Role of Advection in Early Diagenesis: From Seeps to Nearshore and Coastal Margin Sediments

by

Jurjen Rooze

M.S., Utrecht University, The Netherlands, 2013
B.AS., Stenden University of Applied Sciences, The Netherlands, 2011

A Dissertation Submitted to the Graduate Faculty of the
University of Georgia in Partial Fulfillment of the Requirements for the Degree.

Doctor of Philosophy

Athens, Georgia

2020

The Role of Advection in Early Diagenesis: From Seeps to Nearshore and Coastal Margin Sediments

by

Jurjen Rooze

Major Professor:	Christof Meile
Committee:	Renato Castelao
	Daniela Di Iorio
	Samantha Joye
	Laura Lapham

Electronic Version Approved:

Ron Walcott
Interim Dean of the Graduate School
The University of Georgia
August 2020

Acknowledgments

I would like to thank to the committee members, Renato Castelao, Daniela Di Iorio, Mandy Joye, and Laura Lapham for their support and assistance for during my PhD and especially to my adviser, Christof Meile, for his patience, motivation, and guidance in conducting research and writing this dissertation.

I greatly appreciate the contributions of Leigha and Rick Peterson to the 3rd chapter for which they went on a cruise, measured the radium profiles, and helped revising the manuscript. Also my thanks goes to the Joye research group for sharing their porosity data. With Caroline Johansen and Ian MacDonald I had many helpful conversations about cold seeps in the Gulf of Mexico. My PhD has been supported by ECOGIG led by S. Joye, and was funded by the Gulf of Mexico Research Initiative (GoMRI).

I would like to thank our colleagues from Ifremer for the collaboration resulting in the 5th chapter about the Zambezi. A large part of the work and writing was carried out by Mark Zindorf, and we share an equal contribution. Lucie Pastor led the research, as part of the PAMELA (Passive Margin Exploration Laboratories) project. Gwenael Jouet dated the sediment cores and provided the age model. Christophe Brandily provided pore water data. The chapter also benefitted from contributions of Christian März and Robert Newton from the University of Leeds.

I am indebted to my labmates, especially my David Miklesh with whom I shared my office, and my current labmates Kadir Biçe, Xiaojia He, Heewon Jung, for good scientific discussions and also being great friends. I owe thanks to David de Laat for helping me with math problems and visiting me in the United States, and Mathilde Hagens for many conversations. Finally, I would like to thank my family for the time we spent in Europe during holidays.

Contents

List of Figures

List of Tables

Chapter 1

Introduction

Early diagenesis refers to the chemical, physical, and biological processes that occur in newly deposited sediment (Berner 1980). It plays an important role in controlling fluxes across the largest interface in the world — the seafloor. Sediments act as sinks for various chemicals in the ocean, such as oxidants, organic matter, and other particulate material; but can also serve as a source, for instance, of nutrients released during organic matter remineralization (Sarmiento and Gruber 2006), alkalinity produced in anaerobic metabolism (e.g. Oueslati et al. 2019), venting of gas and oil from cold seeps (Suess, 2010), or metals emitted at hydrothermal vents (Conway and John 2014). Research on the mechanisms and factors that control the direction and magnitude of these fluxes not only helps to gain a better fundamental understanding of the ocean biogeochemical cycles (Sarmiento and Gruber 2006), but is also needed for assessing the severity of pollution issues and time-scales for natural mitigation (e.g. Cerco and Cole 1993; Vanderborght et al. 2007; Palastanga et al. 2011; Carstensen et al. 2014).

Sediment cores are routinely collected during research cruises to gather data on early diagenesis. Prior to the determination of chemical and physical properties, they are typically sliced parallel to the seafloor in layers to obtain one-dimensional depth-profiles. From these profiles, estimates can be made of chemical diffusive fluxes and reaction rates, and the burial velocity can be determined from radiotracers. Reaction-transport models can help in quantifying reaction rates and the coupling between biogeochemical reaction pathways. The latter can make pen-and-paper estimates nearly impossible through strongly nonlinear behavior, which can be induced by re-oxidation of reduced metabolites formed during organic matter remineralization (e.g. nitrification, sulfide and dissolved iron oxidation) and mineral precipitation/dissolution reactions, or due to cryptic chemical cycles in which reactants or products are quickly recycled (e.g. Holmkvist et al. 2011; Treude et al. 2014; Xiao et al. 2018; Zindorf et al. 2019).

To match model output with measured profiles, model parameters are fitted. As many rate parameters are poorly constrained (Wang and Van Cappellen 1996; Regnier et al. 2011;

Arndt et al. 2013), parameter sensitivity analysis (sweeping parameter values in consecutive model runs) forms a powerful, although not necessarily conclusive, validation procedure to assess the robustness of model outcomes (Saltelli 1999; Omlin et al. 2001). Sensitivity analysis also greatly increase the scientific value of models by serving as a tool to assess which environmental parameters have the strongest effect on early diagenetic processes, to make inferences about the conditions at locations subject to different environmental conditions, and to interweave often contrasting observations in an overarching theoretical framework. The iterative cycles of experiments, model adaptations, drawing conclusions and making new predictions drive scientific progress.

In most marine sediments, biogeochemistry is driven primarily by the remineralization of detritus (dead particulate organic matter), which were produced in the euphotic zone. The quality of organic matter deposited upon the sediments depends on the type of biological source (e.g. plankton species, fecal material) as well as on the extent of decay while it sinks from the upper ocean to the bottom (Martin et al. 1987; Middelburg et al. 1997; Hartnett and Devol 2003). As a result, remineralization rates are orders of magnitude higher in coastal marine sediments than in the deep-sea. The most widely used models for organic matter remineralization in marine sediments (Arndt et al. 2013) assume that microbes use up oxidants in sequence of the free Gibbs energy yield (Jørgensen 2000), leading to redox stratification in which zones of oxygen, nitrate, metal oxide, and sulfate respiration are layered on top of each other, followed by a zone of fermentative decay (including methanogenesis). This redox stratification is commonly observed in deep-sea sediments (Froelich et al. 1979), where benthic animals tend to be smaller and less abundant due to lower availability of food (Künitzer et al. 1992), leading to less reworking of sediments by infaunal activities (also referred to as bioturbation; Boudreau 1994; Meysman et al. 2006a). Mineralization rates in these settings depend primarily on organic matter loading and reactivity, sedimentation rate, and bioturbation, which can still be a significant transport process, as sedimentation rates also negatively correlate with water-depth (Middelburg et al. 1997). In coastal sediments, burrowing animals (e.g. polychaetes, mollusca, shrimps) need to funnel oxic seawater deeper into the sediment to be able to breath and flush out toxic metabolites (bioirrigation), whereby they disrupt the vertical redox zonation and create lateral concentration gradients. These settings are subjected to higher sedimentation rates, organic matter loading and reactivity, and more intense bioturbation.

The distribution of solutes and solids in marine sediments is typically described by (Boudreau 1997):

$$\begin{aligned} \frac{\partial \phi C}{\partial t} &= \frac{\partial}{\partial z}\left[\phi\left(\frac{D_{\mathrm{mol}}}{\theta^2}+D_b\right)\frac{\partial C}{\partial z}-\phi u C\right]+ \\ &\quad B(C_0-C)+R \qquad (1.1) \\ \frac{\partial (1-\phi) C}{\partial t} &= \frac{\partial}{\partial z}\left[(1-\phi)D_b\frac{\partial C}{\partial z}-(1-\phi)uC\right]+R \qquad (1.2) \end{aligned}$$

In these equations the left-hand side represents mass balances, $-D_{\mathrm{mol}}\,\partial C/\partial z$ is the diffusive flux which is driven by the concentration gradient. Bioturbation is represented as a diffusive process, describing sediment mixing by burrowing animals as a random process similar to the random motion of molecules leading to chemical diffusion. The bioturbation coefficient D_b decreases with depth, reflecting that most burrowing activity occurs typically in the upper 10 cm (Boudreau 1994). As written (D_b outside the derivative of the concentration gradient) it accounts for intraphase mixing, meaning that bioturbation preserves the porosity gradient and does not cause interphase mixing between the solid matrix and porewater (Mulsow et al. 1998; Meysman et al. 2005a). Bioturbation coefficients are typically an order of magnitude lower than aqueous diffusion coefficients, and therefore often omitted for solutes. Burial velocity - reflecting both the effect of the accumulation of new material at the sediment-water interface, the formation and dissolution of solid phases, and compaction is described by ϕu and is (similar to bioturbation) more important for solids than solutes that react near the sediment-water interface. The porosity is written within the temporal derivative on the left-hand side to account for non-steady-state compaction and solid-phase reactions, and also within the spatial derivative to account for the flux divergence (Jourabchi et al. 2010), which can have a significant effect on the distribution of solids in high porosity ocean sediments. Bioirrigation is represented by a non-local exchange term, with a bioirrigation coefficient B (eq. 3.7) that also decreases with depth (Meile et al. 2001). The term R accounts for all the reactions. A fairly comprehensive reaction network commonly adopted in modeling studies can be found in Wang and Van Cappellen (1996). Descriptions of the underlying abiotic and microbial reaction pathways can be found in Canfield et al. (2005).

The one-dimensional description of early diagenesis (eqns. 3.7, 1.2) has been used extensively since the 90s (e.g. Wang and Van Cappellen 1996; Van Cappellen and Wang 1996; Boudreau 1997) to describe bulk processes representative of large areas of the seafloor, such as integrated ocean benthic fluxes (e.g., Soetaert et al. 1996; Middelburg et al. 1996; Thullner et al. 2009), under the assumption of predominant vertical transport and redox stratification. The model remains popular, partly because codes to solve the equations numerically have become well established and are relatively easy to adapt and run (e.g. Soetaert and Meysman 2012; Steefel et al. 2015). However, due to the relative simplicity of the approach, such models are unable to account for a spatial heterogeneity or a more refined view of microbial activity that deviates from average bulk energetic conditions. This can emerge due to the use of different organic electron donors, kinetic effects (e.g. microbes oxidize methane faster with sulfate than metal oxides, despite the former reaction pathway being thermodynamically less favorable; Beal et al. 2009; Rooze et al. 2016) or due to a more detailed account of thermodynamics of minerals and intracellular microbial processes (Postma and Jakobsen 1996; Jakobsen and Postma 1999; Jin and Bethke 2005).

Models for multidimensional flow have been developed to simulate more accurately the effects of bioirrigation (Meile et al. 2003; Meysman et al. 2005b) and wave-induced advection

(Shum 1992; Cook et al. 2006; Cardenas et al. 2008). Following Darcy's law, flow driven by pressure gradients is more readily induced in permeable sands (Hüttel et al. 2003), which cover approximately 70% of the continental shelves (Emery 1968). The advective velocities associated with these processes can exceed sediment burial by multiple orders of magnitude (Table 1.1), which is reflected in the estimation that permeable sediments filter a water volume of the ocean at a time-scale of 3,000 years (Santos et al. 2012). The burrowing activities of sediment infauna can induce strong lateral heterogeneity in chemical distributions resulting from injection of oxic water into otherwise anoxic layers and lateral redox gradients driving diffusion of oxidants from burrows to adjacent anoxic porewater (Aller 2001). Similarly, wave-induced advection affected by heterogeneous anisotropy of sediment permeability can lead to complex flow patterns (Rocha 2008). Concentration fields measured with microprobes (Stockdale et al. 2009) and under in-situ flow conditions (Polerecky et al. 2005; Rocha 2008) can be used to validate multidimensional models. Continuous temporal data of bioirrigation can be obtained with optodes from aquaria with live animals (Volkenborn et al. 2012), while benthic chambers with stirrers and benthic chambers in landers have been employed to study the effects of wave-induced advection (Booij et al. 1991; Glud et al. 1996; Janssen et al. 2005). Sediment-bottom water exchange fluxes of solutes can be measured in the field with the eddy covariance technique (Berg et al. 2017).

Multidimensional models have also been developed to simulate advective flow driven by other mechanisms. Hydrothermal vent and cold seep environments can exhibit complex flow patterns with high velocities (Table 1.1). At hydrothermal vents hot water escapes from the deep subsurface through fissures, leading to geothermal circulation. Coupled heat transport, fluid flow, and chemistry have been modeled (Lowell and Germanovich 2004; LaRowe et al. 2014; Larson et al. 2015). Cold seeps refer to locations with natural upwelling of water that is not very hot (Suess 2010). At these sites free gas may be present leading to multiphase flow (see Chapter 2). Gas hydrate formation can constitute a negative feedback to flow (see second chapter and references therein). When the pore fluid pressure gradient exceeds lithostatic pressure mud volcanoes can emerge (Cathles et al. 2010). New discoveries continue to stimulate the development of novel reaction-transport models. Examples include the occurrence of spatially separated redox half-reaction conducted through bacterial filaments and minerals (Kato et al. 2012; Pfeffer et al. 2012; Meysman et al. 2015), bubble irrigation (O'Hara et al. 1995; Haeckel et al. 2007), or the integration of omics data into reaction-transport models, which can be expected to drive innovation in the future (Meile et al. 2001).

1.1 Dissertation outline

The overarching theme of this dissertation is the study of early diagenetic processes in the presence of various forms of advective transport: multiphase flow (chapter 2), porewater flow

Table 1.1: Advective flow mechanisms and velocities in marine sediments

Process	Typical velocity (m/y)
Sedimentation/burial[S]	
Coastal ($\sim$ 100 m water-depth)	$4.0 \cdot 10^{-3}$
Margin ($\sim$ 1000 m)	$1.6 \cdot 10^{-3}$
Deep-Sea ($\sim$ 4000 m)	$8.0 \cdot 10^{-5}$
Bioirrigation porewater flow[B]	
Coastal	$1.4 \cdot 10$
Margin	5.6
Deep-Sea	0
Wave-induced advection[W]	
Coastal sandy sediments	$3 \cdot 10$
Cold seep environments	
Porewater flow tracer estimates[P]	0.1
Porewater flux meters[P]	1.0
Gas flow[G]	$2.5 \cdot 10^3$
Oil flow[O]	$2.5 \cdot 10$
Hydrothermal vents	$3 \cdot 10^7$

Sources: B = Based on method described for equation 4.13 in chapter 4, G = see chapter 2, H = Germanovich et al. 2015, O = based on 100 times lower volumetric flux of oil compared to gas (Leifer and Wilson 2004), P = see the introduction of chapter 3, S = Middelburg et al. (1997), W = Janssen et al. (2005).

(chapter 3), bioirrigation (chapter 4), and transient burial velocities over millennial timescales (chapter 5). The importance of advection relative to diffusion can be expressed with the Péclet number (Pe = qL/D, where q is the advective velocity, L is the characteristic length-scale, and D is the diffusivity). Surficial marine sediment with burial as the dominant advective transport mechanism are characterized by low Pe numbers for solutes that react with organic matter in the upper sediment highlighting the importance of diffusion. Impermeable sediment without burrowing macrofauna and deep-sea sediments represent low Pe environments. In such settings where diffusion is the dominant solute transport process, diffusion can average out lateral concentration gradients and let vertical gradients persist, supporting a 1D representation of early diagenesis In contrast, bioirrigation and wave-induced advection are associated with higher advective velocities than burial (Table 1.1; Hüttel et al. 2003), corresponding to higher Pe numbers; cold seep areas and hydrothermal vents with dominant upward flow from the deeper subsurface are also high Pe environments. In high Pe environments advection will average out concentration gradients along the flow path, but generate larger lateral heterogeneity (Jung and Meile 2019), possibly necessitating a two- or three-dimensional model setup.

Chapter 2: Modeling Tidal Flow Patterns at Cold Vents

This chapter analyzes gas and water transport in flow conduits, as for example in seeps of the Gulf of Mexico. It gives a background description of the physics of multiphase flow and the implementation in numerical models. Then a model is developed to analyze flow patterns in cold seeps subject to tidal pressure oscillations at the water-sediment interface. The key questions it seeks to address are 1) why tidal signals in gas release are observed at some but not all seeps, and 2) how do tides affect porewater flow.

Chapter 3: Porewater flow patterns in surficial cold seep sediments inferred from conservative tracer profiles and early diagenetic modeling

In this chapter the focus is on porewater flow at cold seeps, delivering reduced substances from the deeper subsurface, thereby forming the basis for diverse seep communities. In brine seeps, porewater flow has often been constrained by fitting vertical porewater chloride profiles with a one-dimensional, steady-state model (Lapham et al. 2008a; Vanneste et al. 2011). In this study, for the first time, we applied this approach to ^{226}Ra profiles retrieved from non-brine seeps. In addition, we examined the effect of spatiotemporal variable flow at seeps on tracer distributions. To determine magnitude and variability of seepage and to identify the factors controlling it, reaction-transport simulations of cold seep surface sediments were

carried out. We analyzed particularly the effect of solid formation on the spatiotemporal evolution of flow in sediments with randomness in the permeability field.

Chapter 4: The effect of redox conditions and bioirrigation on nitrogen isotope fractionation in marine sediments

In this chapter, flow around a lugworm burrow in marine sediment is studied. We couple flow to a reaction network with the goal to simulate the N isotope effect of benthic N_2 production. Fixed N in the form of ammonium, organic nitrogen, and nitrate is an important nutrient for primary producers, and its scarcity limits the ocean's primary productivity. Microbial pathways adding (nitrogen fixation) or removing (denitrification and anaerobic ammonium oxidation) fixed N have distinct N isotope signatures that can be used to constrain the magnitude of the processes (Brandes and Devol 2002; Montoya 2008; Stüeken et al. 2016; Gu et al. 2017; Guo et al. 2020). However, the expression of isotope effects also strongly depends on the open/closed nature of the environment (Jørgensen 1979). The water column forms generally a more open system with fresh supply of nitrate that allows for high expression, whereas sediments represent more closed conditions, limiting expression of the N isotope effect through local depletion of light isotopes in the reactant pool (Brandes and Devol 2002; Deutsch et al. 2004).

Previous modeling studies that integrated measured N isotope data focused on diffusive transport, without bioirrigation (Brandes and Devol 1997; Lehmann et al. 2004; Lehmann et al. 2007, Alkhatib et al. 2012), despite most of the ocean fixed N removal occurring in coastal environments (Middelburg et al. 1996), where wave-induced advection and bioirrigation play important roles. Kessler et al. (2014) have studied the effect of wave-induced advection. Our leading hypothesis was that bioirrigation could enhance the N isotope effect through the injection of water that enhances the fluid exchange between sediment and overlying water.

Chapter 5: The evolution of early diagenetic processes and sediment biogeochemical signatures following postglacial sea-level rise at the Mozambique margin

The large amounts of sediment delivered to the ocean by rivers make continental margins near river mouths critical environments for the deposition, mineralization and burial of organic matter. We analyzed sediment offshore the Zambezi, the largest river in East Africa flowing into the Indian Ocean, to assess the effect of early diagenesis on the sedimentary record and hence preserved oceanographic and climatic signals. A sediment core of ~ 30 m length drilled offshore the Zambezi at 550 m water depth shows that since the last glacial maximum, sedimentation rates as well as organic matter and iron oxide loading have been

strongly affected by changes in seawater level. With $\Delta^{14}C$ dating the sedimentation rates were determined. Geochemical analysis of pyrite indicated that the sulfate-methane transition zone had moved over time, forming distinct peaks.

In this chapter, which is currently under review (Rooze et al. submitted), we reconstruct the diagenetic history of the last $\sim$ 27 ky with a reaction-transport model. We focus on iron and sulfur cycling in response to displacements of the sulfate-methane transition zone. The study emphasizes the importance of legacy effects, as the complex interplay between climate-driven perturbations in sediment loading and in-situ authigenic mineral formation still affect the biogeochemical processes occurring today.

Chapter 2

Modeling Tidal Gas and Water Flow Patterns at Cold Vents

2.1 Introduction

Since hydrocarbon cold seeps were first discovered in the early 1980s (Paull et al. 1984) much research effort has been dedicated to quantifying exchange fluxes between the sediment and the overlying water. To date flux budgets of oil, gas, and water remain poorly constrained (National Research Council 2003, Johansen et al. 2020). Measuring fluxes over prolonged periods of time is complicated by the limited life-span of batteries powering instruments mounted on the seafloor, the release of mud from vents and earthquakes dislocating instruments, and migration, genesis or ending of focal seepage points within a seep field. Continuous records of gas and water fluxes at the sediment-water interface indicate high variability (see references in Table 2.1). Episodic flow can be triggered by earthquakes (Lapham et al. 2008b; Fischer et al. 2013) and gas hydrate decomposition (MacDonald et al. 1994), while seasonal oceanographic conditions (Römer et al. 2016) and glacial-interglacial eustatic fluctuations may reposition the gas hydrate stability zone and affect flow on longer time-scales (Roberts and Carney 1997; Liu and Flemings 2009; Crémière et al. 2016).

Significant correlations have been observed between gas fluxes and changes in hydrostatic pressure forced by swells and tides (Table 2.1), and several hypotheses have been proposed to explain the relationship. Early studies at cold seeps suggested that capillary activation in itself can explain the patterns, as at low tides the critical entry pressure can be exceeded allowing for gas migration (Boles et al. 2001; Liu and Flemings 2009; Leifer and Boles, 2005a). However, Scandella (2010) argued that the pore size in low permeability (muds and siliciclastic) sediments is too small to allow for capillary invasion, so that gas invasion needs to be preceded by the deformation of sediment (Jain and Juanes 2009; Choi et al. 2011). To create or expand a fracture, the fluid pressure needs to exceed the sum of sediment tensile strength and effective stress (Van Kessel and Van Kesteren 2002; Johnson et al. 2002;

Boudreau et al. 2005; Katsman 2015). As sediment failure depends on the confining effective stress, which decreases with decreasing hydrostatic pressure, sediment dilation is triggered at times of lower hydrostatic pressure when the buildup of gas pressure is sufficiently slow (Scandella et al. 2011; Algar et al. 2011; Liu et al. 2016; Katsman 2019). This provides a mechanism that can explain intermittent tidal gas release observed at several pockmarks and seeps (Sirhan et al. 2019). As the effective stress depends on hydrostatic pressure and thus water-depth, this mechanism may be more relevant in sediments of lakes and coastal areas than in deep-sea seeps (Sirhan et al. 2019).

At vents and mud volcanoes (with faster flow compared to seeps) only a small fraction of the gas dissolves (Wang et al. 1998) or is oxidized in the upper sediment (Boetius and Wenzhöfer 2013), thus preventing large decline of the buoyant force of rising gas bubbles and their entrapment in soft sediments. Volumetric gas fluxes can be on the order of 5 L min^{-1} (e.g. Torres et al. 1998 at 800 m water-depth), and be uninterrupted but variable over long periods of time (months to years, e.g. Johansen et al. 2017). High fluxes of gas indicate the presence of a flow conduit, i.e. an interconnected fracture network (Van Kessel and Van Kesteren 2002). Seismic studies have shown that gas migration is primarily facilitated through major faults and conduits at cold seeps connected to deeper geologic formations (Clennell et al. 2000; Talukder 2012; Diercks et al. 2019), for instance, gas and oil reservoirs. To form oil and gas in reservoirs there must be a seal, so that the fluids cannot escape and pressures can accumulate. Caprocks above marine reservoirs are most often shales (finely stratified consolidated mud and clay). At the bottom of a gas pocket porewater and gas may be at hydrostatic pressure or overpressurized due to compaction and applied stress from the overburden. Higher up in the gas pocket the gas is overpressurized due to higher buoyancy of gas compared to water. New fractures are most likely to be formed at the most elevated tip of a gas pocket, as it has the highest overpressure (Cathles et al. 2010). A fractured caprock is called a chimney (Sun et al. 2012), and allows upward migration of hydrocarbons. When fluids start to flow through the chimney a pipe is formed in the consolidated sediment. Cathles et al. (2010) presented a simple analytical model for the genesis of a pipe, assuming that the main resistance is the displacement of water at its top (viscosity of gas is negligible compared to water) and take the buoyancy of gas as the driving force ($\sigma = [\rho_g - \rho_w]gH$). When the fluid pressure gradient exceeds the lithostatic gradient, sediments are mobilized, and a mud volcano is formed. A pipe may extend to seafloor or it can lead distributed unfocused flow if unlithified sediments lose their cohesion (Gay et al. 2012).

Table 2.1: Observations of water, gas and oil flow.

Site (water-depth)	Method	Dynamic Pattern	Reference
Water flow			
			Continued on next page

Table 2.1 – continued from previous page

Site	Method	Dynamic Pattern	Reference
Hydrate Ridge, Cascadia (600 - 800 m)	Flux meter, 28h resolution	Possibly tidal	Tryon et al. (1999)
	Flux meter, 5h resolution	Tidal at some locations	Tryon and Brown (2001)
	Flux meter, 5 min resolution	Tidal at some locations	Linke et al. (1999)
Bush Hill, Gulf of Mexico (540 m)	Flux meter, 7d resolution	Not tidal, changes in flow attributed to gas hydrate dynamics	Solomon et al. (2008)
	Flux meter, >1d resolution	Not tidal; changes due to major gas expulsion event	Tryon and Brown (2004)
Gas flow			
GC600 (1200 m), MC118 (800 m), Gulf of Mexico	Camera	Tidal correlation only at MC118, but with high flow at high tide	Johansen et al. (2017)
MC118 (880 m)	Pore-fluid array sampler	Earthquake	Lapham et al. (2008b)
Doggerbank, North Sea (< 40 m)	Seismic reflection, sampling above seep	Tidally driven	Groot et al. (2019)
North Sea (abandoned well; 100 m)	Hydroacoustics	Tidally driven, but with high flow at high tide	Wiggins et al. (2015)
Northern Cascadia, offshore Vancouver Island (1250 m)	Hydroacoustics	Tidally driven	Römer et al. (2016)
Sea of Marmara, Turkey (350 - 1250 m)	Hydroacoustics	Not tidal	Bayrakci et al. (2014)
Coal Oil Point area, Santa Barbara Channel, California (15 - 20 m)	Tents, hourly resolution for 9 months	Tidally driven	Boles et al. (2001)
	Tents, 3 sec resolution, records 2 h	Ocean swells (1 - 4 m amplitude) drive flow oscillations	Leifer and Boles (2005)
South China Sea (< 50 m)	Gas flux measuring device	Tidally driven	Di et al. (2014)
Convergent margin off Pakistan (2,831 - 2,861 m)	Geochemical and seismic reflection data	Earthquake	Fischer et al. (2013)
Gas and sluggish oil flow			

Continued on next page

Table 2.1 – continued from previous page

Site	Method	Dynamic Pattern	Reference
Coal Oil Point (< 80 m)		Tidally driven (oil)	Mikolaj and Ampaya (1973)
Nearshore Summerland, California (abandoned oil well; 5 m)	Tents	Tidally driven (oil and gas)	Leifer and Wilson (2007)
GC600 (1200 m), MC118 (800 m), Gulf of Mexico	Camera	No significant pattern (oil and gas)	Johansen et al. (2017)

Oscillations in hydrostatic pressure during a tidal cycle are too small to significantly compress the sediment matrix (Wang et al. 1998), leaving the apertures of fractures in flow conduits unaffected. Assuming a static sediment matrix, we study the interaction between gas compression and stress at the seafloor on gas and water flow patterns as a mechanism to explain tidal signals in gas emissions from seeps connected to thermogenic reservoirs. Previous work has shown that compression can increase the gas mobility by allowing bubbles to pass through narrower pore throats (Rosenberry et al. 2006), but also decrease the mobility as it lowers the gas buoyancy (Clayton and Hay 1994; Algar et al. 2011). We model the effect of compression of gas on multiphase flow of continuous water and gas phases for larger volumes over a depth interval of 100 m, focusing on total gas volume changes.

2.2 Methods

The model describes the movement of gas and water in a flow conduit that connects the deeper sediment with the ocean floor, with a stress forced by a semidiurnal tidal cycle (Fig. 2.1). In marine sediments, stress exerted on the top of the sediment propagates as a p-wave with velocities on the order of kilometers per second (Schumann et al. 2014). Small displacement of the solid sediment matrix also contributes to a diffusive component, leading to attenuation and phase shift of the signal with increasing depth (Van der Kamp and Gale 1983; Davis et al. 1995; Wang and Davis 1996). In the model the water phase and sediment matrix are incompressible, thus we are not accounting for dispersion of the pressure signal and propagation speed of a pressure wave in water. Early studies on water flow in cold seeps suggested that upwelling of less dense water, forming a Rayleigh instability, can drive a flow circulation in permeable sediments (Henry et al. 1992, 1996). However, for this the sediment permeability has to be very high $> 10^{-11}$ m^2 and there must be a strong salinity gradient

(Henry et al. 1992), which are conditions typically not encountered at seeps. Since the water-phase density in our model is set to be constant, we do not account for thermohaline effects. We also ignore the effect of pressure and temperature on the compressibility factor of the gas phase.

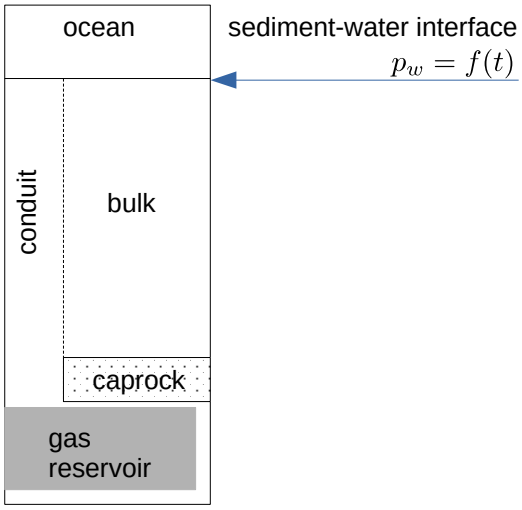

Figure 2.1: Geological setting and schematic for model (not at scale).

The mass balance for the water and gas phase are

$$\phi \frac{\partial S_w}{\partial t} = -\nabla \cdot q_w \tag{2.1}$$

$$\phi \frac{\partial \rho_g S_g}{\partial t} = -\nabla \cdot (\rho_g q_g) \tag{2.2}$$

where ϕ is the porosity, S_α is the phase-saturation (subscript α is used to denote the phase, 'w' or 'g' stands for water or gas, respectively), ρ_g is the gas density, q_α is the Darcy velocity. The saturations are the pore volume fractions filled with each phase, so that $S_g + S_w = 1$ and

$$\frac{\partial S_w}{\partial t} + \frac{\partial S_g}{\partial t} = 0 \tag{2.3}$$

Flow is described by the generalized Darcy equations, so that the velocities depend on the pressure gradient and capillary pressure:

$$q_w = -\lambda_w \kappa \left(\nabla p_w - \rho_w g \nabla z\right) \tag{2.4}$$

$$q_g = -\lambda_g \kappa \left(\nabla p_g - \rho_g g \nabla z\right) \tag{2.5}$$

where $\lambda_\alpha = k_{r\alpha}/\mu_\alpha$, and $k_{r\alpha}$ is the relative permeability of the α-phase obtained from the empirical Van Genuchten equation as functions of water saturation:

$$\begin{aligned} k_{rw}(S_w) &= \bar{S}_w^{\epsilon}\left(1-\left(1-\bar{S}_w^{\frac{n}{n-1}}\right)^{\frac{n-1}{n}}\right)^2 \\ k_{rg}(S_g) &= \bar{S}_g^{\gamma}\left(1-\left(1-\bar{S}_g\right)^{\frac{n}{n-1}}\right)^{\frac{2(n-1)}{n}} \end{aligned}$$

where $\epsilon = 1/2$, $\gamma = 1/3$, ignoring irreducible saturations we set $S_w = \bar{S}_w$ and $S_g = \bar{S}_g$ and also set $n = 3$ (Bastian 1999). The capillary pressure (p_c) defined as $p_g = p_w + p_c$ is also obtained from Van Genuchten's equation as function of water saturation

$$p_c = \frac{1}{\alpha}\left(\bar{S}_w^{-\frac{1}{m}}-1\right)^{\frac{1}{n}}$$

where we set $m = 1 - 1/n$, $n = 3$, and $\alpha = 0.33$ (Bastian 1999).

The gas density behaves with respect to pressure as an ideal gas

$$\rho_g = \rho_0 + cp_g \tag{2.6}$$

as the compressibility (c) is set to a constant value.

2.2.1 Simulation method 1D for conduit

As a first approximation, we only focus on the conduit, and describe the flow of gas- and water-phases only in one dimension. The boundary conditions are

$$\begin{aligned} p_w(z=0,t) &= f(t) \\ q_w(z=L,t) &= q_b \end{aligned}$$

where $f(t)$ can be used to force a tidal stress cycle, e.g.

$$f(t) = \rho_w g A \sin\left(\frac{2\pi}{\tau}t\right) \tag{2.7}$$

where A is the tidal amplitude height, τ is the tidal period. A water-phase Darcy velocity q_b is imposed at the bottom (0.1 m y^{-1} in outcomes shown below).

As initial conditions, the water saturations are set to 0.5 throughout the domain. The pressure is set to the hydrostatic pressure for the pore fluid density, which is a function of the saturation and gas and water densities.

Equations 2.1 to 2.6 are numerically solved by discretizing a one-dimensional domain of length L in N cells. The state variables are p_w and S_w and are represented in the discretiza-

tion scheme as node values. The Darcy velocities (eqns. 2.4 and 2.5) are approximated with the finite volume method and evaluated at cell boundaries. For the upper boundary, the gas phase mobility evaluates $k_{rg}(S_w = 1)$ if the flow is downward and $k_{rg}(S_w = S_w[0])$ if the flow is upward, where $S_w[0]$ is the water-saturation closest to the sediment-water interphase in the grid. For the water-phase $k_{rw}(S_w = S_w[0])$ is used at the upper boundary regardless of flow direction.

Combining eqns. 2.1 and 2.3 and using the computed water-phase Darcy velocities, the temporal change in the phase saturations can be expressed as:

$$\frac{\partial S_g}{\partial t} = \frac{1}{\phi}\frac{\partial q_w}{\partial z}$$

Also the gas density (eq. 2.6) and $\partial(\rho_g q_g)/\partial z$ is computed from pressure. Then the temporal change of the gas pressure can be resolved from

$$\frac{\partial p_g}{\partial t} = -\left[\frac{\partial \rho_g q_g}{\partial z} + \phi\rho_g\frac{\partial S_g}{\partial t}\right]/(\phi S_g c)$$

and that of the water-phase pressure from

$$\begin{aligned}\frac{\partial p_w}{\partial t} &= \frac{\partial p_g}{\partial t} - \frac{\partial p_c}{\partial t}\\ \frac{\partial p_c}{\partial t} &= \frac{\partial p_c}{\partial S_g}\frac{\partial S_g}{\partial t}\end{aligned}$$

The derivative $\partial p_c/\partial S_g$ is solved analytically.

Following this sequence of steps the equations are solved as a system of ordinary differential equations with lsoda (Hindmarsh 1983). The model parameterization can be found in Table 2.2. The code is written in Python and included in appendix A.

2.3 Results and Discussion

Simulations of the vertical flow of water and gas under constant forcing reveal that the water-phase Darcy velocities at the bottom and top of domain differ initially. The water-phase Darcy velocity at the sediment-water interface evolves from 1.4 initially to 0.1 m y^{-1} after $\sim$ 3 years when the water-phase Darcy velocities at the bottom and top approach are approximately balanced (Fig. 2.2). However, the system is not strictly in steady-state (discussed in next subsection). The initial water-phase Darcy velocities correspond to velocities measured with flux meters near bubble ebullition points (Tryon et al. 1999; Solomon et al. 2008), whereas the final velocities match flow estimates obtained from inert tracers profiles

Table 2.2: Overview of chosen model parameters and settings

Parameter description	Symbol	Value
Porosity	ϕ	0.8
Water density	ρ_w	1000 kg m^{-3}
Reference gas density	ρ_0	1 kg m^{-3}
Compressibility	c	$6.8 \cdot 10^{-6}$ s^2 m^{-2}
Absolute permeability	κ	10^{-13} m^2
Domain length	L	10 m
Number of cells	N	50
Dynamic viscosity of water	μ_w	10^{-3} Pa s
Dynamic viscosity of gas	μ_g	10^{-5} Pa s
Tidal period	τ	12 h
Water saturation lower boundary	S_b	0.5
Water-phase Darcy velocity imposed at lower boundary	q_b	0.1 m y^{-1}

at random locations in a seep field (Rooze et al. 2020). While the outflow exceeds the inflow of water, the depth-integrated mass balance is maintained by changing water-saturation in the domain. The resulting water-phase saturation and Darcy velocity profiles (Fig. 2.2) exhibit vacillations from 2 - 4 m depth. When these are smoothed out in the saturation profile by fitting a parabolic line, the resulting flow velocities are also smoothed (not shown). The Darcy velocities of the gas phase are four order of magnitude higher than the water-phase, which is mostly due to the higher buoyancy of the gas phase compared to water. The volumetric gas flow obtained by multiplying the gas Darcy velocity by an area corresponding to a radius of $\sim$ 5 - 10 cm, is on the same order of magnitude as gas fluxes measured by Torres et al. (1998). However, the modeled gas flux is critically sensitive to the relative permeability of the gas phase, which has a strongly non-linear relationship with the gas-phase saturation. The saturation in the sediment column are forced by the imposed saturation at the inlet at the bottom of the domain. Capillary pressures are on the order of 10 Pa and insignificant compared to the buoyant force arising from the density difference between gas and water.

These simulations without tidal forcing provide a reference for the evaluation of fluxes across the sediment-water interface forced by tidal pumping, as well as appropriate depth-profiles of the phase saturation (in relation to the relative permeabilities) and pressure that can be used as initial conditions to study the effect of semi-diurnal tides. In the first day after tidal pumping is turned on, the shape of the general pressure profile and saturation are maintained (not shown). Gas and water continue to flow out at the top of the domain (Fig. 2.3a,b), but the oscillations in tidal pressure lead to a tidal variation in the magnitude of

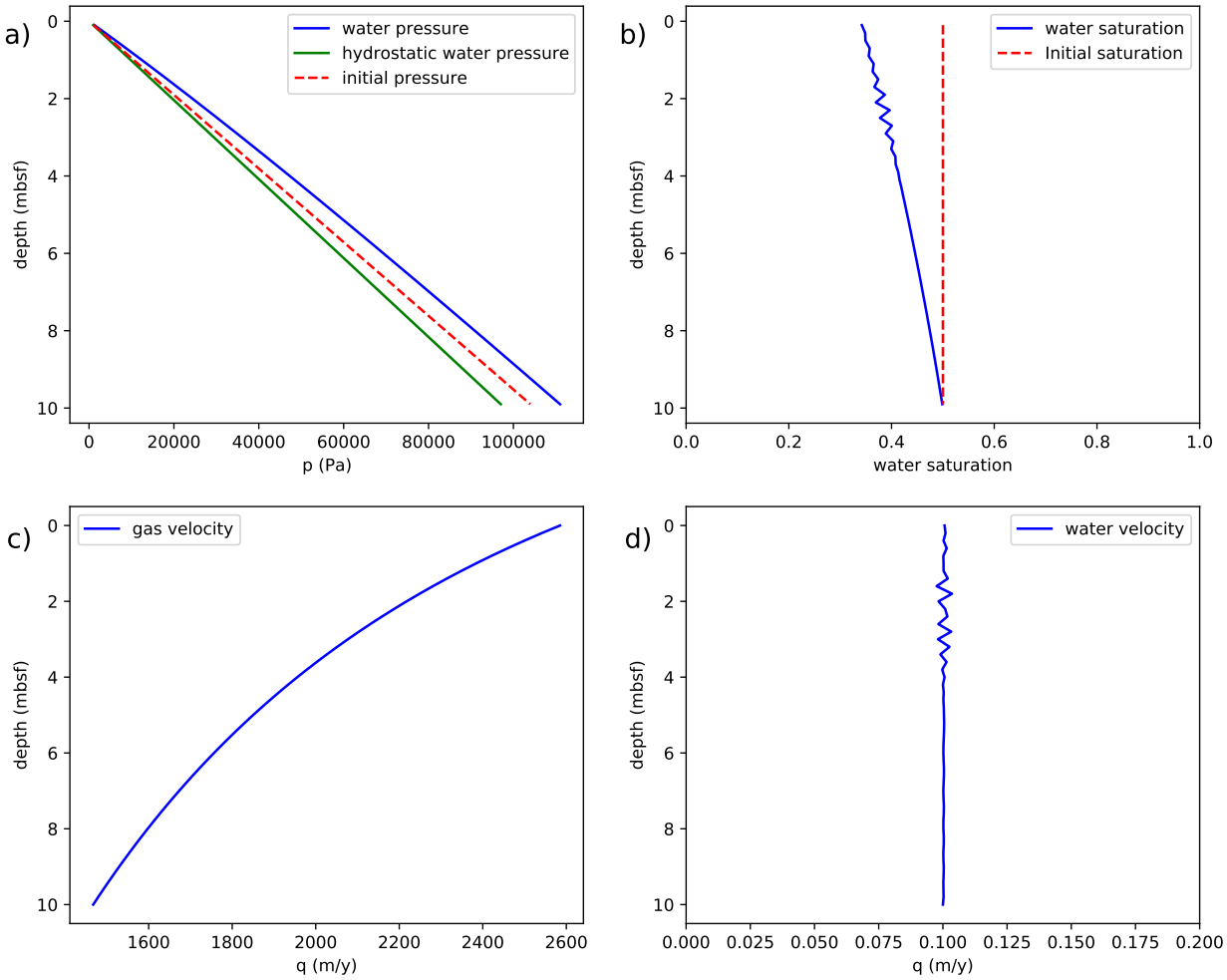

Figure 2.2: State of the system (eqns. 2.1 - 2.6) simulated after 3.3 years without tidal forcing .

these fluxes (Fig. 2.3c, d). The water-phase Darcy velocity integrated over a half tidal cycle during low tide, high tide, and 6 hours without tidal forcing are $1.2 \cdot 10^{-4}$ m, $2.3 \cdot 10^{-5}$ m (net upward displacement), and $6.8 \cdot 10^{-5}$ m, respectively. For the gas phase, the integrated Darcy velocities corresponding to the same time intervals are 2.1 m, 1.5 m, and 1.8 m, respectively.

When the simulation is continued for another 100 days, there is no noticeable change in the tidal pattern of fluxes (not shown). Tidal pumping, however, may fundamentally change the behavior of a system if it is sufficiently large. A change of the tidal amplitude from 1 to 2 m lead to significant flux of ocean bottom-water into the sediment during high tide (Fig. 2.4a), as opposed to continuous outflow at smaller tidal ranges (Fig. 2.3b). During low tide gas expands and porewater is pushed out of the sediment. Conversely, during high

tide bottom-water infiltrates into the sediment as gas compresses, maintaining a constant water-saturation in the top portion of the sediment. In a situation with lower influx of gas from the bottom, gas outflow can cease during high tide.

2.3.1 Simulated gas and water flow dynamics in relation to model setup and environmental conditions

The model results strongly suggest that capillary entry pressure does not impede vertical flow in a conduit, as the magnitude of the vertical excess pressure gradient exceeds variations in capillary pressure by orders of magnitude. Since capillary pressure and relative permeability do not appear to affect particularly the tidal dynamics, the description of the system can be simplified by assuming constant phase-mobilities and ignoring capillary pressure. Combining eqns. 2.1, 2.2, 2.3 yields

$$\frac{1}{\phi}\frac{\partial q_w}{\partial z} = -\frac{1}{\phi}\frac{\partial q_g}{\partial z} - \frac{q_g}{\phi\rho_g}\frac{\partial \rho_g}{\partial z} - \frac{S_g}{\rho_g}\frac{d\rho_g}{dt} \tag{2.8}$$

Fow $p_w = p_g = p$ and constant values of other parameters over depth, eqns. 2.1 to 2.6 can be condensed to

$$\begin{aligned} S_g\frac{\partial p}{\partial t} &= \frac{\lambda_g\kappa}{\phi}\left(\frac{\partial p}{\partial z}\right)^2 + \\ &\quad \frac{(\rho_0 + cp)(\lambda_g - \lambda_w)\kappa}{\phi c}\frac{\partial^2 p}{\partial z^2} - \frac{2\lambda_g\kappa g(\rho_0 + cp)}{\phi}\frac{\partial p}{\partial z} \end{aligned} \tag{2.9}$$

$$\frac{\partial S_g}{\partial t} = \frac{\lambda_w\kappa}{\phi}\frac{\partial^2 p}{\partial z^2} \tag{2.10}$$

As $\lambda_g - \lambda_w$ is positive, the term $\partial^2 p/\partial z^2$ behaves opposite to diffusion and thus has the tendency to form peaks. This may explain the oscillations observed in the saturation profile. Eq. 2.10 implies that for steady-state conditions $\partial^2 p/\partial z^2 = 0$. Inserting this into eq. 2.10 and solving it analytically yields a solution in which $d^2 p/dz^2 \neq 0$, meaning that the system cannot be at steady-state.

By analyzing the magnitude of terms in equation 2.8, it can be shown that the term with the density derivative has the largest impact. Therefore, a 0D box-model only accounting for compression and expansion of hydrocarbons may be able to represent the basic behavior of the system. This can be used, for instance, to analyze the effect of the presence of oil. Based on correlations for pressure-temperature behavior of gas-oil mixtures (Boyun et al. 2007), gas would typically exsolve during periods of low tide and dissolve in oil at high tides. This behavior strenghens tidal signals, which is in line with observations of gas emissions from abandoned oil wells (Table 2.1). A 0D model cannot reproduce the more complicated patterns with sluggish flow observed at oil seeps. Periods with emissions of more oily bubbles

can alternate with periods with emissions of more gassy bubbles (Leifer 2019), and oil has the tendency to constrict flow paths for gas (Bastian 1999).

The 1D model setup can be justified for gas flow, which follows a path of least resistance through fractures and conduits (Clennell et al. 2000). The entry pressure for gas to invade low permeablity sediments is too high to occur without sediment deformation, so unlikely to occur in the presence of a gas conduit. The mechanism we propose to explain flow oscillations pertains to settings with an established flow conduit, connecting the sediment-water interface to the deeper subsurface. We have not explored whether the mechanism applies to settings in which a pipe from a reservoir approaches but does not extend all the way to the sediment-water interface (Gay et al. 2012). The 1D model may not accurately resolve water flow in the presence of gas. Gas may push water more easily aside than up (Tryon et al. 2002), as water is less buoyant and can flow through low permeability sediments. However, in our simulations saturation hardly changes during tidal cycles, indicating that gas in a continuous phase accelerates or decellerates during expansion or compression, respectively, but does not push away or give way to the water-phase. The representation of gas as a continuous phase throughout the model domain, contrasts with settings where a stream of bubbles induces turbulent down-mixing of water, which increases the exchange of water between the bottom-water and sediment (Haeckel et al. 2007).

Water-depth can be expected to be a critical factor for the effect of the tidal pressure variations on flow patterns, as the relative change in volume of an ideal gas is approximately the tidal amplitude divided by the water-depth. Emissions of gas tend to be correlated to tides in shallow water environment, such as in the South China sea at < 50 m (Di et al. 2014), Coal Oil Point at 20 - 80 m (various studies, Table 2.1), the Doggerbank at < 40 m (Groot et al. 2019). The tidal patterns in these studies are often superimposed on a continuous mean outflow, which is in line with our model, but not with intermittent flow induced by sediment dilation and compaction during tidal cycles (e.g. Scandella et al. 2011; see introduction). Wiggins et al. (2015) also found a tidal signal at ~ 100 m water-depth in the North-Sea, but with an opposite trend, i.e. with increased gas emissions during high tide, for which they propose that it relates to capillary activation and complex spatial flow connections. As an alternative explanation, compression of gas may increase the gas mobility (Rosenberry et al. 2006; see introduction), but this remains speculative. The pattern is opposite to the trend expected from our model. In the Sea of Marmara (350 - 1250 m water-depth) there appeared to be no tidal signal in gas release. This is likely due to the low tidal amplitude of ~ 3 cm (Bayrakci et al. 2014).

Cold seeps from Hydrate Ridge (~ 800 m water-depth) exhibit generally tidal flow patterns in both gas and water flow (Table 2.1), which corresponds well to the modeled behavior. However, in the Gulf of Mexico at depths of 540 m (Bush Hill), 850 m (MC118), and 1200 m (GC600), emissions can typically not be correlated to tidal pressure oscillations (Table 2.1). More pronounced tidal patterns would also be expected at Hydrate Ridge due the larger

tidal range (on the order of $\sim$ 2.5 m) compared to the seep sites in the Gulf of Mexico (on the order $\sim$ 0.5 m; NOAA 2020). A tidal pattern was also observed at the seeps of Northern Cascadia at 1250 m depth, which experiences tidal pressure oscillation of 1282-1286 dbar (1 dbar corresponds to the hydrostatic pressure of $\sim$ 1 m water-depth; Römer et al. 2016).

An additional possible cause for the lack of tidal signals in the emissions from seeps of the Gulf of Mexico are the softer sediments. In harder sediments conduits can extend to the sediment-water interface. The length of a pipe structure is critical, as the total change in volume of gas in the entire conduit determines the amplitude of fluxes. For this reason tidal signals may also be stronger in abandonded wells, where actual pipes have been drilled to deeper reservoirs (Table 2.1). In the Gulf of Mexico conduits are connected to deeper thermogenic hydrocarbon reservoirs. However, the upper sediments are softer, which can lead to the formation of a V-shaped seepage structure (Gay et al. 2012). The spreading of gas over a larger area in this structure may reduce oscillations in vertical fluid flow. However, this remains speculative.

The model can be adapted to environmental conditions: For a larger hydrostatic pressure at the sediment-water interface at greater water-depth the upper boundary conditon needs to be adapted, and the reference density needs to be increased. A larger value for ρ_0 (eq. 2.6) leads to smaller variations in the density due to tidal oscillations. The length of the conduit is set by the model length. As we used a conduit of only 10 m length, tidal variations in flow can be expected to be larger at locations with longer pipe structures. For quantitative estimates of deeper conduits, it is important to take into account dissipation and lag of tidal pressure signals (Davis et al. 1995; Wang and Davis 1996), which has currently not been implemented. For longer conduits it will be also be more important to account for non-ideal behavior of methane gas.

2.4 Conclusion

The model simulates water and gas flow in a conduit, leading to efficient transport of hydrocarbons from the subsurface to the seafloor. Simulated gas emissions are similar to those measured in seep areas at locations with focussed flow (Torres et al. 1998). Changes in hydrostatic pressure acting as a stress on the sediment-water interface can significantly compress or expand gas volumes in a conduit, leading to water and gas fluxes at the sediment-water interface that vary with the tides (Figs. 3, 4). The significant oscillations in water flux around a mean water flux do not lead to significant displacements of water during a tidal cycle due to the relative short time-period of 6 hours. This is in line with the argument that tidal oscillations affect flow velocities measured by water flux meters installed on the seafloor, but are not captured in flow estimates based on inert tracers (Rooze et al. 2020). The effects of tidal pressure oscillations are expected to be stronger in sediments at shallower

depth and at sites experiencing larger tidal amplitudes. The higher hydrostatic pressure in the deep-sea make tidal hydrostatic pressure oscillations less important.

While our analysis shows the potential impact of pressure fluctuations, the quantitative estimates of gas and water flow oscillations are sensitive to the chosen domain length, and it is not clear what length is appropriate. Oscillations in vertical water flow may be over-estimated, as the 1D model does not allow water to flow horizontally in response to gas compression/expansion. Quantitative estimates of the magnitude of flow oscillations can be improved by simulating the stress field and dispersion of the tidal stress signal (Davis et al. 1995; Wang and Davis 1996), implementing an equation of state for methane to represent the behavior of gas (Wang et al. 1998), and increase the model dimensionality to 2D with radial symmetry.

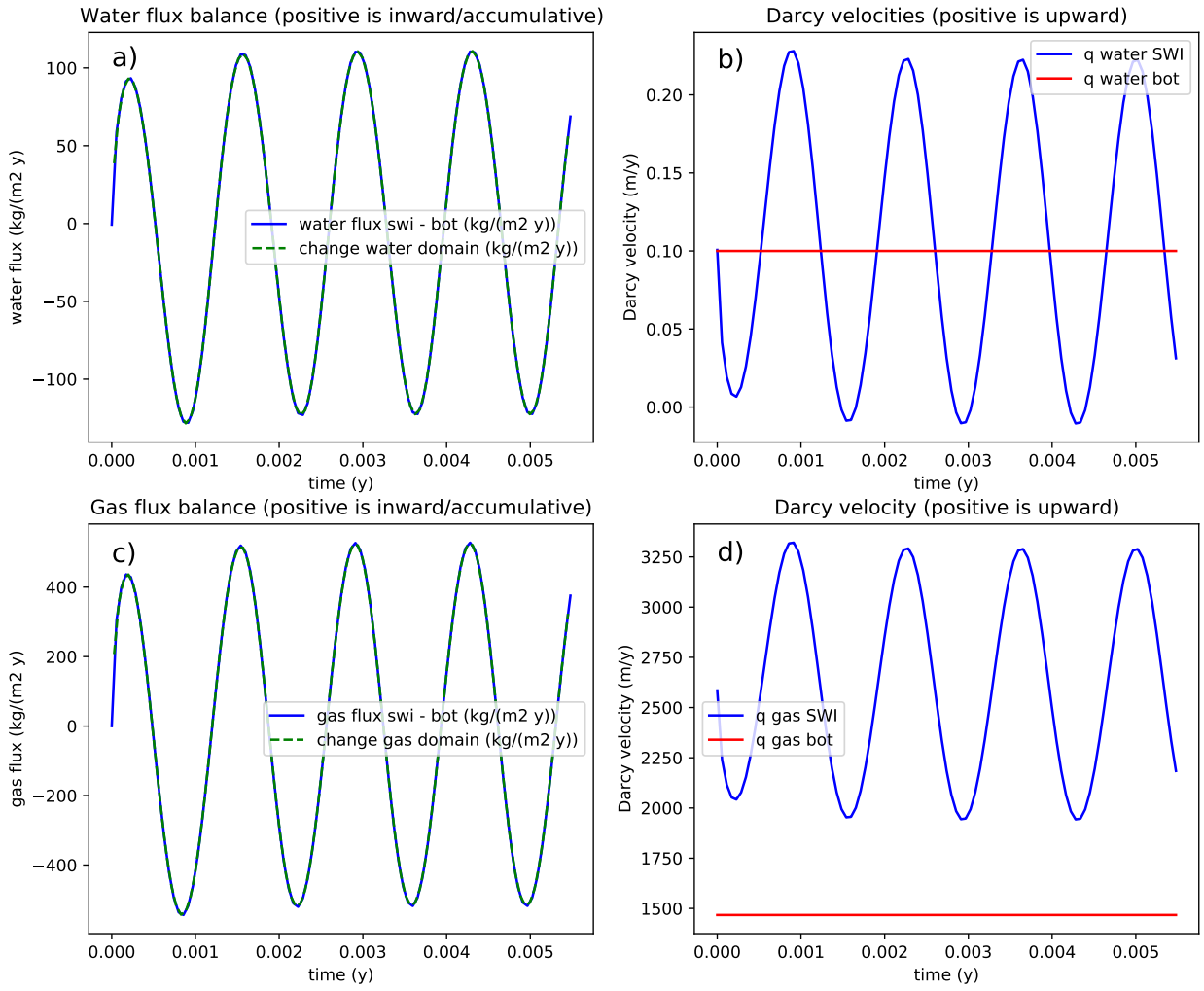

Figure 2.3: Effect of timing on tidal forcing in the first 2 days, beginning from initial conditions shown in Fig. 2.2. The tidal stress function (eq. 2.7) is out of phase with the gas and water fluxes at the sediment-water interface, 'bot' stands for bottom, 'swi' stands for sediment-water interface, q stands for the Darcy velocity.

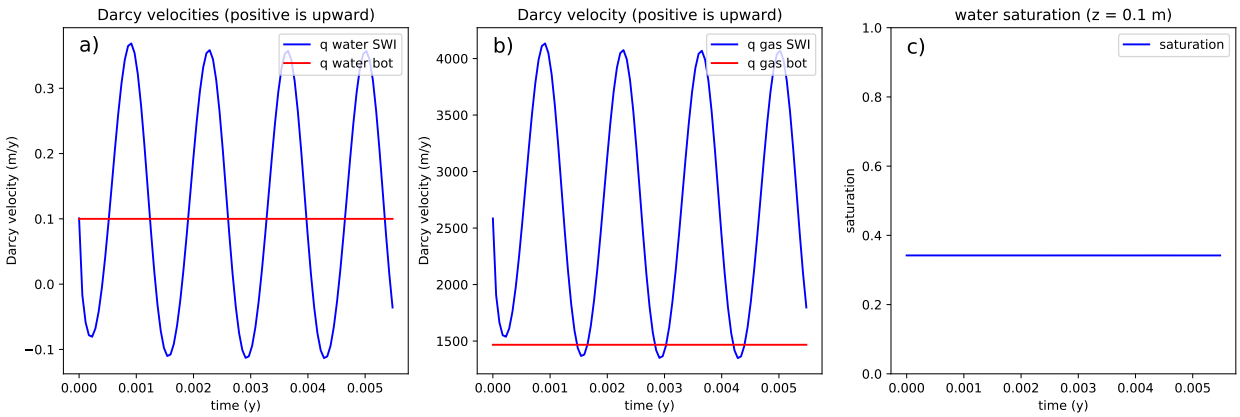

Figure 2.4: Effect of increasing the tidal amplitude to 2 m water-height.

Chapter 3

Porewater Flow Patterns in Surficial Seep Sediments Inferred from Conservative Tracer Profiles and Early Diagenetic Modeling[1]

[1]Rooze, J., L. Peterson, R. N. Peterson, and C. Meile (2020). In: *Chemical Geology* 536, p. 119468. Reprinted here with the permission of the publisher.

Abstract

Porewater flow at cold seeps controls methane oxidation and carbonate precipitation rates, and also plays an important role in gas hydrate dynamics. We constrain the porewater flow rates in the upper sediment of Gulf of Mexico cold seeps by fitting measured ^{226}Ra and Cl^- profiles. The approach exploits their natural increase with depth through shallow sediments at non-brine (^{226}Ra) and brine (Cl^-) seeps. Vertical flow velocities at non-brine and brine seeps are found to be similar in magnitude, typically on the order of 0.1 m y^{-1}. The accuracy of the flow estimates is assessed and shown to depend substantially on uncertainties in both concentrations and sediment tortuosity. Model simulations further reveal that the natural heterogeneity of sediment permeability can cause considerable lateral variability in vertical flow at the scale of a sediment core, which implies that the coring location and core size can have a substantial effect on the estimated porewater velocities. The formation of gas hydrates and calcium carbonates reduce sediment permeability, and decrease the spatial variability in flow over time, as the formation rates are higher along preferential flow paths. This analysis of the effect of spatiotemporal variability on chemical profiles improves the assessment of uncertainties in the estimated magnitude of flow, and is important for the evaluation of benthic-pelagic coupling at seeps.

3.1 Introduction

Cold seep environments in the deep-sea form the habitat of large and highly biodiverse benthic communities (Cordes et al. 2009), which thrive, in the absence of sunlight, on microbial communities that oxidize ascending hydrocarbons and reduced metabolites. The hydrocarbons can be of microbial and thermogenic origin and are comprised of methane, short-chain alkanes, and crude oil (Sassen et al. 2004). Oxidation of these reduced solutes in the surficial sediments modulates inorganic carbon and energy fluxes to seep communities near the seafloor and the oceanic ecosystem (Hovland et al. 2012; Niemann et al. 2013; Levin et al. 2016). Anaerobic oxidation of methane, driven by the transport of dissolved methane in porewater, further induces the precipitation of calcium carbonate. Most of the hard substrata in the northern Gulf of Mexico derive from seeps and are used by organisms for attachment and protection (Roberts and Aharon 1994; Levin et al. 2016).

The efficiency of hydrocarbon oxidation in sediments depends on the upward transport of substrates from depth to the upper sediment and their exposure to oxidants from the overlying water, particularly oxygen and sulfate (Sommer et al. 2006; Orcutt et al. 2017). Local porewater and gas flow control the mixing of reducing and oxidizing fluids but are difficult to constrain due to their diffuse nature and variability. The release of gas and oil bubbles has been shown to oscillate with swells (Leifer and Boles 2005) and the tide (e.g. Di et al. 2014; Johansen et al. 2017; Römer et al. 2016). Also, processes in the deep

subsurface (Roberts and Carney 1997), changes in oceanographic conditions (Römer et al. 2016), and earthquakes (Lapham et al. 2008b; Fischer et al. 2013) induce temporal variability. Porewater flow fluctuates with the tide as well (Tryon et al. 1999; Tryon and Brown 2001) and can be affected by gas expulsion events (Tryon and Brown 2004; Solomon et al. 2008). The formation of carbonates and gas hydrates impedes and deflects flow (Clennell et al. 2000; Hovland 2002; Solomon et al. 2008), introduces spatial heterogeneity, and contributes to the succession and patchy distribution of seep fauna (Bergquist et al. 2003; Lessard-Pilon et al. 2010). When bottom-water temperature increases, gas hydrate near the surface can rapidly dissociate and allow for underlying gas and water to escape (MacDonald et al. 1994).

Continuous and direct records of seepage have been obtained only at few sites (Tryon et al. 1999; Solomon et al. 2008; Barnes et al. 2015; Martens et al. 2016). Instead, most studies rely on chemical and/or temperature profiles to constrain the transport of porewater and dissolved methane. Notably, porewater flow velocities obtained from chloride profiles have been typically on the order of 0.1 m y^{-1}, whereas flow meters have often measured flow velocities well above 1 m y^{-1} (see Lapham et al. (2008a) and Vanneste et al. (2011) for compilations). These considerations raise the question to what extent chemical/temperature profiles can provide reliable constraints on transport in cold seep environments, and how spatial and temporal variability may impact the determination of seepage rates.

In this communication, we determine porewater flow velocities for a number of sites in the northern Gulf of Mexico by fitting a 1D diffusion-advection model to depth profiles of the stable, conservative tracers ^{226}Ra (for non-brine seeps) and Cl^- (for brine seeps). We investigate with a multidimensional reaction-transport model the effect of spatiotemporally varying flow on tracer distributions and the implications for fitting tracer profiles, and also use the model to explore the interplay between early diagenetic processes and flow patterns.

3.2 Methods

3.2.1 Sample collection and measurements

Sediment cores for porewater ^{226}Ra analysis were collected using a shipboard multiple corer from the R/V Endeavor in summer 2015 (EN559). Cores were collected from known cold seeps and control sites across the northern continental slope of the Gulf of Mexico, including (from east to west) in the Mississippi Canyon (BP444 and BP463), Green Canyon (GC185, GC186, GC574, GC600, GC699, and GC767), and Garden Banks (GB480 and GB847) lease blocks (see inset of Fig. 3.3). Following core recovery, overlying waters were siphoned off and passed slowly through 25 g aliquots of dry acrylic fibers impregnated with MnO_2 ('Mn fibers'; Moore 1976). Sediments were then sectioned at 4 cm vertical intervals into centrifuge tubes and spun at 5000 RPM for 15 minutes. Recovered porewaters were collected from the

centrifuge tubes via needle and syringe, diluted to 1 L with Ra-free seawater, and similarly passed through Mn fibers.

Mn fibers were then rinsed with Ra-free freshwater and dried to an optimal humidity level (0.3 – 1 $g_{ceH2O}/g_{\text{fiber}}$; Sun and Torgersen 1998) before being analyzed for short-lived Ra isotopes (data presented elsewhere). The fibers were then transported to the lab where they were sealed in an air-tight cartridge to allow equilibration of ^{222}Rn with ^{226}Ra on the fiber and subsequently on a radon emanation line (following Peterson et al. 2009). Analytical uncertainties presented throughout represent 1-σ measurement uncertainties based on counting statistics.

Porosities were determined by mass loss upon drying (Joye 2018). To calculate the diffusivities of radium at the seep locations we used the reported temperatures, salinities, and water-depth from the cruise (Montoya 2015). Chloride profiles used in this work were measured and reported by Castellini et al. (2006).

3.2.2 Fitting measured 1D conservative tracer profiles

Radium isotopes in sediment are transported by advection and diffusion, adsorb onto and desorb from sediment surfaces, and decay radioactively. Following Bear (1972), the governing equation for the total (dissolved and adsorbed) radium profile can be written as

$$\frac{\partial}{\partial t}\left(\phi C + \phi_s F\right) = \frac{\partial}{\partial x}\left(\frac{\phi D}{\alpha^2}\frac{\partial C}{\partial x} - \phi u C\right) - \lambda(\phi C + \phi_s F) \tag{3.1}$$

where C is the dissolved radium concentration in units of mol per fluid volume, F is the adsorbed radium concentration in units of mol per solid volume, ϕ is the porosity, $\phi_s = 1-\phi$ is the solid volume fraction, D is the tracer diffusivity, α is the tortuosity, u is the pore water flow velocity, λ is the decay constant, and here x is the depth in the sediment. Biologically induced mixing is ignored. When adsorbed and dissolved radium are in equilibrium (i.e., $K = F/C$) and porosity is not varying with time, then

$$(\phi + \phi_s K)\frac{\partial C}{\partial t} = \frac{\partial}{\partial x}\left(\frac{\phi D}{\alpha^2}\frac{\partial C}{\partial x} - \phi u C\right) - \lambda C(\phi + \phi_s K) \tag{3.2}$$

Defining $R_d = (\phi + \phi_s K)$ yields

$$\frac{\partial C}{\partial t} = \frac{1}{R_d}\frac{\partial}{\partial x}\left(\frac{\phi D}{\alpha^2}\frac{\partial C}{\partial x} - \phi u C\right) - \lambda C \tag{3.3}$$

In this study, we used the most abundant Ra isotope, ^{226}Ra, which has a half-life of 1600 years. The slow decay of ^{226}Ra has no discernible effect on the concentration profile, as the residence time of radium in the upper sediment is only on the order of years or less. Ignoring

decay, assuming steady-state ($\partial C/\partial t = 0$), and multiplying Eq. 3.3 by R_d yields

$$0 = \frac{d}{dx}\left(\frac{\phi}{\alpha^2}\frac{dC}{dx} - \Theta_1\right) - \lambda C \tag{3.4}$$

where $\Theta_1 = \phi u/D$ is outside the derivative because the diffusion coefficient is assumed to be constant with depth, and the Darcy velocity ($q = \phi u$) is constant in order to conserve mass. Note that Eq. 3.4 applies to tracers in general (including Cl^-), and that C can represent a mass or an activity (decays per minute) per porewater volume. The sediment porosity was described as

$$\phi(x) = \phi_\infty + (\phi_0 - \phi_\infty)e^{-\beta x} \tag{3.5}$$

where ϕ_0 is the porosity at the sediment-water interface, ϕ_∞ is the asymptotic porosity value at depth, and β is a parameter determined by fitting each porosity profile. Tortuosity was defined as function of the pore volume fraction filled with water (Boudreau, 1996):

$$\alpha^2(\phi) = 1 - 2\log(\phi S_f) \tag{3.6}$$

where S_f is the water saturation, here set to 1.

Equation 3.4 was discretized with a finite volume method (Versteeg and Malalasekera 2007) and solved numerically in R 3.4. The grid had a 1 mm vertical resolution and ranged from the sediment-water interface to 1.5 times the depth of the deepest measurement. The activities at the top and bottom of the profile were set to Θ_2 and Θ_3, respectively. Their values, along with the parameter Θ_1, were fitted to the measured profiles with the nlm function in R (Dennis Jr and Schnabel 1983; Schnabel et al. 1985). Local sensitivities were computed as the first derivative of the radium activities with respect to the fitting parameters (Soetaert, Petzoldt, et al. 2010). Confidence intervals were determined with a Monte Carlo analysis. Ten thousand depth profiles were created by randomly selecting a Ra activity or Cl- concentration from a normal distribution, which was defined by the reported mean and standard deviation at each depth a measurement had been made. Each profile realization was then fitted, and from all the fitted parameter values the 95% confidence intervals were determined.

3.2.3 Multidimensional reaction-transport model

The range of velocities obtained from fitting equation 4 to the data was then used to inform a multidimensional reaction-transport model to simulate the effect of carbonate and hydrate formation on flow and tracer distributions. Luff et al. (2005) developed a 1D model to evaluate the effect of carbonate crust formation on permeability reduction. Our new model expands on their work by incorporating gas hydrate dynamics and considering lateral

heterogeneity in flow and reactions. The distribution of solutes was described as

$$\frac{\partial(\phi S_f C_i)}{\partial t} = \nabla \cdot \left[\phi S_f \left(\frac{D_i}{\alpha^2} + D_b \right) \nabla C_i - \phi S_f (u + w) C_i \right] + R_i \tag{3.7}$$

where S_f is the water saturation, which is the pore volume fraction filled by fluid, C_i is the concentration of solute i, R is a source/sink term for reactions, and w is the burial velocity. Eq. 3.7 was also used to simulate an unreactive tracer. The model formulation assumed that bioturbation leads only to intraphase mixing and does not affect the porosity gradient (Mulsow et al. 1998). The bioturbation coefficient D_b accounts for enhanced mixing of sediment by infauna, and was parameterized to decrease with depth (x):

$$D_b = D_0 e^{-x/\zeta} \tag{3.8}$$

where D_0 is the bioturbation coefficient at the top in the domain, and ζ is the e-folding length (Table 3.1; Reed et al. 2011). Typical conditions at 1000 m water-depth (Table 3.1) were assumed to calculate the diffusivities. The model did not account for advective flow induced by macrofauna.

Table 3.1: Parameterization of the reaction-transport model.

Description	Symbol	Value	Source
Salinity	S	35	
Temperature	T	278 K	
Hydrostatic pressure at the sediment-water interface	p	$1.01 \cdot 10^7$ kg m^{-1} y^{-2}	
Molecular diffusivity of oxygen	D_{O2}	0.0463 m^2 y^{-1}	S
Molecular diffusivity of sulfate	D_{SO4}	0.0201 m^2 y^{-1}	S
Molecular diffusivity of hydrogen sulfide	D_{HS}	0.0375 m^2 y^{-1}	S
Molecular diffusivity of bicarbonate	D_{HCO3}	0.0216 m^2 y^{-1}	S
Molecular diffusivity of calcium	D_{Ca}	0.0150 m^2 y^{-1}	S
Molecular diffusivity of methane	D_{CH4}	0.0352 m^2 y^{-1}	S
Molecular diffusivity of tracer (radium)	D_{Ra}	0.0147 m^2 y^{-1}	S
Bioturbation coefficient at the sediment-water interface	D_0	0.0012 m^2 y^{-1}	M

Continued on next page

Table 3.1 – continued from previous page

Description	Symbol	Value	Source
E-folding length of bioturbation	ζ	0.01 m	
Dynamic viscosity of water	μ	$3.15 \cdot 10^4$ kg m^{-1} y^{-1}	
Sediment density	ρ_s	2500 kg m^{-3}	
Calcite density	ρ_c	271 kg m^{-3}	
Hydrate density	ρ_h	930 kg m^{-3}	
Water density	ρ_h	1028 kg m^{-3}	
Burial velocity	w	$6 \cdot 10^{-5}$ m y^{-1}	A
Rate constant for aerobic methane oxidation	k_1	10^7 m^3 mol^{-1} y^{-1}	W
Rate constant for sulfide oxidation	k_2	160 m^3 mol^{-1} y^{-1}	W
Rate constant for anaerobic methane oxidation	k_3	200 mol m^{-3} y^{-1}	T
Half-saturation constant anaerobic methane oxidation for sulfate	K_{m1}	1 mol m^{-3}	N
Half-saturation constant anaerobic methane oxidation for methane	K_{m2}	37 mol m^{-3}	Z
Rate constant for calcium carbonate formation	K_{4f}	10^5 mol m^{-3} ym^{-1}	L
Rate constant for calcium carbonate dissolution	K_{4b}	18.3 y^{-1}	J
Power for calcium carbonate dissolution	m	4.5	J
Rate constant for gas hydrate formation	$k_{5\mathrm{f}}$	10 y^{-1}	T
Rate constant for gas hydrate dissolution	$k_{5\mathrm{b}}$	10^3 y^{-1}	T
Calcite solubility constant	K_c	0.521 mol^2 m^{-6}	H
Acid dissociation constant of H_2CO_3	K_{H2CO3}	$9.45 \cdot 10^{-4}$ mol m^{-3}	H
Acid dissociation constant of HCO_3	K_{HCO3}	$5.35 \cdot 10^{-7}$ mol m^{-3}	H
Acid dissociation constant of H_2S	K_{H2S}	$1.51 \cdot 10^{-4}$ mol m^{-3}	H
Acid dissociation constant of boric acid	K_{BOH3}	$1.56 \cdot 10^{-6}$ mol m^{-3}	H
Ionization constant of water	K_w	$1.15 \cdot 10^{-8}$ mol^2 m^{-6}	H
Total borate concentration	TB	0.42 mol m^{-3}	H

Continued on next page

Table 3.1 – continued from previous page

Description	Symbol	Value	Source
Reference porosity	ϕ_r	0.8	
Reference permeability	κ_r	10^{-12} m^2	
Reference equilibrium concentration of methane	C_0	87 mol m^{-3}	T
Temperature gradient	dT/dx	1 K m^{-1}	
Derivative of the equilibrium methane concentration to temperature	dC_{eq}/dT	5 mol m^{-3} K^{-1}	T

Sources: A = Aharon and Fu 2000; H = Hofmann et al. 2010; J = Jourabchi et al. 2010; L = Luff and Wallmann 2003; M = Middelburg et al. 1997; N = Nauhaus et al. 2002; S = Soetaert et al. 2010; T = see text; W = Wang and Van Cappellen 1996; Z = Zhang et al. 2010

The distribution of gas hydrate was described by

$$\frac{\partial(\phi S_h)}{\partial t} = \nabla \cdot (\phi D_b \nabla S_h - \phi w S_h) + R_h \tag{3.9}$$

where C_j is the calcium carbonate concentration, ϕ_s is the solid volume fraction, and R_j is the net rate of calcium carbonate precipitation and dissolution. The solid volume fraction was computed, following Jourabchi et al. (2010), as

$$\frac{\partial \phi_s}{\partial t} = -\nabla \cdot (w \phi_s) + R_s \tag{3.10}$$

where R_s is the rate at which calcium carbonate reactions change the solid volume fraction.

Reaction network - The model simulated the dynamics of elements that could affect the permeability field through gas hydrate and calcium carbonate formation, including reactions (Table 3.2) that influence the pH through the production or consumption of alkalinity and dissolved inorganic carbon (Soetaert et al. 2007; Hagens and Middelburg 2016). Aerobic oxidation of methane and sulfide make porewater more acidic (R1, R2, Table 3.2). Conversely, anaerobic oxidation of methane increases the alkalinity (R3). The concentrations of dissolved calcium and carbonate determine the saturation state of calcium carbonate, which can buffer porewater to increases and decreases in pH through dissolution (R4b) and precipitation (R4f), respectively. Assuming rapid equilibration of dissolved acids and bases, pH was computed from total alkalinity (TA), dissolved inorganic carbon (TC), total dissolved sulfide (TS), and total borate (TB). Ignoring the contribution of diffusive fluxes of minor constituents, we used total alkalinity, dissolved inorganic carbon, and total sulfide as state variables (Eq. 3.7) with the diffusivity of bicarbonate for TA and TC, and that of hydrogen sulfide for TS. The total borate concentration is set to a constant value, representative of the

bottom-water (Table 3.1). The carbonate ion concentration was calculated from the total alkalinity and the dissolved inorganic carbon.

Gas hydrate formation and dissolution were implemented as kinetic processes forced by the saturation state (Table 3.2). The equilibrium concentration of dissolved methane (C_{eq}) was approximated by

$$C_{\mathrm{eq}} = C_0 \frac{dC_{\mathrm{eq}}}{dT} \frac{dT}{dx} \Delta x \tag{3.11}$$

where C_0 is the reference equilibrium concentration at the sediment-water interface (Table 3.1), and T is the temperature. Since temperature profiles are linear in the upper meters of sediment at cold seeps (Smith et al. 2014), dT/dx was set to a fixed value (Table 3.1). Also, dC_{eq}/dT was assumed to be constant. The values of C_0 and dC_{eq}/dT were based on the model of Duan et al. (2011) and evaluated at the pressure, temperature, and salinity given in Table 3.3. Equation **??** does not account for the effect of minor changes in pressure and salinity with depth on C_{eq}. The rate constant of gas hydrate formation was based on experimental data (Table 3.1; Chaturvedi et al. 2018), and the dissolution rate constant was chosen sufficiently large so that the methane concentration remains near equilibrium with gas hydrate.

Aerobic oxidation of methane and sulfide were described by bimolecular rate laws, following Wang and Van Cappellen (1996). The rate of anaerobic oxidation of methane was described with Michaelis-Menten terms for both sulfate and methane (Table 3.2;Regnier et al. 2011), and the parameterization was informed by rates measured at seeps (Table 3.1; Treude et al. 2003; Joye et al. 2004).

Transport and permeability field - For the solid phases, the burial velocity was set to a constant value (Table 3.1). For the aqueous phase, flow was calculated from the pressure field and Darcy's law

$$q = -\frac{\kappa}{\mu} \nabla p \tag{3.12}$$

where κ is the permeability, μ is the dynamic viscosity of water, and p is the excess pressure. The excess pressure field was obtained from solving the mass conservation equation

$$\nabla \cdot q + \frac{\partial (S_f \phi)}{\partial t} = 0 \tag{3.13}$$

after substitution of q using equation 3.12. The excess pressures at the top and bottom of the model domain were set to fixed values, whereas no gradient boundary conditions were applied at the sides. The effect of changes in the porosity and water saturation on permeability are

accounted for by

$$\kappa = \kappa_r \left(\frac{S_f \phi}{\phi_r} \right)^n \tag{3.14}$$

where κ_r is the reference permeability, ϕ_r is the reference porosity, and n is an empirical exponent (Kossel et al. 2018). A random permeability field for the initial permeability was produced with simple kriging (Delhomme 1978) following a log-normal distribution with a mean of $1.4 \cdot 10^{-11}$ m^2, a standard deviation of $1.1 \cdot 10^{-11}$ m^2 ($\sigma^2_{\log \kappa} = 0.5$), and a correlation length of 7 cm, based on measurements of marine sediment (Briggs et al. 1998; Reed et al. 2002). For the exponent n, studies on the permeability reduction induced by gas hydrate formation have reported a wide range of values, mostly between 2.5 and 15 (see Kossel et al. 2018 and references therein) - we used a value of 10 in the baseline simulation. To explore the effect of solid formation on flow in a more heterogeneous setting, simulations were also performed with a preferential flow conduit, representing the relict of a fracture or bubble stream. Such a conduit was implemented as a 5 cm wide column with a ten-fold higher permeability on the left side of the domain.

Implementation - The transient simulations were run in 2D. A Cartesian grid with cells of 1x1 cm2 was designed to represent a 0.7 m wide and 1.41 m deep domain. An overview of the boundary conditions for all state variables can be found in Table 3.3. The concentrations at the top and bottom boundaries are representative of the overlying water at a depth of 1000 m, which is oversaturated with respect to calcite, and the composition of the rising porewater, respectively. Initial values were set to 0, except for total alkalinity, dissolved inorganic carbon, and dissolved calcium, which were set to values in equilibrium with calcite.

The model was implemented with the finite volume method in R 3.4 and C. The sequential iterative operator splitting (Steefel and MacQuarrie 1996) approach was applied to couple transport to reaction rates, which were computed with CVODE (Hindmarsh et al. 2005). Random permeability fields were created with the R-package gstat (Pebesma 2004), acid-base constants were calculated with AquaEnv (Hofmann et al. 2010), and diffusion coefficients were obtained from marelac (Soetaert et al. 2010). The FME R-package (Soetaert, Petzoldt, et al. 2010) was used for statistical analyses.

Applicability - The model simulates the formation of dispersed gas hydrates and calcium carbonate crust and the transport of dissolved methane through the upper sediment. Such conditions are characteristic features of seeps with lower flow velocities and at the periphery of more active vents (Roberts and Carney 1997). The model does not simulate the transport of free gas (for this see Mogollón et al. 2009), which is important at locations with more active seepage. It can lead to more complicated spatial flow patterns and higher temporal variability (Tryon et al. 2002) and the formation of massive gas hydrates that grow in the vicinity of or even cross the sediment-water interface. The model does not simulate the mobilization of sediment, the formation of fractures, and the washout of carbonates (Roberts

Table 3.2: Reaction network and rate laws.

Reaction stoichiometry	Kinetic rate law
$2\,O_2 + CH_4 \longrightarrow CO_2 + 2\,H_2O$	$R_1 = k_1[O_2][CH_4]$
$2\,O_2 + H_2S + 2\,HCO_3^- \longrightarrow$ $SO_4^{2-} + 2\,CO_2 + 2\,H_2O$	$R_2 = k_2[O_2][H_2S]$
$SO_4^{2-} + CH_4 + CO_2 \longrightarrow$ $2\,HCO_3^- + H_2S$	$R_3 = k_3 \frac{[SO_4^{2-}]}{[SO_4^{2-}]+K_{m1}} \frac{[CH_4]}{[CH_4]+K_{m2}}$
$Ca^{2+} + CO_3^{2-} \rightleftharpoons CaCO_3$	$R_{4f} = (\Psi > 0) k_{4f} \Psi$
	$R_{4b} = (\Psi < 0) k_{4b} [CaCO_3] \Psi^m$
$CH_4 + 6\,H_2O \rightleftharpoons CH_4 * H_2O$	$R_{5f} = ([CH_4] > C_{eq}) k_{5f} \Upsilon$
	$R_{5b} = ([CH_4] < C_{eq}) k_{5b} S_h \Upsilon$

The saturation index for calcium carbonate is defined as $\Psi = [Ca^{2+}][CO_3^{2-}]/K_c - 1$, and for gas hydrate as $\Upsilon = [CH_4]/C_{eq} - 1$.

and Carney 1997; Crémière et al. 2016), nor the effect of macrofauna and microbial mats on flow (Hovland 2002).

3.3 Results and Discussion

We first describe the Darcy velocities derived from fitting measured 226 Ra profiles (Fig. 3.1) with the 1D diffusion-advection model, and then present the effect of early diagenetic processes on the flow and tracer profiles in cold seep sediments.

3.3.1 Estimates of vertical Darcy velocities

Upward flow carries the tracer-enriched porewater from depth towards the sediment surface, with tracer concentration decreasing towards that in the overlying water (Fig. 3.2a). The steepness of the Ra activity gradient near the sediment-water interface reflects the relative strength of advection compared to diffusion, a relation contained in the principal fitting parameter Θ_1 (Eq. 4). The modeled radium profiles thus showed the highest sensitivity to Θ_1 in the region of the gradient (Fig. 3.2b).

Darcy velocities, determined from radium and chloride profiles of non-brine and brine seeps, respectively, spanned a range from approximately 0 to 0.25 m y^{-1} upward flow (Fig. 3.3). Confidence intervals tended to be larger for profiles associated with higher Darcy velocities (Fig. 3.3), but when normalized to the best-fit Darcy velocity did not reveal a clear trend with Péclet number. While 11 out of 12 analyzed radium profiles (Fig. 3.3)

Table 3.3: The boundary conditions of the state variables.

Variable	Upper b.c.	Lower b.c.
Solutes	Concentration (mol m^{-3})	Concentration (mol m^{-3})
O_2	0.225	0
SO_4^{2-}	28	0
Ca^{2+}	10.28	0
TA	2.40	20
TC	2.27	20
TS	0	0
CH_4	0	42.73
Tracer	0	1
Solids	Flux	Gradient
S_h	0	0
$CaCO_3$	0	0
Others		
ϕ_s	$w\phi_s = 1.2 \cdot 10^{-5}$ m y^{-1}	Zero gradient
p	0	$1.93 \cdot 10^{15}$ kg m^{-1} y^{-2}

All state variables use zero gradient boundary conditions on the left and right sides. With total alkalinity TA = $2[CO_3^{2-}]+ [HCO_3^-]+ [HS^-]+ [B(OH)_4^-]+ [OH^-]- [H^+]$, dissolved inorganic carbon TC = $[CO_3^{2-}]+ [HCO_3^-]+ [H_2CO_3]$, and total dissolved sulfide TS = $[HS^-]+ [H_2S]$; b.c. stands for boundary condition.

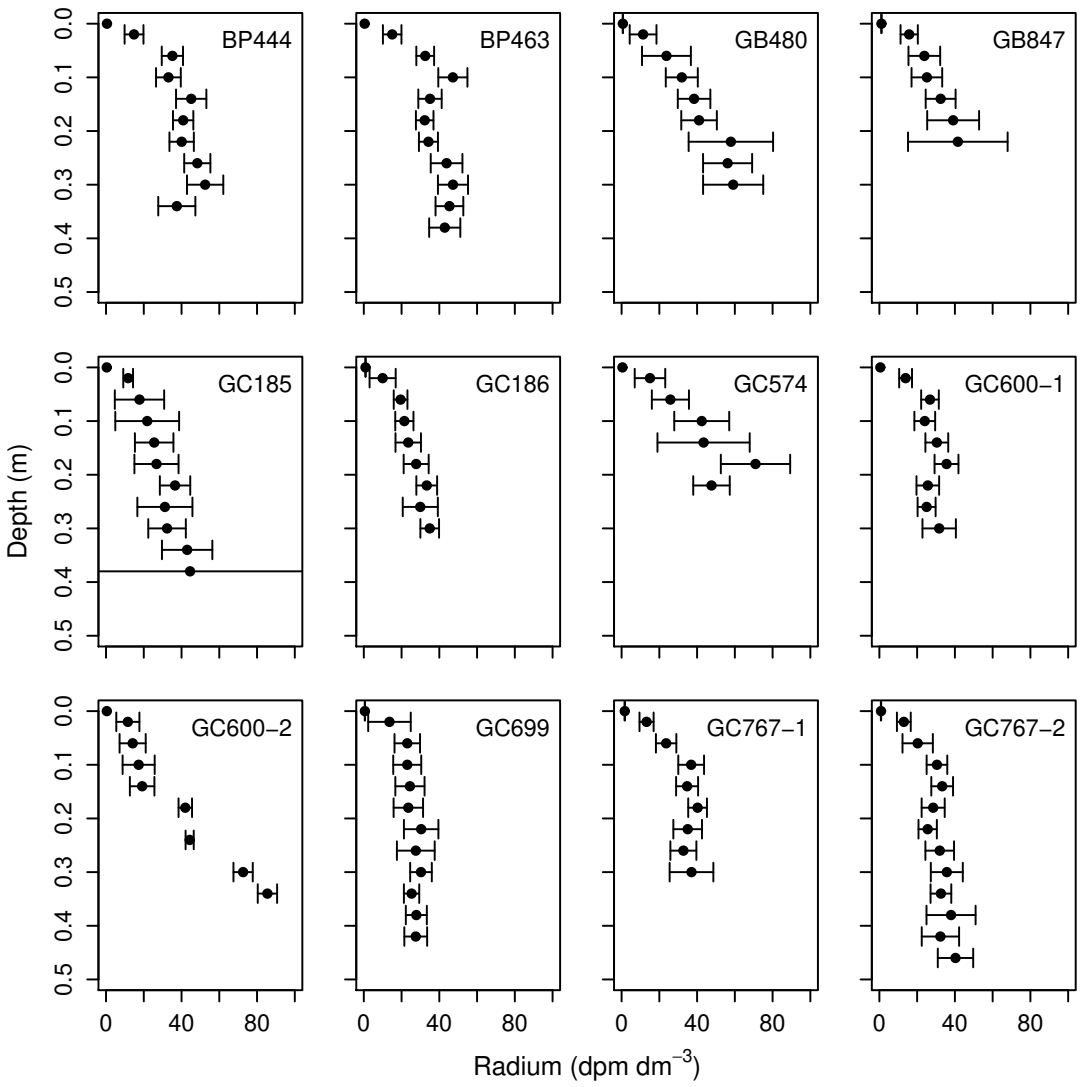

Figure 3.1: Measured radium profiles.

and 5 out of 9 analyzed chloride profiles exhibited the general patterns shown in Fig. 3.2a, five profiles had convex-down shapes. The latter can indicate downward flow, which can develop when gas is discharged from the sediment and replaced by water (O'Hara et al. 1995; Tryon and Brown 2001; Tryon and Brown 2004) or when gas bubbles streams induce turbulent down mixing of porewater (Haeckel et al. 2007). Bio-irrigation was likely not the cause of the convex-down shape of the profiles: Macrofauna were not observed in the core from which the 226Ra profile indicated negative flow (GC600-2, Figs. 3.1, 3.3). For the Cl^- profiles suggesting downward flow (GB425, Fig. 3.3), the signature of the overlying water

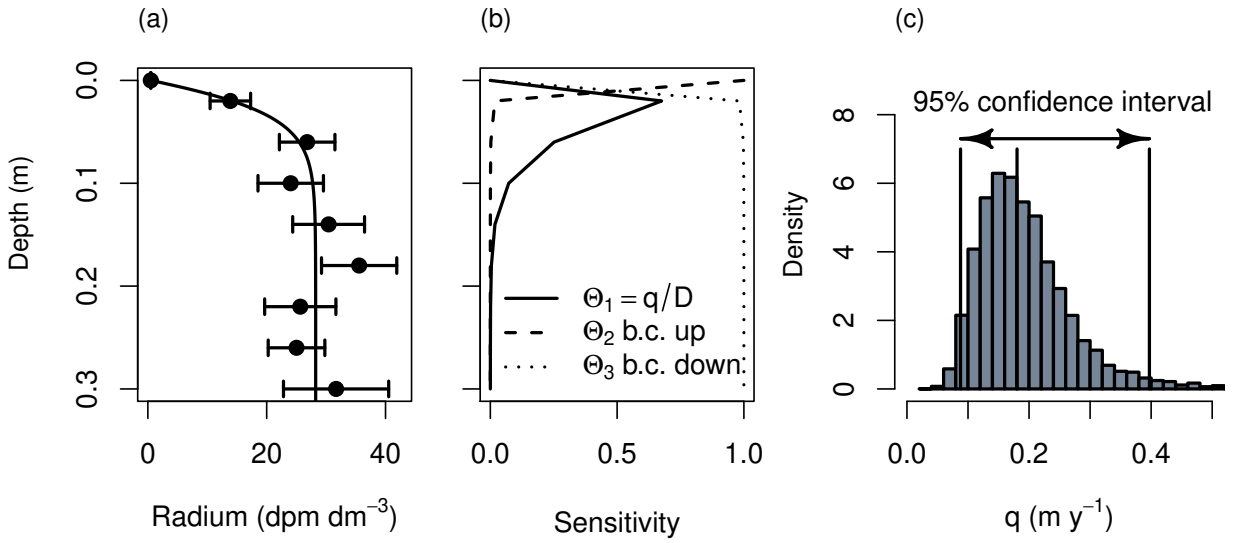

Figure 3.2: Example of radium profile GC600-1; (a) measured radium activities, along with fitted profile, (b) the local sensitivity of the simulated profile to the fitting parameters, (c) confidence interval based on Monte Carlo simulation. Θ_2 b.c. up and Θ_3 b.c. down denote the Ra activities at the upper and lower boundaries, respectively.

extended to $>$ 2 m depth (Castellini et al. 2006), and seep biota typically do not burrow that deep.

The range of downward and upward flow velocities (Fig. 3.3) is in accord with previous studies that determined the flow from conservative tracer profiles (e.g.,Lapham et al. 2008a and references therein). However, higher velocities extending to several meters per year up- and downward flow have been measured directly with flux meters (Tryon et al. 2002; Tryon and Brown 2004; Solomon et al. 2008). There are two possible explanations for such a discrepancy: First, velocities determined from tracer profiles at steady-state represent long-term averages. The characteristic time-scale for the ^{226}Ra profiles to approach steady state in the upper 10 cm of sediment is on the order of a month ($\tau = L^2/[4D]$; Malinverno 2010). When porewater velocities are affected by tidal oscillations, the displacement of the tracer during one phase of the tidal cycle will be small and counteracted by the next phase, and hence the tracer profiles will reflect the mean and not the peak velocities. Second, direct measurements are often conducted at locations that exhibit locally higher flow. The cores in this study, while collected in areas with known seepage, did not show surficial indicators of high flow, such as the presence of microbial mats or bivalves near the surface (Hovland 2002).

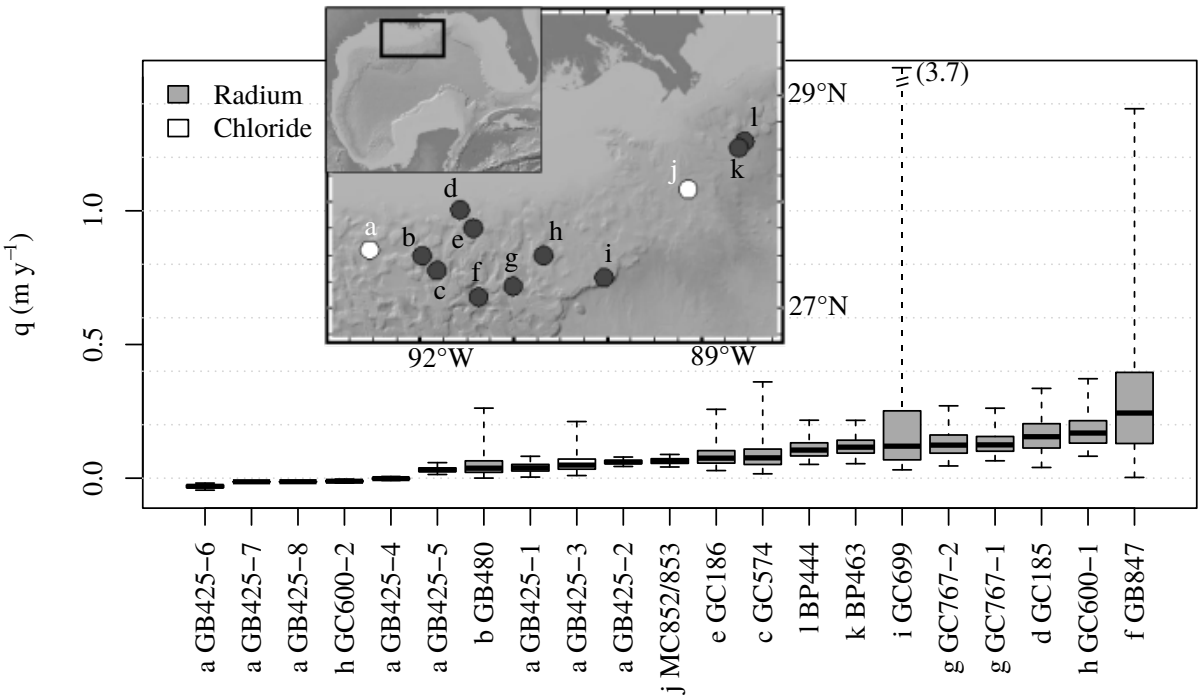

Figure 3.3: Darcy velocities obtained from fitting radium and chloride profiles, along with the confidence intervals. The map was created with GeoMapApp (Ryan et al. 2009).

Magnitude and effect of uncertainty in porewater flow

Absolute ^{226}Ra measurement errors typically increased with depth (Fig. 3.2a), and as a consequence, the uncertainty in Θ_3 (lower boundary condition) was substantially larger than that in Θ_2 (upper boundary condition). The 95% confidence interval of the Darcy velocity ($q = \Theta_1 D$, Eq. 3.4), established through the Monte Carlo simulation, showed a long-tailed distribution (Figs. 3.2c, 3.3). It represents the uncertainty caused by measurement errors and possibly the inadequacy of model assumptions.

Our estimates of Darcy velocities also depend on the diffusion coefficient ($q = \Theta_1 D$, Eq. 3.4). The diffusivities of most solutes in seawater can be estimated with an error less than 13% (Felmy and Weare 1991), and at non-brine seeps the aqueous diffusivity can be assumed to be constant with depth. To obtain this level of accuracy in the presence of large salinity gradients, diffusivities need to be corrected for changes in ionic strength (Haffert et al. 2013; Haffert and Haeckel 2019). Data compiled by Boudreau (1996) indicate that for a porosity above 0.6 the tortuosity can vary by 30 to 100%. This uncertainty in the tortuosity propagates directly into that of the Darcy velocity.

The uncertainty in effective diffusion coefficients can have a significant impact on estimates of benthic-pelagic coupling at cold seeps, which depend on accurate estimates of fluid flow. For example, Smith et al. (2014) constrained the Darcy velocity at site MC852/853 (Fig. 3.3) by fitting Cl^- profiles. They assumed a constant porosity and tortuosity and lumped these parameters implicitly in the effective diffusivity, which was set to $2.5 \cdot 10^{-10}$ m^2 s^{-1}. This value was taken from Dugan and Flemings (2000), who used it for a 600 m depth interval on the New Jersey continental slope, where pressure, temperature and porosity (which varied between 0.4 and 0.65, likely corresponding to different sediment tortuosity) differed from conditions in the upper sediment of MC852/853. With this effective diffusivity, a porewater Darcy velocity of 3 ± 2 cm y^{-1} was obtained. The temperature measurement indicated a source of heat beyond porewater flow, which was attributed to the flow of gas. Fitting the observed temperature profiles yielded a vertical gas velocity of 80 ± 20 cm y^{-1}, several orders of magnitude larger than previously estimated (National Research Council 2003). However, assuming a constant porosity of 0.7 (Castellini et al. 2006) and correcting for in-situ conditions (Boudreau 1997), we calculated an effective diffusivity of $5 \cdot 10^{-10}$ m^2 s^{-1}. Since this calculated diffusivity is twice as large as the one used by Smith et al. (2014), it yields a two times larger porewater Darcy velocity (6 cm y^{-1}; $q = \Theta_1 D$) and confidence interval. With this higher velocity, more heat is transported via the aqueous phase. Thus, the gas flow velocity needed to fit the temperature profile becomes much lower and its confidence interval larger, even encompassing 0. The high sensitivity of the estimated gas flow to the porewater flow follows from the 13-fold higher volumetric heat capacity of water compared to gas, and indicates the need for a careful assessment of the uncertainties.

3.3.2 Effects of spatially variable permeability

The spatially variable permeability field led to a spatially variable flow field in our 2D simulations. Here we analyze how this variability can affect flow estimates made with different experimental methods. . Simulated upward flow velocities at the sediment-water interface, where flux meters (e.g. Tryon et al. 1999) measure flow, varied from -70% to +211% relative to the domain-averaged Darcy velocity ($\bar{q}[t]$). Averaging the vertical velocities over the upper 20 cm, which corresponds to the typical depth of the measured ^{226}Ra profiles and hence is comparable to velocities inferred from fitting porewater profiles, yielded a narrower range of -60% to +83% (Fig. 3.4a). This lateral variability in vertical velocities implies that the width of a sediment core can have a substantial effect on the velocities obtained from measured conservative tracer profiles, as it determines the cross-sectional area over which the velocities are averaged. The variability quantified by computing the mean of the 0-20 cm depth-averaged Darcy velocity over a core width, with cores sampling across the entire model domain, ranged from -41% to +62% and -17% to 15% for 5 cm and 25 cm wide cores, respectively (Fig. 3.4b). Model simulations suggest that the spatial variability persists over time, even if the absolute Darcy velocity changes (see section 3.3.2 below). For example, in

a simulation in which the average velocity ($\bar{q}[t]$) decreased substantially from 0.51 to 0.27 m y^{-1} over a period of 100 years, the relative variation in flow ($q[x,t]/\bar{q}[t]$) remained rather constant (compare grey and black lines in Fig. 3.4a). The robustness of the observed patterns for random permeability fields with variances ($\sigma^2_{\log\kappa}$) between 0.2 and 1.0 has been confirmed through additional simulations in both 2D and 3D (see appendix B.1).

The presence of a preferential flow conduit obviously further increases the spatial variability in vertical flow (Fig. 3.4c,d). In this case, a strong feedback exists from solid formation as the Darcy velocity in the conduit decreases more rapidly than in the remainder of the sediment (see below, and compare grey and black lines in Fig. 3.4c).

To assess the horizontal variability in flow estimates derived from tracer profiles, we extracted 20 cm long vertical profiles from the simulated tracer field, starting at each grid point at the sediment-water interface. These were then fitted using Eq. 3.4 to determine a Darcy velocity from each of these profiles. Compared to the depth-averaged Darcy velocities derived from the simulated flow field (solid grey lines, Fig. 3.4a, c), these fitted velocities (dashed lines, Fig. 3.4a, c) exhibited broader and less pronounced peaks, which is caused by lateral diffusion of the tracer. The variance of velocities determined by fitting computed tracer profiles was $\sim$ 20% to 50% lower than those of the depth-averaged Darcy velocities from simulated flow fields (based on additional simulations, see appendix B.1). When tracer concentrations are averaged over a cross-sectional area, the range of fitted velocities for a core width (striped area, Fig. 3.4b) is smaller than the range of the laterally averaged computed velocities (grey area, Fig. 3.4b). This reduction is stronger with greater differences in local velocities, such as with a preferential flow conduit (compare of striped areas Fig. 3.4b,d).

3.3.3 Simulating the effect of solid formation on changes in flow over time

The interaction between early diagenesis and flow are first briefly described (for an in-depth discussion, see also Luff and Wallmann 2003 and Luff et al. 2005), and then the effect of dispersed hydrate formation and carbonate precipitation on flow and the fitting of tracer profiles are evaluated.

Early diagenesis

Anaerobic oxidation of methane has a large influence on the distribution of solids, as it produces the alkalinity needed for calcium carbonate precipitation and affects the depth interval over which methane concentrations are below saturation with respect to gas hydrate. The consumption of sulfate is driven by methane oxidation, and the sulfate concentration gradient (and hence the sulfate penetration depth) mirrors the rate of this process. The penetration depth increased from 4.5 to 7.5 cm in the time interval of 10 to 500 years (Fig. 3.5a), reflecting simultaneous decreases in the Darcy velocity (from 0.51 to 0.04 m y^{-1}), the

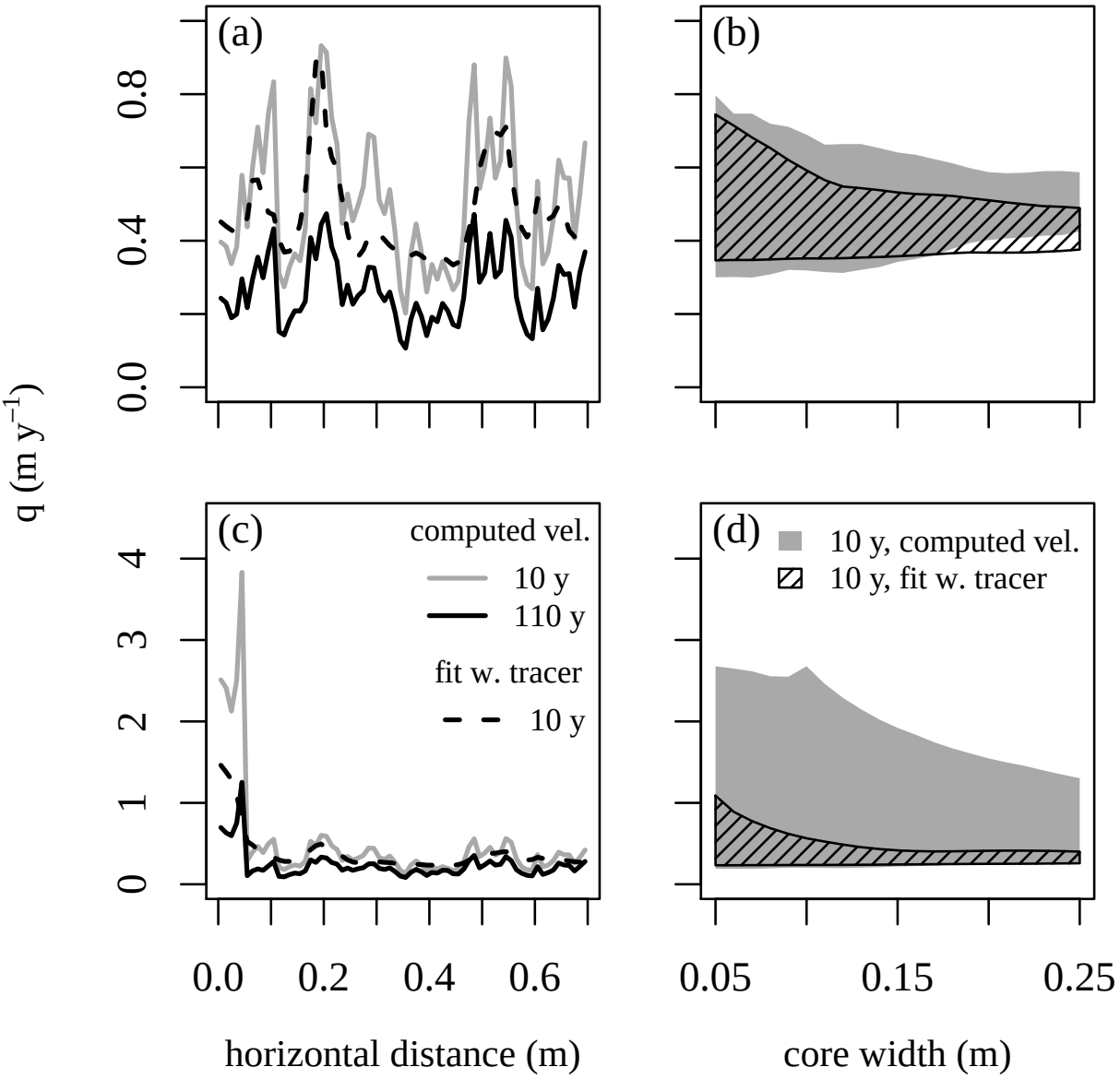

Figure 3.4: Simulated Darcy velocities averaged vertically over the top 0.2 m (solid lines) and Darcy velocities obtained from fitting simulated tracer distributions (dashed lines) for sediment with (c) and without (a) a preferential flow conduit in the leftmost 0.05 m. Panels (b) and (d) show the velocities obtained when averaging those shown in (a) and (c) across a width of 0.05 to 0.25 m; the vertical extent of the grey zone indicates the variability of Darcy velocities for a given core width, and the striped zones correspond to those constrained from fitting conservative tracers.

influx of methane (15.3 to 1.4 mol m^{-2} y^{-1}), and the sulfate reduction rate (3.1 to 1.3 mol m^{-2} y^{-1}). The efficiency of methane oxidation (defined as the spatially integrated reaction rate divided by the influx of CH_4 from below) increased from 23 to 30% during the time of 10 to 100 years, and the methane oxidation rate was larger than the influx of methane at 500 years, as a part of the substrate was produced in-situ through the dissolution of gas hydrate. Simulated methane concentration profiles exhibited a steep non-linear gradient in the upper sediment and a small linear increase with depth in the deeper sediment (Fig. 3.2a), indicating the transition from a region where the methane is below the gas hydrate equilibrium concentration to a region where it is controlled by the gas hydrate equilibrium concentration, which increases linearly with depth (Eq. 3.11). The gas hydrate zone retreated to greater depth over time (Fig. 3.5b) due to the decrease in methane influx. Calcium carbonate precipitated near the sediment-water interface, leading to a higher solid volume fraction (Fig. 3.5b) and the formation of a crust. This crust became thicker over time due the downward migration and thickening of the anaerobic methane oxidation zone, and also through the burial of carbonates. The calcium carbonate concentration peak was formed in the beginning of the simulation, and slowly moved down through burial to 3 cm after 500 years (Fig. 3.5b). Calcium carbonate precipitation rates gradually declined with time due to a decrease of the alkalinity production rate. This change reflects that the deceleration of flow led to a reduced flux of methane into the surface sediment, lowering the rate of anaerobic methane oxidation, despite an increase in oxidation efficiency.

The presence of a preferential flow conduit (Fig. 3.5e,f) led to (horizontally averaged) chemical profiles that were qualitatively similar to those without one. The methane and sulfate profiles exhibited more gradual gradients, reflecting lower velocities and reduced influx of methane outside the conduit. The solid volume fraction was higher in the conduit and lower in the remainder of the sediment, resulting in a laterally averaged profile that had a slightly lower and broader peak compared to the simulation without the conduit (Fig. 3.5e, inset of Fig. 3.6b). The hydrate stability zone was located closer to the sediment-water interface in the conduit than in the remainder of the sediment (inset of Fig. 3.6b), which resulted in a kink in the laterally averaged hydrate saturations (Fig. 3.5e).

Evolution of the flow field

The simulations showed a rapid deceleration of flow in the first 200 years and then a steady decline to a plateau value of $\sim$ 0.02 m y^{-1} (Fig. 3.6a). This pattern was observed across a wide range of imposed pressure gradients, corresponding to initial velocities ranging from 0.2 to 1.0 m y^{-1} (Fig. 3.6a). Calcium carbonate formation reduced the fluid volume fraction near the sediment-water interface across the width of the domain, and gas hydrates accumulated at greater depth (see inset of Fig. 3.6b). In the simulations with a preferential flow conduit, the high permeability zone experienced a stronger reduction in fluid volume fraction ($S_f\phi$, Eq. 3.14) and deceleration of flow with time (Fig. 3.6b). In all simulations,

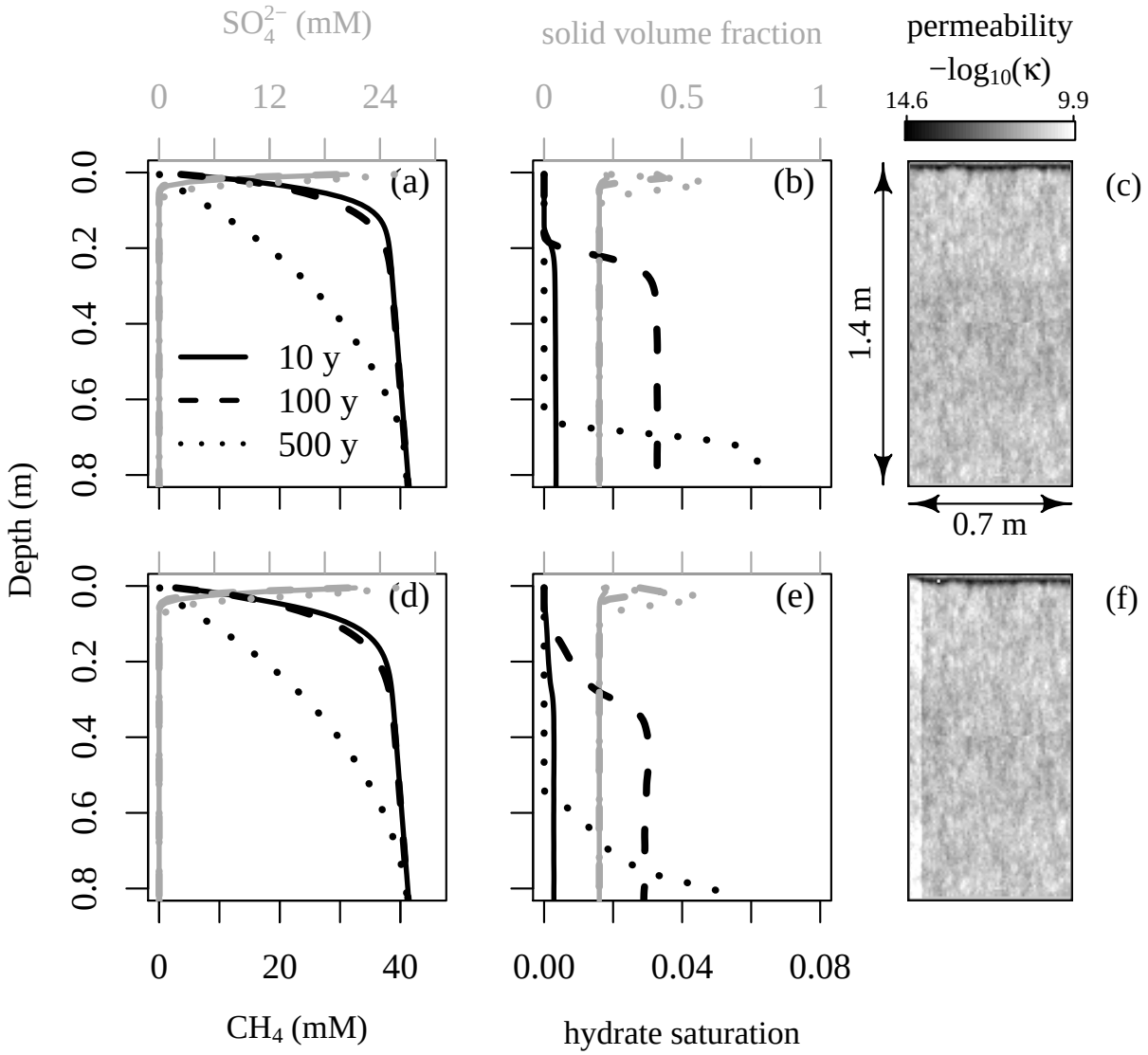

Figure 3.5: Depth profiles of (a,d) dissolved methane (black) and sulfate (grey) and (b,e) the hydrate saturation (black) and the solid volume fraction (grey), as simulated in the reaction-transport model after 10, 100, and 500 years (solid, dashed and dotted lines, respectively). Panels denote simulations with (d,e) and without (a,b) a preferential flow conduit in the leftmost 0.05 m of sediment. The values are averaged over the domain width; deviations of the solid volume fraction from its initial value (0.2) correspond to the calcium carbonate content. Panels c and f show the permeability fields of the simulations without (c) and with (f) conduit, respectively, after 325 years. Changes in permeability with time are reflected by those in the Darcy velocity (Fig. 3.6).

the deceleration caused by solid formation was stronger for faster flow and thus constituted a negative feedback. The time-scales of these processes on the order of decades to centuries is slow compared to the time of a tracer profile to approach steady state, and hence does not invalidate the steady-state assumption when fitting measured profiles to determine Darcy velocities. Sensitivity analyses indicated that the rate constant of anaerobic methane oxidation, the burial velocity, and the exponent in the permeability function (Eq. 3.14) can have a significant effect on the deceleration rate and stable plateau value of the Darcy velocity (see appendix A2).

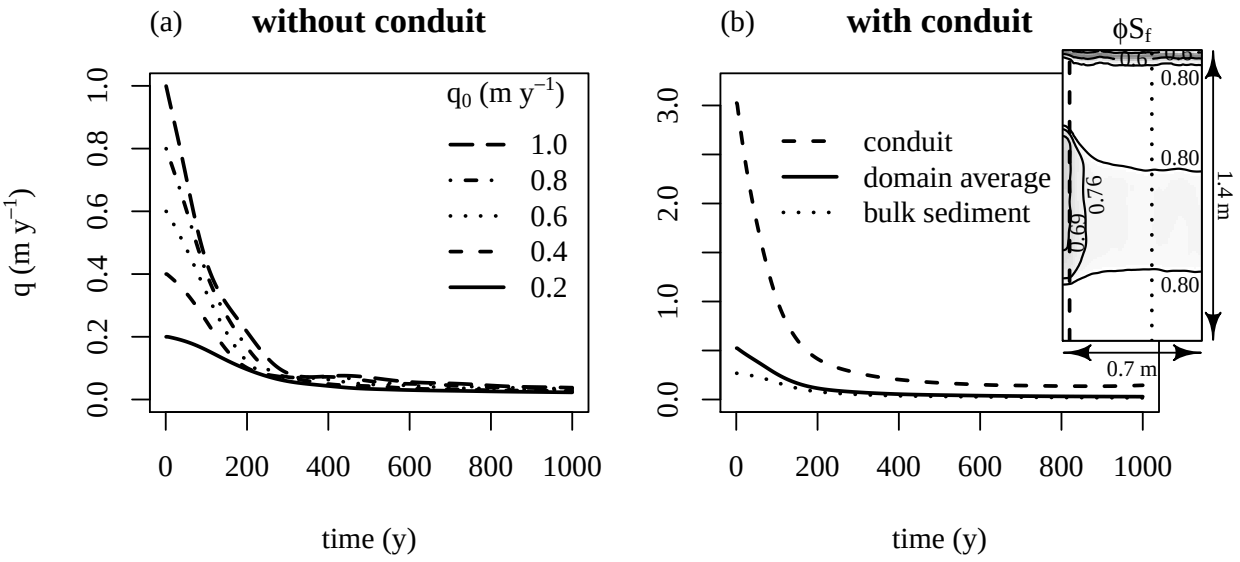

Figure 3.6: Average vertical flow velocities over time with (b) and without (a) a preferential flow conduit. Panel (a) denotes 5 simulations differing in the imposed vertical pressure gradient. Panel (b) denotes the vertical flow for a pressure gradient that corresponds to the initial Darcy velocity of 0.6 m/y in panel (a); the dashed and dotted lines are representative values for the preferential flow conduit and the bulk sediment, respectively, while the solid line denotes the domain average. The inset in panel(b) visualizes the water-saturated pore space (ϕS_f) as isolines in the preferential flow section (dashed vertical line) vs. the bulk sediment (dotted line) after 325 years.

The simulated patterns may apply to sites of mineral-prone features with slower flow. More complex flow can emerge when high fluid pressure in low permeability sediments can form fractures (Cavagna et al. 2015). At ancient and modern seep sites, tubular carbonate aggregates are present with horizontal and vertical orientations that served as conduits for water and gas flow (e.g. Aiello et al. 2001; Haas et al. 2010). The model is not designed to simulate the formation of fractures. Neither can it resolve morphologies of carbonates, such as tubes, nodules, shells, filled-molds (Haas et al. 2010), nor the shape of hydrates in nodules, lenses, or massive structures (e.g. MacDonald et al. 1994; Tréhu et al. 2004),

which can affect the flow path. At sites with slower seepage, solids carbonate slabs can form over time-scales longer than investigated here (Roberts and Aharon 1994; Teichert et al. 2003). In such settings, the tendency of solid formation to decelerate flow and to reduce the spatial heterogeneity by clogging preferential flow paths (Hovland 2002), as shown in the simulations, may help explain the relatively narrow range of velocities determined from measured tracer profiles (Fig. 3.3).

3.4 Conclusion

Seepage at multiple cold seep sites in the northern Gulf of Mexico have been quantified by fitting ^{226}Ra profiles with a 1D diffusion-advection model. The uncertainties in the fits are substantial, commonly on the same order of magnitude as the estimated flow velocities. They arise from uncertainties in the measurements, the tortuosity, and modeling assumptions, which are factors that apply to chemical tracer profiles in general.

Our work provides a foundation for a comparison between estimates of flow based on conservative tracer profiles and other approaches. For example, as estimates of gas flow based on temperature and salinity gradients are highly sensitive to the estimated porewater Darcy velocity, they tend to be less reliable than gas flux estimates based on field observations. Furthermore, our simulations illustrate the effect of the spatial variability on porewater flow estimates, and how it relates to collected sediment core size. The effect of temporal variability in external forcing depends on the characteristic time-scale, which for a tracer profile is on the order of a month. Fast oscillations, induced by the tide or short expulsion events, have a small or negligible effect on the tracer profiles. Flux meters can capture these shorter-lived signals, leading to higher extremes in up- and downward velocities with a similar mean. The formation of dispersed gas hydrates and carbonates tend to decrease the spatial variability in flow on time-scales of decades to centuries. The tracer profiles do not retain information of these changes, but adjust to changes in flow direction and magnitude during a month.

Chapter 4

The Effect of Redox Conditions and Bioirrigation on Nitrogen Isotope Fractionation in Marine Sediments[1]

[1]Rooze, J. and C. Meile (2016). In: *Geochimica et Cosmochimica Acta* 184, p. 227-239. Reprinted here with the permission of the publisher.

Abstract

Nitrogen isotopic signatures of sources and sinks of fixed nitrogen (N) can be used to constrain marine nitrogen budgets. However, the reported fractionation during benthic N_2 production varies substantially. To assess the range and mechanisms responsible for such observations, we conducted a model study to evaluate the extent to which nitrification, denitrification, and anaerobic ammonium oxidation contribute to the isotopic composition of in situ N_2 production. Different hydrodynamic regimes were taken into account, ranging from bioirrigation to diffusion-dominated transport. The benthic redox conditions were found to control the N isotope effect, which under reducing conditions is driven by fractionation during nitrification and anaerobic ammonium oxidation and under oxidizing conditions by fractionation during denitrification. Environmental parameters, such as the mineralization rate, the bioirrigation intensity, and chemical composition of the overlying water affect the benthic redox zonation and therefore also the benthic N isotope effect. The N isotope effect of benthic N_2 production was computed for a wide range of bioirrigation intensities and mineralization rates, and found to be approximately -3‰ for commonly encountered conditions. This value is similar to previous estimates of the global N isotope effect of benthic N_2 production, which provides a strong constraint on the relative importance of water column vs. benthic N_2 production.

4.1 Introduction

The availability of nitrogen (N) is considered one of the main controls of primary production in the ocean (Sarmiento and Gruber 2006). Marine fixed N inventories are regulated mainly by microbial processes, which can induce N isotope effects by consuming or producing ^{14}N and ^{15}N species at slightly different rates. Therefore, the contributions from different sources and sinks to the bioavailable oceanic N pool can not only be determined from measured fluxes, but also constrained from their isotopic signatures (Montoya 2008).

Globally, nitrogen fixation is the largest source and N_2 production through denitrification (DNF) and anaerobic ammonium oxidation (anammox) represent the major sinks of bioavailable N in the ocean. N fixation introduces N with a $\delta^{15}N$ of -1 ± 1‰($\delta^{15}N = \{[^{15}N/^{14}N]/[^{15}N/^{14}N]_{\text{standard}} - 1\} \cdot 1000$‰; Minagawa and Wada 1986; Carpenter et al. 1997). Anammox is carried out by chemolithoautotrophic bacteria that gain energy from the reaction of ammonium (NH_4^+) with NO_2^- to N_2, with an N isotope effect of -16‰ for NO_2^- reduction and approximately -26‰ for NH_4^+ oxidation (Brunner et al. 2013). During DNF, nitrate (NO_3^-) is reduced through several intermediates, including nitrite (NO_2^-) to dinitrogen gas (N_2). Although fractionation can occur during each step, the overall N isotope effect of the DNF pathway is affected most by the step in which a nitrogen-oxygen bond of a nitrate ion bound to nitrate reductase is cleaved (Shearer et al. 1991). In laboratory studies with marine denitrifying bacteria, fractionation by -5 to -30‰ has been measured, depending

on the specific denitrifier species and experimental conditions (Wellman et al. 1968; Granger et al. 2008; Kritee et al. 2012).

Strong N isotope fractionation of $-25 \pm 5‰$ has been reported to occur during N_2 production in oxygen minimum zones (Brandes et al. 1998; Altabet et al. 1999; Sigman et al. 2003). Due to this fractionation, NO_x (NO_2^- + NO_3^-) tends to become locally enriched in ^{15}N, which counters the discrimination against the preferential consumption of ^{14}N and diminishes the effect on the bulk oceanic fixed $\delta^{15}N$ (Deutsch et al. 2004). Thus, the apparent enrichment factor of water-column N_2 production is likely substantial, but less negative than the organism-level N isotope effect. In sediments the apparent N isotope effect was thought to be close to zero, since initial studies showed that the bottom water $\delta^{15}N$-NO_x did not change during incubation experiments (Brandes and Devol 1997; Brandes and Devol 2002; Lehmann et al. 2004). More recent studies have called the assumption of negligible N isotope fractionation into question. Firstly, fractionation during nitrification can produce light NOx substrate for N_2 production and lead to exchange fluxes of heavy reduced N (NH_4^+ + dissolved organic nitrogen [DON]) from the sediment to the overlying water, which then increases the ocean fixed $\delta^{15}N$ (Granger et al. 2008; Alkhatib et al. 2012). Secondly, NO_x exchange fluxes have been found to directly communicate the benthic N isotope effect to the overlying water (e.g. Dale et al. 2014), which is consistent with observations in incubation experiment showing that N isotope fractionation during DNF led to heavier bottom water NO_3^- (Dähnke and Thamdrup 2013).

In this study, we assess N isotope fractionation in sediments that are inhabited in bottom dwelling organisms. In particular near-shore environments are commonly inhabited by benthic infauna, which often are critical in shaping their habitat (Meysman et al. 2006a; Archer and Devol 1992; Volkenborn et al. 2007). They enhance solute transport in sediments (Meile and Cappellen 2003), increase benthic mineralization rates (Aller and Aller 1998; Kristensen 2001; D'Andrea and DeWitt 2009), and promote higher coupled nitrification-N_2 production rates (Grundmanis and Murray 1977; Na et al. 2008). The study of sediment N cycling is particularly relevant on continental shelves, which host 50 - 65% of the global benthic N_2 production (Middelburg et al. 1996; Bianchi et al. 2012; Bohlen et al. 2012). Approximately 70% of continental shelf sediments are permeable (Emery 1968), so that advective transport typically dominates solute transport (Hüttel et al. 2003). Flow circulating through such sediment may introduce NO_3^- that is only partially consumed in situ, leaving the efflux enriched in heavy N to potentially communicate the N isotope effect of N_2 production to the overlying water. Kessler et al. (2014) found that N_2 production in a column experiment with current-induced flow led to a N isotope effect of approximately $-2.8‰$. However, the effect of bioirrigation on benthic N isotope cycling has not yet been studied in detail. Here we present a mechanistic, early diagenetic process model to quantify the N isotope effect in sediment surrounding a burrow and identify the role of the redox conditions and advection induced by infauna in controlling the N isotope effect of benthic N_2 production.

4.2 Methods

4.2.1 Reaction-transport model

The mechanistic model simulated the effects of sediment early diagenesis in the presence of pumping infauna on the isotopic signature of benthic N fluxes. A 2D axisymmetric domain represented the physical 3D cylindrical environment surrounding a burrow, following the lugworm model of Meysman et al. (2006b). The domain radius was 10 cm, which corresponds to a population density of ∼32 individual organisms m^{-2}. The uppermost 2 cm of the domain represented the bottom water, overlying 20 cm of sediment. A burrow feeding pocket was implemented as a fluid injection site of radius 2.5 mm located at 15 cm depth, with a feeding funnel above it that had a 10 times higher permeability than the rest of the sediment (Jones and Jago 1993; Riisgard and Banta 1998).

The method described in Dornhoffer et al. (2015) was used to simulate fluid flow. In short, flow velocities were calculated using the Navier-Stokes and Darcy-Brinkman equations (Le Bars and Worster 2006), accounting for pressure forces and shear stress in the momentum balance. Fluid was injected into the sediment at a constant rate by imposing a normal velocity on the boundary of the feeding pocket. Symmetry conditions with zero normal flow were imposed at the outer cylinder boundaries. Zero normal flow was imposed at the bottom of the domain, while the top boundary allowed for fluid to escape.

The steady-state distribution of dissolved species was described by the following mass balance equation:

$$0 = \nabla \cdot (\phi D_i \nabla C_i - \phi v C) + R \tag{4.1}$$

where D_i is the diffusion coefficient, C_i is the concentration, ϕ is the porosity (set to 1 in the overlying water), v is the velocity vector, and R is the net reaction rate. The molecular diffusion coefficients D_i^{mol} were calculated following Boudreau (1997) at a temperature of 5 °C and a salinity of 35. In the bottom water the diffusion coefficient was the sum of D_i^{mol} and the eddy diffusion coefficient calculated with the Reichardt equation (Boudreau 2001):

$$D_i = D_i^{\mathrm{mol}} + \kappa z u^* \left[1 - \frac{11\nu}{z u^*} \tanh\left(\frac{z u^*}{11\nu} \right) \right] \tag{4.2}$$

where κ is the dimensionless von Karman constant (0.4), z is the distance from the sediment-water interface, u^* is the shear velocity (set to 10^{-3} m s^{-1}), and ν is the kinematic viscosity (10^{-6} m^2 s^{-1}). The diffusion coefficient in the sediment was corrected for tortuosity in the porous medium following Boudreau (1996):

$$D_i = \frac{D_i^{\mathrm{mol}}}{1 - 2\log\phi} \tag{4.3}$$

The reaction network (Table 4.1) described mineralization of dissolved organic matter (DOM) in the sediment with aerobic respiration, DNF, and dissimilatory iron oxide ($Fe(OH)_3$) and sulfate (SO_4^{2-}) reduction. The various mineralization reactions of labile DOM with different electron acceptors use a first-order rate law with respect to DOM concentration (Table 4.2). NO_2^- was accounted for explicitly to implement anammox and to act as an intermediate in the DNF and nitrification reactions. Sulfide (HS^-) and dissolved iron (Fe^{2+}) can be reoxidized or form a FeS precipitate (Table 4.1). Reaction rates were set to zero in the overlying water, and processes such as dissimilatory nitrate reduction to ammonium, ammonium assimilation, or benthic primary production, which may become important in shallower waters, are not included. Strong mixing of the sediment by macrofauna was assumed to lead to a homogeneous distribution of solids in the sediment, and POM and $Fe(OH)_3$ concentrations were held constant over the domain depth.

The parameterization of the baseline simulation was based on literature values, and within the reported ranges adapted to the setting of Brandes and Devol (1997). The measured benthic exchange fluxes of inorganic N and the N_2 production rate were fitted by adjusting the benthic DOM production rate, the rate constants and half-saturation constants of nitrification, DNF, and anammox, and by adjusting the fractionation factors associated with NH_4^+ consumption during anammox and nitrification (Table 4.3). At the top of the domain, known concentrations were imposed. For this, the bottom water concentrations of O_2 and NO_3^- and the $\delta^{15}N$ of NO_3^- and organic matter reported by Brandes and Devol (1997) were used (Table 4.3). The concentrations in the oxygenated bottom water of reduced species NO_2^-, NH_4^+, Fe^{2+}, and HS^- were set to zero, and the DOM concentration was set to 50 µmol (Lønborg and Søndergaard 2009). The same concentrations were also imposed at the feeding pocket, except that respiration by the macrofauna was assumed to produce NH_4^+ and lead to a 60% oxygen drawdown in the fluid injected (Table 4.3). No flux conditions were imposed at the domain sides and bottom.

The model was implemented in COMSOL4.4 using the "Free and Porous Media Flow" and "Solute Transport" application modes. The domain was discretized with approximately 23,000 triangular elements, with element sizes ranging from about 60 µm to 1 cm. The mesh was finest near the feeding funnel and SWI in order to resolve sharp concentration gradients accurately. All simulations were run dynamically to steady state.

4.2.2 Nitrogen isotope fractionation

For the dissolved N species separate state variables were included to account for ^{14}N and ^{15}N. N isotope fractionation occurred through multiplying rate constants of the ^{15}N species by fractionation factors, which are defined as $\alpha = (R_h/R_l)/(^{15}N/^{14}N)_{substrate}$, where R_h and

Table 4.1: Reaction pathways

Primary redox reactions*	
R_1	$(CH_2O)_a(NH_3)_{b(aq)} + a\,O_2 \longrightarrow a\,CO_2 + fb\,{}^{14}NH_4^+ + (1-f)b\,{}^{15}NH_4^+ + aH_2O$
R_2^l	$(CH_2O)_a(NH_3)_{b(aq)} + \frac{4}{3}a\,{}^{14}NO_2^- + (\frac{4}{3}a+b)H^+ \longrightarrow a\,CO_2 + fb\,{}^{14}NH_4^+ + (1-f)b\,{}^{15}NH_4^+ + \frac{2}{3}a\,{}^{14}N_2 + \frac{5}{3}aH_2O$
R_2^h	$(CH_2O)_a(NH_3)_{b(aq)} + \frac{4}{3}a\,{}^{15}NO_2^- + (\frac{4}{3}a+b)H^+ \longrightarrow a\,CO_2 + fb\,{}^{14}NH_4^+ + (1-f)b\,{}^{15}NH_4^+ + \frac{2}{3}a\,{}^{15}N_2 + \frac{5}{3}aH_2O$
R_3^l	$(CH_2O)_a(NH_3)_{b(aq)} + 2a\,{}^{14}NO_3^- + bH^+ \longrightarrow a\,CO_2 + fb\,{}^{14}NH_4^+ + (1-f)b\,{}^{15}NH_4^+ + 2a\,{}^{14}NO_2^- + aH_2O$
R_3^h	$(CH_2O)_a(NH_3)_{b(aq)} + 2a\,{}^{15}NO_3^- + bH^+ \longrightarrow a\,CO_2 + fb\,{}^{14}NH_4^+ + (1-f)b\,{}^{15}NH_4^+ + 2a\,{}^{15}NO_2^- + aH_2O$
R_4	$(CH_2O)_a(NH_3)_{b(aq)} + 4a\,Fe(OH)_3 + (8a+b)H^+ \longrightarrow a\,CO_2 + fb\,{}^{14}NH_4^+ + (1-f)b\,{}^{15}NH_4^+ + 4a\,Fe^{2+} + 11aH_2O$
R_5	$(CH_2O)_a(NH_3)_{b(aq)} + \frac{1}{2}a\,SO_4^{2-} + (\frac{1}{2}a+b)H^+ \longrightarrow a\,CO_2 + fb\,{}^{14}NH_4^+ + (1-f)b\,{}^{15}NH_4^+ + \frac{1}{2}a\,HS^- + aH_2O$
Other reactions	
R_6^{ll}	${}^{14}NH_4^+ + {}^{14}NO_2^- \longrightarrow {}^{14}N_2 + 2\,H_2O$
$R_6^{NO_2^h}$	${}^{14}NH_4^+ + {}^{15}NO_2^- \longrightarrow {}^{14}N\,{}^{15}N + 2\,H_2O$
$R_6^{NH_4^h}$	${}^{15}NH_4^+ + {}^{14}NO_2^- \longrightarrow {}^{14}N\,{}^{15}N + 2\,H_2O$
R_6^{hh}	${}^{15}NH_4^+ + {}^{15}NO_2^- \longrightarrow {}^{15}N_2 + 2\,H_2O$
R_7^l	${}^{14}NH_4^+ + \frac{3}{2}\,O_2 + 2\,HCO_3^- \longrightarrow {}^{14}NO_2^- + 3\,H_2O + 2\,CO_2$
R_7^h	${}^{15}NH_4^+ + \frac{3}{2}\,O_2 + 2\,HCO_3^- \longrightarrow {}^{15}NO_2^- + 3\,H_2O + 2\,CO_2$
R_8^l	${}^{14}NO_2^- + \frac{1}{2}O_2 \longrightarrow {}^{14}NO_3^-$
R_8^h	${}^{15}NO_2^- + \frac{1}{2}O_2 \longrightarrow {}^{15}NO_3^-$
R_9	$HS + 2\,O_2 \longrightarrow SO_4^{2-} + H^+$
R_{10}	$Fe^{2+} + \frac{1}{4}O_2 + 2\,HCO_3^- + \frac{1}{2}H_2O \longrightarrow Fe(OH)_3 + 2\,CO_2$
R_{11}	$Fe^{2+} + HS^- \longrightarrow FeS\,H^+$
R_{12}	$(CH_2O)_a(NH_3)_{b(s)} \longrightarrow (CH_2O)_a(NH_3)_{b(aq)}$

* $CH_2O)_a(NH_3)_{b(aq)}$ and $CH_2O)_a(NH_3)_{b(s)}$ refer to dissolved and particulate organic matter, respectively. 'a' and 'b' subscripts refer to the C:N ratio in organic matter, which was set to 106:16.

Table 4.2: Rate laws

Primary redox reactions

$$R_1 = k_{\mathrm{DOM}} C_{\mathrm{DOM}} \frac{[\mathrm{O_2}]}{[\mathrm{O_2}]+K_{\mathrm{m,O_2}}}$$

$$R_2^{\mathrm{l}} = \left(k_{\mathrm{DOM}} C_{\mathrm{DOM}} - R_1\right) \frac{[^{14}\mathrm{NO_2^-}]}{[^{14}\mathrm{NO_2^-}]+[^{15}\mathrm{NO_2^-}]+K_{\mathrm{m,NO}_x}}$$

$$R_2^{\mathrm{h}} = \alpha_{\mathrm{NO_2,DNF}} \left(k_{\mathrm{DOM}} C_{\mathrm{DOM}} - R_1\right) \frac{[^{15}\mathrm{NO_2^-}]}{[^{14}\mathrm{NO_2^-}]+[^{15}\mathrm{NO_2^-}]+K_{\mathrm{m,NO}_x}}$$

$$R_3^{\mathrm{l}} = \left(k_{\mathrm{DOM}} C_{\mathrm{DOM}} - R_1 - R_2^{\mathrm{l}} - R_2^{\mathrm{h}}\right) \frac{[^{14}\mathrm{NO_3^-}]}{[^{14}\mathrm{NO_3^-}]+[^{15}\mathrm{NO_3^-}]+K_{\mathrm{m,NO}_x}}$$

$$R_3^{\mathrm{h}} = \alpha_{\mathrm{NO_3,DNF}} \left(k_{\mathrm{DOM}} C_{\mathrm{DOM}} - R_1 - R_2^{\mathrm{l}} - R_2^{\mathrm{h}}\right) \frac{[^{15}\mathrm{NO_3^-}]}{[^{14}\mathrm{NO_3^-}]+[^{15}\mathrm{NO_3^-}]+K_{\mathrm{m,NO}_x}}$$

$$R_4 = \left(k_{\mathrm{DOM}} C_{\mathrm{DOM}} - R_1 - R_2^{\mathrm{l}} - R_2^{\mathrm{h}} - R_3^{\mathrm{l}} - R_3^{\mathrm{h}}\right) \frac{[\mathrm{Fe(OH)_3}]}{[\mathrm{Fe(OH)_3}]+K_{\mathrm{m,Fe(OH)_3}}}$$

$$R_5 = \left(k_{\mathrm{DOM}} C_{\mathrm{DOM}} - R_1 - R_2^{\mathrm{l}} - R_2^{\mathrm{h}} - R_3^{\mathrm{l}} - R_3^{\mathrm{h}} - R_4\right) \frac{[\mathrm{SO_4^{2-}}]}{[\mathrm{SO_4^{2-}}]+K_{\mathrm{m,SO_4}}}$$

Other reactions

$$R_6^{\mathrm{ll}} = k_{\mathrm{amx}} [^{14}\mathrm{NO_2^-}] \frac{[^{14}\mathrm{NH_4^+}]}{[^{14}\mathrm{NH_4^+}]+[^{15}\mathrm{NH_4^+}]+K_{\mathrm{m,NH_4}}}$$

$$R_6^{\mathrm{NO_2^}h} = \alpha_{\mathrm{NO_2,amx}} k_{\mathrm{amx}} [^{15}\mathrm{NO_2^-}] \frac{[^{14}\mathrm{NH_4^+}]}{[^{14}\mathrm{NH_4^+}]+[^{15}\mathrm{NH_4^+}]+K_{\mathrm{m,NH_4}}}$$

$$R_6^{\mathrm{NH_4^}h} = \alpha_{\mathrm{NH_4,amx}} k_{\mathrm{amx}} [^{14}\mathrm{NO_2^-}] \frac{[^{15}\mathrm{NH_4^+}]}{[^{14}\mathrm{NH_4^+}]+[^{15}\mathrm{NH_4^+}]}$$

$$R_6^{\mathrm{hh}} = \alpha_{\mathrm{NO_2,amx}} \alpha_{\mathrm{NH_4,amx}} k_{\mathrm{amx}} [^{15}\mathrm{NO_2^-}] \frac{[^{15}\mathrm{NH_4^+}]}{[^{14}\mathrm{NH_4^+}]+[^{15}\mathrm{NH_4^+}]}$$

$$R_7^{\mathrm{l}} = k_t ext AO [\mathrm{O_2}] \frac{[^{14}\mathrm{NH_4^+}]}{[^{14}\mathrm{NH_4^+}]+[^{15}\mathrm{NH_4^+}]+K_{\mathrm{m,NH_4}}}$$

$$R_7^{\mathrm{h}} = \alpha_{\mathrm{NH_4,ox}} k_{\mathrm{AO}} [\mathrm{O_2}] \frac{[^{15}\mathrm{NH_4^+}]}{[^{14}\mathrm{NH_4^+}]+[^{15}\mathrm{NH_4^+}]+K_{\mathrm{m,NH_4}}}$$

$$R_8^{\mathrm{l}} = k_{\mathrm{NO}} [\mathrm{O_2}] [^{14}\mathrm{NO_2^-}]$$

$$R_8^{\mathrm{h}} = \alpha_{\mathrm{NO_2,ox}} k_{\mathrm{NO}} [\mathrm{O_2}] [^{15}\mathrm{NO_2^-}]$$

$$R_9 = k_{\mathrm{HS}} [\mathrm{O_2}] [\mathrm{HS^-}]$$

$$R_{10} = k_{\mathrm{Fe}} [\mathrm{O_2}] [\mathrm{Fe^{2+}}]$$

$$R_{11} = \max\left[0,\ k_{\mathrm{FeS}} \left(\frac{[\mathrm{Fe^{2+}}][\mathrm{HS^-}]}{K_{\mathrm{FeS}}[\mathrm{H^+}]} - 1\right)\right]$$

$$R_{12} = F_{\mathrm{DOM,prod}} / L$$

L refers to the length of the modeled sediment domain, which is 20 cm.

R_l are the rates of reactions that consume ^{15}N and ^{14}N species, respectively (Table 4.2; Mariotti et al. 1981). The fractionation factors were generally less than 1, reflecting enzymatic discrimination against heavy N (Table 4.3). The only exception was NO_2^- oxidation, which has an inverse N isotope effect (Casciotti 2009).

The effect of the benthos on the isotopic composition of fixed N in the ocean is determined by the fluxes and isotopic composition of inorganic and organic N across the sediment-water interface. At steady-state the sum of these fluxes have to balance the magnitude and isotopic composition of the in situ N_2 production, since DNF and anammox are the only sinks of N in the model. Therefore, the isotopic composition of the in situ produced gas can be used to quantify the N isotope effect (ϵ_{sed}):

$$\epsilon_{\text{sed}} = \left[\frac{(^{15}\text{N}/^{14}\text{N})_{\text{N}_2\text{ production}}}{(^{15}\text{N}/^{14}\text{N})_{\text{bottom-water NO}_3^-}} - 1 \right] \cdot 10^3 \tag{4.4}$$

where the N_2 production rates are defined as:

$$\frac{4}{3} R_2^l + R_6^{\text{NO}_2\text{i}} + R_6^{\text{NH}_4\text{i}} + 2R_6^{\text{ii}} \tag{4.5}$$

with i=h for ^{15}N and l for ^{14}N; ii denotes anammox using nitrite and ammonium that are both heavy or light, respectively (Table 4.1). Burial of organic N is not taken into account, since the flux is small compared to the benthic and water-column N_2 production rates (Brandes and Devol 2002).

The model can be used to quantify the contribution of individual processes to the isotopic composition of N_2 produced in the sediment and hence the overall benthic N isotope effect,

$$\epsilon_{\text{sed}} \approx \delta^{15}\text{N-N}_2 - \delta^{15}\text{N-NO}_{3\,,\text{bw}}^- \tag{4.6}$$

where δ^{15}N-N_2 and δ^{15}N-$NO_{3\,,\text{bw}}^-$ are the isotopic composition of the in situ produced N_2 gas and NO_3^- in the overlying water, respectively. The isotopic composition of N_2 produced from different sources in the absence of fractionation can be approximated by:

$$\delta^{15}\text{N-N}_2 = f_1\delta_1 + \ldots + f_n\delta_n \tag{4.7}$$

where f_i refers to the fraction of source i (with signature δ_i). Fractionation in the conversion of substrate s to product p can be expressed as

$$\delta p \approx \delta s + \epsilon \tag{4.8}$$

Combining equations 4.7 and 4.8 yields:

$$\begin{aligned} \delta_{N_2} &= f_1\delta_1 + f_1\epsilon_1 + \ldots f_n\delta_n + f_n\epsilon_n \\ &= A + \sum f_i\epsilon_i \end{aligned} \tag{4.9}$$

Substitution into Eq. 4.6 shows that a simulation with all the fractionation factors (α, Table 4.3) set to 1, which turns off fractionation in the model, yields an apparent N isotope effect (ϵ_j) that accounts for sources with a different N isotopic composition (organic N and bottom water NO_3^-) and is reflected in the parameter A (Eq. 4.9)

$$\epsilon_0 = A - \delta^{15}\text{N-NO}_{3,\text{bw}}^- \tag{4.10}$$

Next simulations were run with a single fractionation factor having its original value and all the others set to 1, which yields an apparent N isotope effect (ϵ_j). The apparent N isotope effect of individual processes ($\epsilon_k = \epsilon_j - \epsilon_0$) can then be combined to yield the overall benthic N isotope effect

$$\epsilon_{\text{sed}} = \epsilon_0 + \sum \epsilon_k \tag{4.11}$$

The effect of the areal bioirrigation intensity on benthic N isotope cycling was examined by changing the pumping rate (Q, Table 4.3) and organism density, i.e. the domain radius. Simulations with a burrowing depth of 5 cm were performed to analyze the impact of shallow bioirrigation. The in situ DOM production rate ($F_{\text{DOM,prod}}$, Table 4.3), DOM reactivity (k_{DOM}, Table 4.3), and the composition of the overlying water ($O_{2,\text{bw}}$ and $NO_{3,\text{bw}}^-$, Table 4.3) were varied to evaluate the benthic N isotope effect in different environmental settings.

Finally, sediment N fractionation was quantified for a wide range of mineralization rates and areal bioirrigation intensities. The latter is the pumping rate of an individual organism (Q, Table 4.3) divided by the domain surface area ($A = \pi r^2$, Table 4.3). In total 198 simulations were carried out in which the bioirrigation intensity and mineralization rates were varied from 4.6 to 91.7 L m^{-2} d^{-1} and 0.36 to 29.73 mmol m^{-2} d^{-1}, respectively. Since burrowing macrofauna are dependent on the availability of POM as food source (Künitzer et al. 1992), sediment mineralization rates and bioirrigation intensities are often related. Two empirical relationships from literature were employed to provide a first order estimate of commonly encountered conditions, using the total sediment community oxygen consumption (SCOC) as a measure for the mineralization rate. The first relationship is based on an estimate of non-diffusive sediment O_2 uptake (see Eq. 1 in Meile and Cappellen 2003), which we tentatively assume to be due to bioirrigation. Recasting that equation and assuming a negligible amount of O_2 in the sediment porewater yields:

$$\frac{Q}{A} = \frac{\text{SCOC}}{O_{2,\text{bw}}}\left(1 - \frac{1}{1.292 + 0.073 \cdot \text{SCOC}}\right) \cdot 1000 \tag{4.12}$$

where Q/A is in L m^{-2} d^{-1}, SCOC corresponds to the mineralization rate in mmol C m^{-2} d^{-1}, and $O_{2,bw}$ is the oxygen bottom water concentration in µM (Table 4.3).

Table 4.3: Parameters used in reaction-transport model (baseline)

Description	Symbol	Value	Source
Environmental parameters			
Bottom water O_2 concentration	$O_{2,bw}$	150 µM	a
Bottom water NO_3^- concentration	$NO_{3,bw}^-$	23 µM	a
Isotopic composition bottom water NO_3^-	δ^{15}N-$NO_{3,bw}^-$	7.6‰	a
Isotopic composition organic N	Org. δ^{15}N	7.0‰	a
Bottom water DOM concentration	DOM_{bw}	50 µM	b
Injected O_2 concentration	$O_{2,inj}$	$0.4 \cdot O_{2,bw}$	c
Injected NH_4^+ concentration	$NH_{4,inj}^+$	8 µM	d
Imposed $Fe(OH)_3$ concentration	$Fe(OH)_3$	5 mM	
N:C of POM and DOM	N:C	16:106	
Porosity	ϕ	0.4	
Acidity	pH	8.1	
In situ DOM production	$F_{DOM,prod}$	4 mmol C m^{-2} d^{-1}	e
Pumping rate	Q	0.62 mL min^{-1}	e
Rate constants			
DOM production	k_{DOM}	$2 \cdot 10^{-5}$ s^{-1}	f
Anammox	k_{amx}	$1.7 \cdot 10^{-5}$ s^{-1}	e
NH_4^+ oxidation	k_{AO}	$1.5 \cdot 10^{-5}$ s^{-1}	e
NO_2^- oxidation	k_{NO}	$6.3 \cdot 10^{-7}$ µM^{-1} s^{-1}	e
HS^- oxidation	k_{HS^-}	$5.1 \cdot 10^{-9}$ µM^{-1} s^{-1}	g
Fe^{2+} oxidation	$k_{Fe^{2+}}$	$7.5 \cdot 10^{-5}$ µM^{-1} s^{-1}	h
FeS precipitation	k_{FeS}	$1.9 \cdot 10^{-12}$ µM^{-1} s^{-1}	g
Half-sat. constant aerobic respiration	K_{m,O_2}	8 µM	g
Half-sat. constant DNF	K_{m,NO_x}	12 µM	g
Half-sat. constant $Fe(OH)_3$ reduction	$K_{m,Fe(OH)_3}$	$50 \cdot 10^3$ µM	h
Half-sat. constant SO_4^{2-} reduction	K_{m,SO_4}	0.85 mM	i
Half-sat. constant anammox and NH_4^+ oxidation	K_{m,NH_4}	10 µM	e

Continued on next page

Table 4.3 – continued from previous page

Description	Symbol	Value	Source
Dissociation constant FeS	K_{FeS}	1.12 mM	g
Fractionation factors			
Denitrification (NO_2^-)	$\alpha_{\mathrm{NO_2,DNF}}$	0.985	j
Denitrification (NO_3^-)	$\alpha_{\mathrm{NO_3,DNF}}$	0.979	j
Nitrification (NH_4^+)	$\alpha_{\mathrm{NH_4,ox}}$	0.984	e
Nitrification (NO_2^-)	$\alpha_{\mathrm{NO_2,ox}}$	1.013	j
Anammox (NO_2^-)	$\alpha_{\mathrm{NO_2,amx}}$	0.982	k
Anammox (NH_4^+)	$\alpha_{\mathrm{NH_4,amx}}$	0.984	e

Sources: (a) Brandes and Devol (1997), (b) Lønborg and Søndergaard (2009), (c) Volkenborn et al. (2010), (d) Reitze and Schöttler (1989), (e) fitted to reproduce measurements of Brandes and Devol (1997), (f) Dornhoffer et al. (2015), (g) Wang and Van Cappellen (1996), (h) Van Cappellen and Wang (1995), (i) Pallud and Van Cappellen (2006), (j) from data compiled by Casciotti (2009), (k) Brunner et al. (2013).

The second method uses the equation derived by Fennel et al. 2009, which estimates the benthic N_2 production rate ($F_{\mathrm{N_2}}$, mmol N m^{-2} d^{-1}) as a function of SCOC:

$$F_{\mathrm{N_2}} = 0.086111 \cdot \mathrm{SCOC} + 0.17624 \tag{4.13}$$

Results for simulations with particulate-to-dissolved organic matter conversion ($F_{\mathrm{DOM,prod}}$, Table 4.3) and pumping (Q) rates, which match the relationship between SCOC and $F_{\mathrm{N_2}}$ given in Eq. 4.13 were then identified. Since the sediment N_2 production in the model is to a large extent dependent on the NO_3^- introduced through bioirrigation (see results), this allows identification of the corresponding bioirrigation intensity.

4.3 Results

The distribution of solutes and reaction rates in the baseline simulation are shown in Fig. 4.1. O_2 was restricted to a plume surrounding the feeding pocket (Fig. 4.1a), limiting the volume where aerobic remineralization and nitrification (Fig. 4.1d) can take place. The zone of N_2 production through DNF and anammox (Fig. 4.1e), which are inhibited by O_2 and limited by NO_x availability (Fig. 4.1b), encapsulated this oxygenated zone. At a burrowing depth of 15 cm nearly all NO_x produced in situ or pumped into the sediment was ultimately reduced to N_2, while at a shallower burrowing depth of 5 cm the burrow-associated NO_x plume extended across the sediment-water interface (see contour lines in Fig. 4.1b), enabling a significant fraction of the injected NO_x to escape reduction to N_2. Modeled NH_4^+ concentrations were suppressed at the depth of the feeding pocket due to high consumption by nitrification and anammox (Figs. 4.1c,f). The NO_3^- profile peaked at the feeding pocket

depth, while the NO_2^- concentrations remained below 4 µM throughout the sediment domain. The lateral heterogeneity in the sediment allows the highest rates of aerobic and anaerobic processes to occur at the same depth (e.g. anammox and nitrite oxidation, Fig. 4.1f).

The benthic exchange fluxes measured by Brandes and Devol (1997) were reproduced in the baseline simulation. The modeled benthic O_2 uptake of 4.4 mmol m^{-2} d^{-1} and the magnitude and isotopic composition of the NH_4^+ flux to the overlying water (Fig. 4.2a) matched their data. Bottom water $NO_3^-$with a measured $\delta^{15}N$ of 7.3‰ was pumped into the sediment and was reduced to NO_2^-. A small fraction of relatively light NO_2^- was able to escape further reduction and fluxed out to the overlying water (Fig. 4.2a). The resultant net NO_x flux into the sediment of 7.5‰, combining an influx of bottom water nitrate of 7.3‰ with a nitrite efflux of 3.3‰, was slightly heavier than the bottom water NO_3^- and matched with the values reported in Brandes and Devol (1997). Denitrification of NO_2^- and anammox accounted for 63% and 37% of the benthic N_2 production, respectively. The N_2 production also matched that of Brandes and Devol (1997), but had a $\delta^{15}N$ of 5.2‰ compared to the reported 1 ± 4‰. Applying Eq. 4.4 the ϵ_{sed} value was -2.4‰.

Sensitivity analyses were performed by changing the pumping rate (Fig. 4.3a), burrow density and burrow depth (Fig. 4.3b), the reactivity of DOM (Fig. 4.3c), the bottom water O_2 and NO_3^- concentrations (Fig. 4.3d.e), and the POM to DOM conversion rate (Fig. 4.3f). Each panel shows the N_2 production rates (top) and the ϵ_{sed} values (bottom), which together determine the effect of benthic N_2 production on the isotopic composition of dissolved inorganic N in the overlying water. A lower pumping rate decreased the N_2 production rate and led to a higher expression of the N isotope effect of anammox and nitrification (Fig. 4.3a). Conversely, higher pumping rates enhanced the N_2 production and led to more fractionation due to DNF (Fig. 4.3a). Changing the domain radius, reflecting a different organism density, showed a similar pattern. Fractionation due to nitrification and anammox was more strongly expressed when the bioirrigation intensity was decreased (larger domain radius, Fig. 4.3b), while the fractionation induced by DNF was stronger when the bioirrigation intensity was increased (smaller domain radius). A shallower burrow depth of 5 cm reduced the N_2 production rate and increased the N isotope fractionation of nitrification, anammox, and DNF (compare left and right group in Fig. 4.3b).

Lowering the reactivity of DOM by two orders of magnitude (to $k_{DOM} = 2 \cdot 10^{-7}$ s^{-1}, Fig. 4.3c) led to a strong degree of N isotope fractionation. Fractionation during NH_4^+ oxidation made ϵ_{sed} less negative and thus had an apparent inverse N isotope effect. However, the effect on the isotopic composition of NO_x in the overlying water was small (Fig. 4.2b), since the N_2 production was very low (Fig. 4.3c, top panel). Lowering the reactivity of DOM by only one order of magnitude (to $k_{DOM} = 2 \cdot 10^{-6}$ s^{-1}, Fig. 4.3c), led to a slightly lower N_2 production rate than in the baseline simulation. Fractionation during DNF had a large impact on ϵ_{sed} and led to heavier NO_x in the overlying water. A higher DOM reactivity ($k_{DOM} = 2 * 10^{-5} s^{-1}$ and $k_{DOM} = 2 * *10^{-4} s^{-1}$, Fig. 4.3c) had little effect on the N_2 production rate, but led

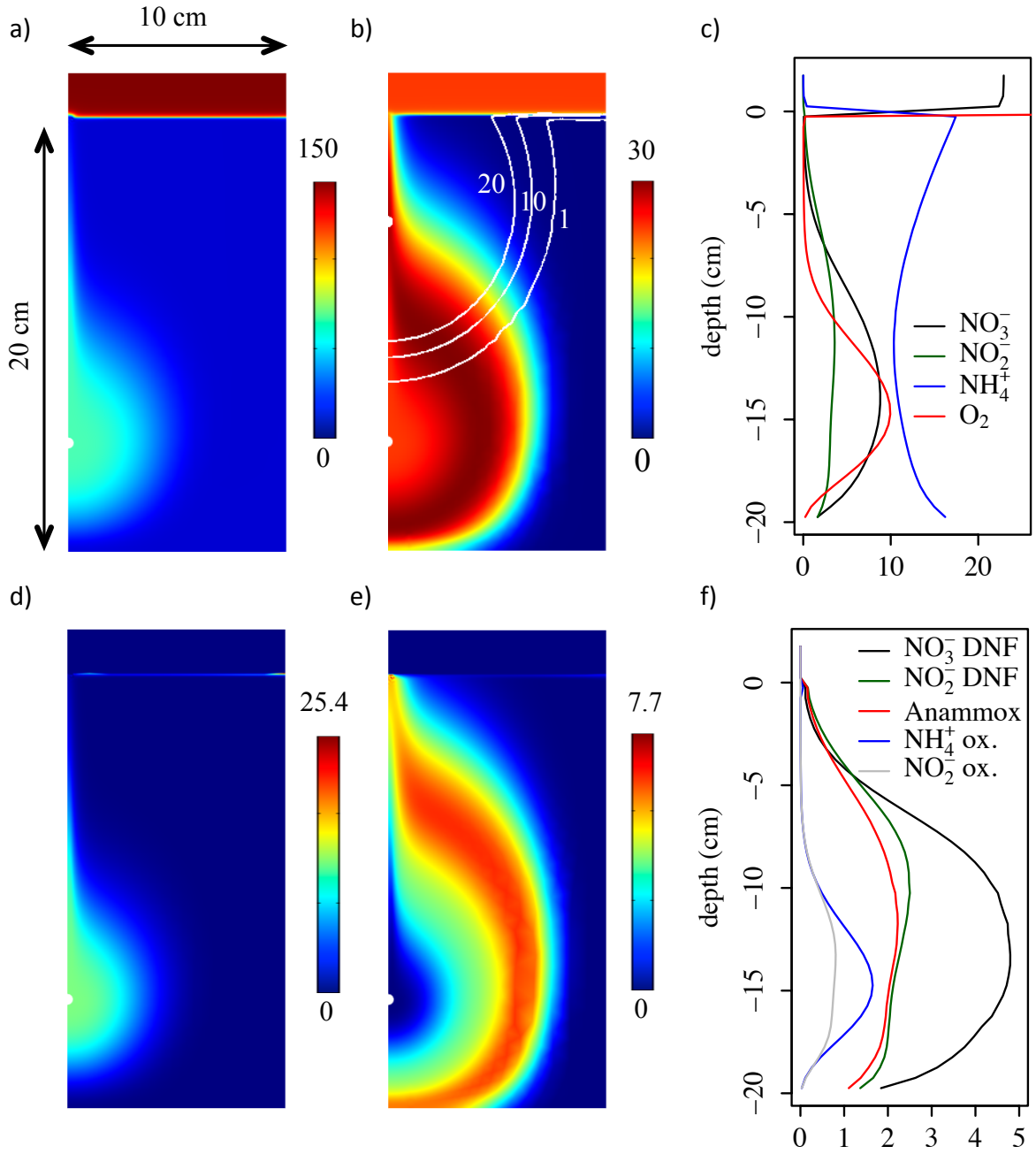

Figure 4.1: Steady-state concentration fields and reaction rates from the baseline simulation. The contours in panel b show the NOx concentrations of the simulation with a feeding pocket at 5 cm depth. The concentrations and rates in panels c and f, respectively, are horizontally averaged over the domain.

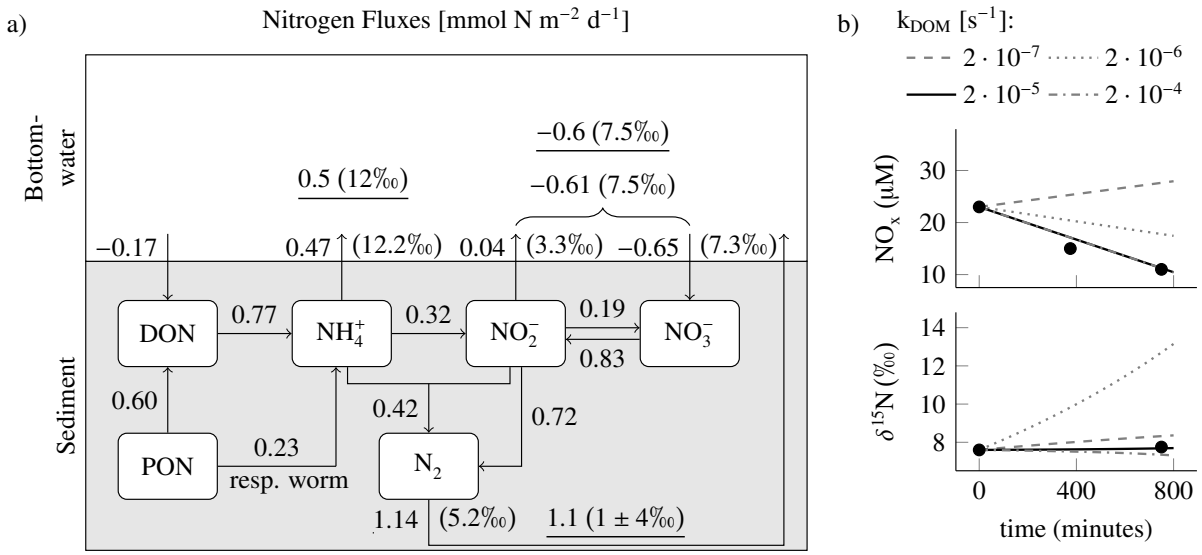

Figure 4.2: Nitrogen cycling in the baseline simulation, (a) N fluxes and their isotopic composition: measurements of Brandes and Devol (1997) are underlined; 'resp. worm' refers to NH_4^+ produced during respiration by the worm, (b) NO_x concentration and associated isotope signature in a benthic chamber reflecting the conditions of Brandes and Devol (1997). Lines are calculated from fluxes of the baseline (solid) and sensitivity analysis of DOM reactivity (dashed), while filled circles represent the observations of Brandes and Devol (1997).

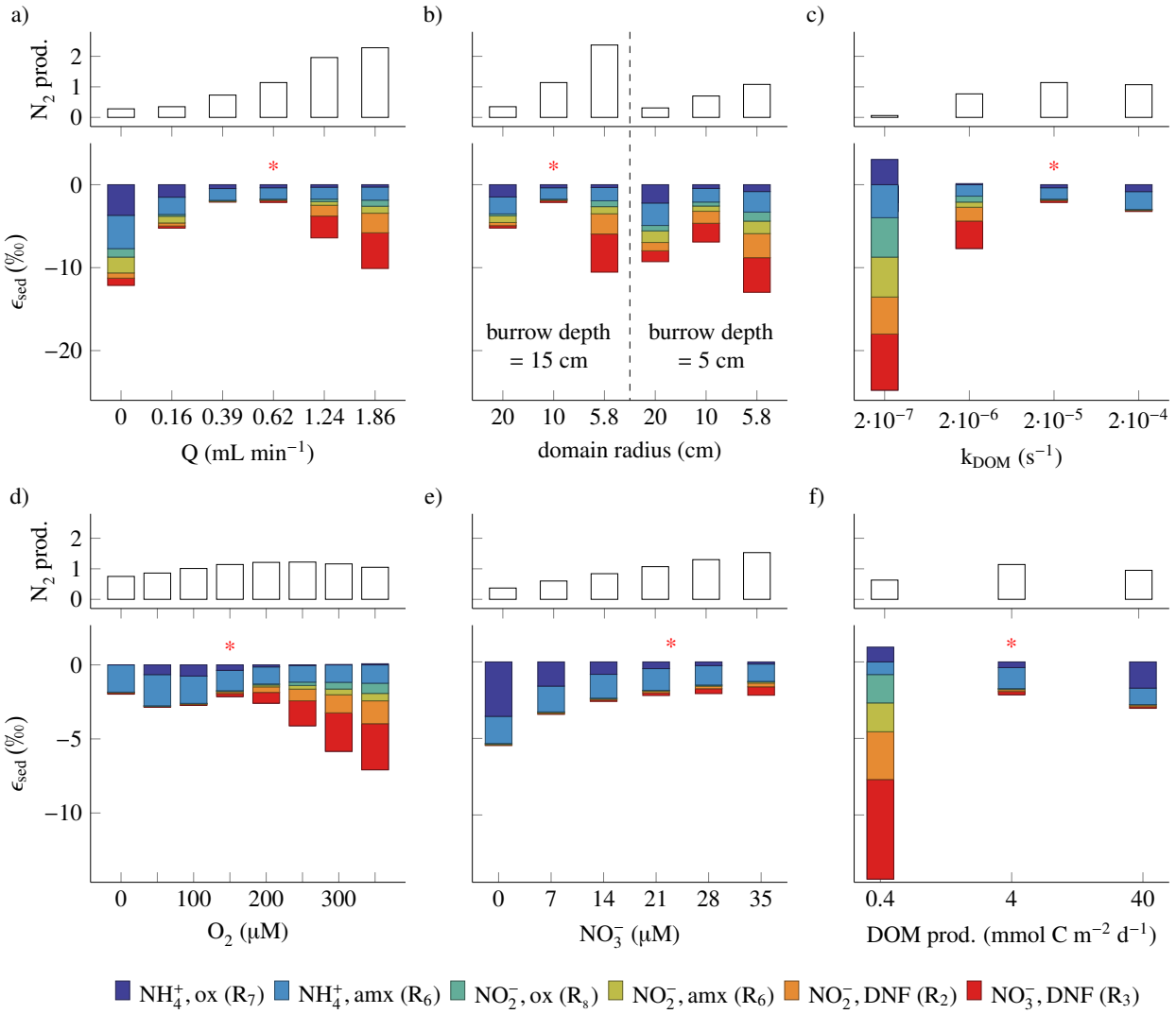

Figure 4.3: Sensitivity of the N_2 production rate (mmol m^{-2} d^{-1}) and benthic N isotope effect towards (a) the pumping rate, (b) the domain radius with a burrow depth of 15 cm and 5 cm, (c) the reactivity of dissolved organic matter, (d) the bottom water O_2 concentration, (e) the bottom water NO_3^- concentration, and (f) the in situ dissolved organic matter production rate. Stacked bars show the contribution of individual processes (see also Eq. 4.11). Asterisks indicate the values used in the baseline simulation.

to less N isotope fractionation during DNF and slightly more fractionation during NH_4^+ oxidation and anammox. The isotopic composition of the benthic NO_x flux was similar to that of NO_3^- in the overlying water and had therefore a negligible effect on the $\delta^{15}N$ of NO_x in the overlying water (Fig. 4.2b). Changing the rate of DOM to POM conversion had a moderate effect on the benthic N_2 production rate (Fig. 4.3f) and the contribution of individual processes on ϵ_{sed} values showed similar trends as changing the DOM reactivity.

The bottom water O_2 concentration had a moderate effect on the N_2 production rate, with maximum areal rates at 250 µM (Fig. 4.3d). At higher O_2 concentrations, fractionation during DNF led to substantially more negative ϵ_{sed} values. The highest contribution of NH_4^+ oxidation and anammox to the isotope effect of benthic N_2 production was at relatively low O_2 concentrations of 50 - 100 µM. The bottom water NO_3^- concentrations had a substantial effect on the benthic N_2 production rates (Fig. 4.3e). The N isotope effect of NH_4^+ oxidation and anammox was stronger at low NO_3^- concentrations, while fractionation during DNF was stronger at high NO_3^- concentrations.

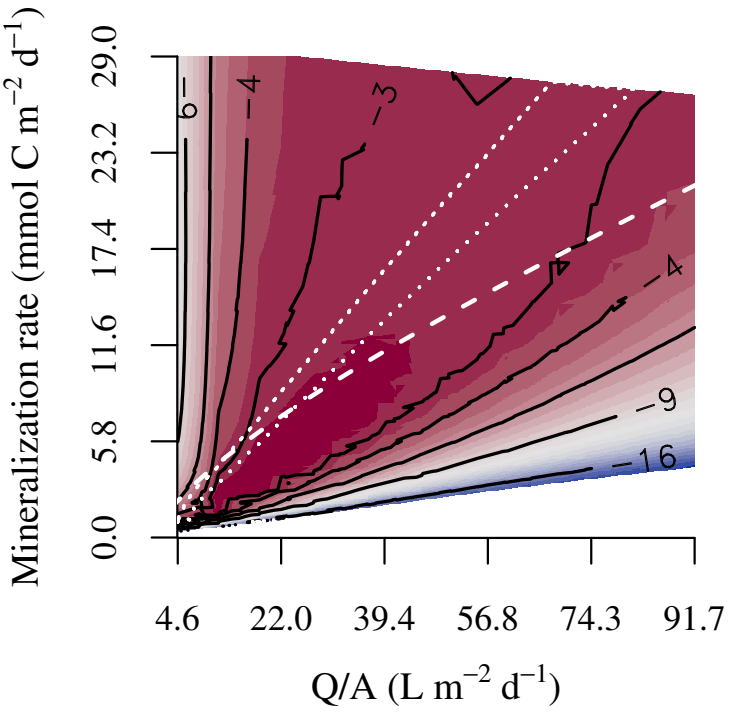

Figure 4.4: The combined effect of the mineralization rate and bioirrigation intensity on the benthic N isotope effect (ϵ_{sed}, solid contour lines). The dashed line corresponds to Eq (4.12). The dotted contour delineates the region in which the model computed N_2 flux is within ±10% of Eq. (4.13).

Changing the mineralization rate and bioirrigation intensity simultaneously gives insight in the expression of the benthic N isotope effect in different environments. The ϵ_{sed} values

were most negative when either the irrigation intensity was high and the mineralization rate low or, conversely, the irrigation intensity low and the mineralization rate high (Fig. 4.4). Between these extremes, there was a relatively large region with ϵ_{sed} values between -2.1 and -4‰. The two lines in Fig. 4.4 that tentatively indicate which mineralization rates may be most typical for different bioirrigation intensities (see methods section) were similar for low bioirrigation intensities, but differed more substantially at higher values. Nonetheless, both ϵ_{sed} values corresponding to these estimates of commonly encountered combinations of irrigation intensities and mineralization rates were generally less negative than -3.5‰. A similar analysis conducted with a burrow depth of 5 cm (not shown) exhibited a similar pattern, but exhibited about 2 - 3‰ more negative ϵ_{sed} values.

4.4 Discussion

4.4.1 Benthic nitrogen processing and isotope fractionation

Macrofauna can pump bottom water to depths in the sediment that without bioirrigation would be anoxic. The simulated redox zonation with an oxic plume surrounding the feeding pocket and anoxic conditions in the remainder of the sediment (Fig. 4.1a) are in line with studies on large burrowing macrofauna (Na et al. 2008; Volkenborn et al. 2010). The modeled solute profiles showed pronounced accumulation of NO_3^- and depletion of NH_4^+ at the feeding pocket depth (Fig. 4.1c), which is qualitatively consistent with profiles measured at sites with large burrowing macrofauna (Grundmanis and Murray 1977; Hüttel 1990; Volkenborn et al. 2007). At the Puget Sound site studied by Brandes and Devol (1995, 1997), measured O_2 and NO_3^- concentrations approached zero in the uppermost centimeter of sediment, similar to the computed horizontally averaged concentration profiles (Fig. 4.1c), but no measurements were reported at greater depth in the sediment, where infauna present (Lie 1968; Brandes and Devol 1997; Nichols 2003) may have affected O_2 and NO_3^- concentrations. Sediment permeability and porosity constrains the environment in which bioirrigation can be a dominant transport process (Hüttel et al. 2003). However, since model simulations use an imposed pumping rate, the computed flow field is only impacted by spatial variations in permeability. The ten-fold higher permeability in the feeding funnel than in the bulk sediment leads to a slightly higher expulsion of porewater through this conduit. However, the overall effect on the benthic N exchange fluxes and expression of the N isotope effect was small ($\Delta\epsilon = -0.1$‰). Similarly, variations in porosity have only a minor impact on fluxes and fractionation (not shown).

For a given organism density (reflected in the domain size), the pumping rate controlled the benthic exchange fluxes of NO_x and O_2, since the injected NO_x and O_2 were in most settings quantitatively consumed. For instance, in the baseline simulation all O_2 and nearly all NO_x from the plume were consumed before they could reach the sediment-water interface

(Fig. 4.1b). Areal pumping rates, which are a combination of the density of burrowing organisms and the individual pumping rates, were the same in the simulations with a domain radius r = 10 cm and Q = 0.16, 0.62, and 1.86 mL min^{-1} (Fig. 4.3a) and those with Q = 0.62 mL min^{-1} and r = 20, 10, and 5.8 cm (Fig. 4.3b, burrow depth = 15 cm), respectively. The corresponding bar plots are nearly identical. This indicates that the areal bioirrigation intensity controls the magnitude and isotopic composition of the N fluxes.

The model simulations reproduced the benthic exchange fluxes reported by Brandes and Devol (1997) except that the isotopic composition of the in situ produced N_2 gas differed by 4‰ from the average measured value reported by Brandes and Devol (1997). Multiple factors could have played a role in causing this discrepancy. Firstly, determining N_2 fluxes is challenging due to the high background concentrations of N_2 in seawater (Hamersley and Howes 2004), and uncertainties in isotopic signatures of fluxes can be substantial (±4‰ in Brandes and Devol 1997). Secondly, sediment N sources and sinks may be out of balance, while steady-state conditions were assumed in the model, which can lead to differences in modeled and observed benthic N fluxes and isotope effects. Finally, the model did not account for dissimilatory nitrate reduction to ammonium, connecting the oxidized and reduced dissolved inorganic N species, or for NH_4^+ assimilation, which could affect the isotopic composition of benthic DON exchange fluxes. Underestimating the efflux of heavy DON would result in an isotopically too heavy N_2 efflux in the model. Alkhatib et al. (2012) have argued that DON fluxes can play an important role in communicating benthic N isotope effects to the overlying water. However, this contribution remains poorly constrained as neither Alkhatib et al. (2012) nor Brandes and Devol (1997) reported the $\delta^{15}N$ and flux of DON separately from NH_4^+.

In the sensitivity analysis the expression of the N isotope effect of individual processes (ϵ_i, Fig. 4.3) is largely controlled by the benthic redox conditions. More oxidizing conditions correspond to higher injection rates of oxic bottom water into the sediment (Q, Fig. 4.3a), higher organism densities (i.e. smaller domain radii, Fig. 4.3b), DOM with less reducing power (smaller k_{DOM}, Fig. 4.3c), more O_2 and NO_3^- in the bottom water (Figs. 4.3d,e), the production of less reducing DOM (Fig. 4.3f), while the opposite trends correspond to more reducing conditions. Under oxidizing conditions discrimination against heavy NO_3^- during DNF is more strongly expressed, whereas under reducing conditions discrimination against heavy NH_4^+ during NH_4^+ oxidation and anammox is more pronounced. This reflects that the expression of N isotope fractionation at the cell level is dependent on the fraction of the benthic reactant pool that is being consumed (Mariotti et al. 1981; Lehmann et al. 2004). Under oxidizing conditions the sediment resembles a closed system for NH_4^+, consuming a larger fraction of the benthic NH_4^+ pool, and preventing the efflux of heavy NH_4^+ caused by fractionation during NH_4^+ oxidation and anammox to the overlying water. Meanwhile, the sediment resembles a more open system towards NO_3^- and simulations that showed stronger expression of the fractionation during NO_3^- reduction ($\epsilon_{NO_3,DNF}$) had NO_x

plumes that extended from the feeding pocket to the sediment-water interface (e.g. Figs. 4.1b,4.3b). The preferential consumption of light NO_x in the sediment will then lead to a flux of NO_x enriched in ^{15}N to the overlying water. Conversely, under more reducing conditions, the system becomes more open towards NH_4^+ as less O_2 is available to oxidize it, while it becomes more closed towards NO_3^-, minimizing the expression of the N isotope effect of DNF.

The expression of a benthic N isotope effect depends on the fractionation occurring at the cell level, as well as the coupling between different reactions that compete for substrates. The latter can lead to an apparent inverse N isotope effect on the overall benthic N_2 production, despite a fractionation factor $\alpha < 1$, as seen for NH_4^+ oxidation at low mineralization rates (Figs. 4.3c,f). Since fractionation during this reaction leads to heavier NH_4^+ and lighter NO_2^-, the inverse apparent N isotope effect (production of isotopically heavy N_2) can only occur when a large amount of NH_4^+ is converted to N_2 and a part of the produced NO_x escapes to the overlying water. This depends on the prevalent redox conditions, and requires anammox to be the dominant N_2 production pathway, propagating the heavy residual NH_4^+ signature into N_2. When DNF dominates N_2 production (as is the case at higher mineralization rates in Figs. 4.3c,f), the δ_{N_2} reflects largely the isotopic signature of the NO_2^- and a "normal" negative apparent N isotope effect of NH_4^+ oxidation is observed.

The impact of the benthic N isotope effect on the isotopic composition of fixed N in the overlying water is dependent on both ϵ_{sed} and the N_2 production rate. Thus, there is a stronger impact at high irrigation rates compared to conditions with low Q, as N_2 production increases with the higher input of NO_3^- (Fig. 4.3a). Similarly, there is a very strong N isotope effect at the lowest DOM reactivity, but the impact on fixed N in the overlying water is negligible due to the extremely low N_2 production rate (Fig. 4.3c). In Fig. 4.3e the N isotope effect of NH_4^+ oxidation and anammox is stronger at lower NO_3^- bottom water concentrations. This is because at the same pumping rate less NO_3^- is injected, so that the N_2 production and its isotopic signature are more dependent on fractionation during NH_4^+ oxidation. At higher NO_3^- concentrations in the bottom water, the supply of NO_3^- to the sediment via bioirrigation increases. This stimulates N_2 production and lowers the relative contribution of NH_4^+ oxidation to the benthic nitrogen isotope effect (Fig. 4.3e).

4.4.2 The effect of solute transport on benthic nitrogen isotope fractionation

In bioirrigated sediment, N isotope cycling is dependent on the bioirrigation intensity and the burrowing depth (Figs. 4.3a,b). For shallow burrows, some of the injected NO_x is flushed out the sediment before it can be reduced, which significantly enhances the expression of the N isotope effect of DNF. A shallow burrow depth also increases the expression of the N isotope effect of nitrification and anammox (Fig. 4.3b). Rates of these processes are

highest within and around the oxic plume (Figs. 4.1d,e). When the plume extends across the sediment-water interface a larger fraction of NH_4^+ produced in the sediment by organic matter mineralization escapes to the overlying water (Fig. 4.3b) and allows for expression of the N isotope effect of benthic N_2 production. NO_x injected at greater depth is less likely to escape to the overlying water, since the oxic plume surrounding the burrow and the sediment-water interface are than separated by a larger reducing zone, where DNF and anammox take place. When the injected NO_x is quantitatively consumed DNF does not induce fractionation.

Our model results provide context for the interpretation of field observations. Lehmann et al. (2004) measured benthic N fluxes with incubation experiments in shelf sediments of the Santa Monica Bay, where bioirrigation plays an important role. They observed that the isotopic composition of NO_3^- did not change over time, which suggests that, similar to our baseline scenario, the NO_3^- was quantitatively consumed. In contrast, Dale et al. (2014) reported a strong benthic N isotope effect in hypoxic Mauritanian margin sediments. Their ϵ_{sed} value was $-13‰$ and appeared to be mostly communicated to the overlying water through NO_x exchange fluxes. On photographs of the sediments burrow openings and other signs of macrofaunal activity were visible, yet the porewater profiles did not exhibit subsurface peaks of NO_3^-, which makes the importance of bioirrigation unclear. Granger et al. (2008) estimated an ϵ_{sed} value of -6 to $-8‰$ based on measured light NO_3^- and heavy reduced N in bottom water of the Bering Sea shelf, and argued that partial nitrification of the benthic NH_4^+ pool drove the N isotope effect of benthic N_2 production. The benthic infauna was not identified in their study, but burrows are prevalent in Bering Sea shelf sediments (Davenport et al. 2012) exposed to large fluxes of POM (Baumann et al. 2013). Large NH_4^+ effluxes are common in bioirrigated sediments (Na et al. 2008; Stief 2013, Lehmann et al. 2004) due to enhanced mineralization rates (Aller and Aller 1998; Kristensen 2001) and the ejection of anoxic porewater (Volkenborn et al. 2010). Under these conditions, the N isotope effect of anammox and coupled nitrification-N_2 production can be communicated to the overlying water through effluxes of isotopically heavy NH_4^+, which is consistent with our analysis (see for example the effect of higher mineralization rates in Figs. 4.3c,f).

The effect of bioirrigation can also be compared and contrasted with other transport regimes. Advective flow caused by pressure gradients, which may be the result of bottom currents over rippled sediment surfaces or the motion of waves, can lead to high N_2 production in sediments (Boudreau et al. 2001; Kessler et al. 2012). Based on combined water-column experiments and modeling Kessler et al. (2014) estimated that benthic N_2 production in these sediments can lead to NO_3^- fluxing out of the sediment that is enriched by $3 \pm 1‰$. Nitrification did not occur in their experiment, but their model indicated that including nitrification would have a small effect. DNF under advective flow regimes is mainly driven by NO_3^- from the overlying water, while coupling between nitrification and DNF is low (Kessler et al. 2012). This is in stark contrast to sediments with deeper bioirrigation, where

the coupling between nitrification and N_2 production is strong as all the NO_x produced in the oxic plume surrounding the burrow is ultimately reduced to N_2.

When the transport regime is dominated by diffusion, NO_x fluxing into the sediment will be quantitatively consumed. In such a setting, a benthic N isotopic effect can still occur if the isotopic composition of the NO_x fluxing into the sediment differs from that of bottom water NO_x. Models have indicated that the preferential consumption of light NO_x in the sediment leads to a steeper gradient of $^{14}NO_x$ than $^{15}NO_x$, which then results into a net flux of light NO_x into the sediment and consequently the in situ production of light N_2 (Bender 1990; Brandes and Devol 1997). However, early studies showed that the isotopic composition of NO_x in the overlying water did not change during incubation experiments, which could suggest that N isotope fractionation in the sediment was negligible (Brandes and Devol 2002; Lehmann et al. 2007). It is also possible that the production of light NO_x during nitrification can mask the preferential use of isotopically light NO_x during DNF (Lehmann et al. 2007). This was observed in the simulation with bioirrigation turned off ($Q = 0$, Fig. 4.3a) where ϵ_{sed} was -12.6‰, while the sediment NO_x efflux was enriched by only 1.7‰. The N isotope effect is then communicated to the overlying water primarily through the efflux of heavy NH_4^+. Qualitatively, this is in agreement with a benthic N isotope effect of up to -7.2‰ modeled by Lehmann et al. (2007), who accounted for aerobic respiration, denitrification and nitrification only. It is also consistent with work by Dähnke and Thamdrup (2013), who showed experimentally that apparent N isotope fractionation during benthic DNF can occur in a setting where transport is dominated by diffusion.

4.4.3 Benthic nitrogen isotope effects under commonly encountered environmental conditions

Our simulations indicate that the N isotope effect will be strongest in surficial sediments that have either strongly reducing or oxidizing conditions (Figs. 4.3a,4.4). Redox conditions strongly depend on the intensity of bioirrigation and the reaction rates consuming O_2, reflected in mineralization rate. However, settings with high bioirrigation intensity and low mineralization rates or vice versa are relatively rare. These two competing factors commonly correlate, since OM rich settings with high rates of mineralization can support a large number of benthic infauna (Künitzer et al. 1992), which enhance the transport of oxidants into the sediment. Conversely, in areas where POM is scarce the bioirrigation intensity may be lower. By using the relationships between the bioirrigation intensity and benthic mineralization rates (see Eqns. 4.12, 4.13) the model simulations predict that ϵ_{sed} values in bioirrigated sediment are commonly close to -3‰ (Fig. 4.4). However, there are a number of uncertainties associated with this estimate. Firstly, our simulations of shallower burrows indicate a larger benthic N isotope effect (Fig. 4.3b). However, smaller organisms are likely to pump less, and enhanced flow may also lead to conditions more comparable to the advec-

tive setting studied by Kessler et al. (2014). Secondly, N-cycling processes not considered in the model may also impact fractionation. Thirdly, comprehensive data sets on benthic N isotope cycling suitable for model parameterization are scarce, offering limited constraints on the model parameterization. For example, it is clear that fractionation factors in the field may differ from laboratory conditions, yet it is not well understood what causes the discrepancies between different studies (Kritee et al. 2012).

Bioirrigation is important in shallow marine environments where a significant part of the global N_2 production takes places and therefore must have a large imprint on the global average N isotope effect of benthic N_2 production (ϵ_{glob}). Our estimate of -3‰ being common for bioirrigated sediments is akin to previous estimates of ϵ_{glob}. Lehmann et al. (2007) estimated -4‰, which is remarkably similar given the fact that they did not account for advective transport and considered a different set of early diagenetic reactions. Kessler et al. (2014) also found an N isotope effect of ~ -3‰ for coastal sediment with transport dominated by wave-induced advection. Global circulation models coupled to N cycle models have tried to reproduce the measured NO_3^- concentrations and isotopic composition in the ocean to spatially resolve pelagic and benthic N_2 production rates. Using this approach, Somes et al. (2013) found best fits of the ocean fixed δ^{15}N with ϵ_{glob} values between -2 and -4‰. Such benthic fractionation has a significant impact on estimates of benthic vs. pelagic N_2 production. Assuming steady-state and considering only nitrogen fixation as source and water-column and benthic N_2 production as sinks, the fraction fbenthic of benthic N_2 production of the total N_2 production can be estimated as

$$f_{\text{benthic}} \approx \frac{\epsilon_{\text{fix}} - \delta^{15}\text{N-N}_{\text{fix,avg}} - \epsilon_{\text{wc}}}{\epsilon_{\text{glob}} - \epsilon_{\text{wc}}} \tag{4.14}$$

where ϵ_{fix} is the N isotope effect of N fixation (~ -1‰), $\delta^{15}\text{N-N}_{\text{fix,avg}}$ is the average isotopic composition of ocean fixed N (~ 5‰), and ϵ_{wc} is the N isotope effect of water-column N2 production. Kritee et al. (2012), whose experiments indicated that turbulence and thermodynamically lower N isotope fractionation at the cell level, argued that ϵ_{wc} might fall in the range of -10 to -15‰, which is substantially different from earlier estimates such as the -20‰ estimated by Brandes and Devol (2002). Furthermore, less apparent fractionation can be expected in oxygen minimum zones if NO_3^- becomes locally heavier than the average ocean δ_{NO_3} (Deutsch et al. 2004). Using $\epsilon_{\text{wc}} = -12.5$‰ and $\epsilon_{\text{glob}} = -3$‰, leads to 68% of total marine N_2 production to taking place in the sediment. For water-column N_2 production of ~ 70 Tg N yr_{-1} (Bianchi et al. 2012), the benthic N_2 production rate would be 152 Tg N yr^{-1}. A ± 1‰ uncertainty in ϵ_{glob} corresponds to global benthic N_2 production rates between 114 and 228 Tg N yr^{-1}, which highlight the sensitivity of the ocean fixed δ^{15}N towards N isotope fractionation in sediments.

4.5 Conclusion

Redox conditions exert a major control on the N isotope effect of benthic N_2 production, since they determine the extent to which different benthic N pools are consumed within the sediment. Fractionation against heavy NH_4^+ during nitrification and anammox is enhanced under reducing conditions. Conversely, fractionation against heavy NO_x during DNF is enhanced under oxidizing conditions.

Solute transport processes together with the POM rain rate and the composition of the overlying water control the redox conditions in sediments. Bioirrigation can enhance mineralization (Aller and Aller 1998; Kristensen 2001), which promotes reducing conditions, but this effect is opposed by the injection of oxic water, which leads to more oxidizing conditions. The benthic N isotope effect is largest under either strongly reducing or strongly oxidizing conditions, which correspond to combinations of low bioirrigation intensities and high mineralization rates and vice versa, or when shallow pumping leads to substantial recirculation of injected dissolved N. However, under conditions most commonly encountered in bioirrigated sediments, the benthic N isotope effect is estimated to be close to $-3‰$, which is similar to previous estimates of the global N isotope effect (Lehmann et al. 2007; Somes et al. 2013). Such fractionation in sediments leads to substantially heavier NO_x in the ocean, tilting the balance towards benthic N_2 production, compared to estimates that ignore fractionation in marine sediments.

Chapter 5

The Evolution of Early Diagenetic Processes and Signatures During the Last Glacial-Interglacial Climate Transition at the Mozambique Margin[1]

[1]Rooze, J., Zindorf, M., C. Meile, C. März, G. Jouet, R. Newton, C. Brandily, and L. Pastor. Submitted to Geochimica et Cosmochimica Acta.

Abstract

The Mozambique continental margin experienced large variations in sedimentation rates, primarily due to sediment re-routing from the Zambezi river during the last glacial-Holocene transition. As changes in sediment accumulation and organic matter deposition impose a strong control on the formation of authigenic minerals in the sediments, the distribution of these minerals may reflect the regional paleoenvironmental and paleoclimatic evolution. Combining geochemical analyses of pore-waters and sediments with a reactive transport modeling approach, we reconstruct the depositional history and its effect on biogeochemical reaction processes in the sediment column at a site on the Mozambique margin over the past 27 kyr. Fitting the model parameters (influx of sedimentary organic matter and iron-(oxyhydr)oxides) to match the observed geochemical patterns, the reconstruction of past sulfate-methane transition zone depth and associated reaction rates shows that the sulfate-methane transition zone fluctuated in short time intervals between 15 and 10 kyr BP in response to sedimentation rate changes and organic matter deposition. Model results reveal an ongoing transition from high diagenetic reaction rates representative of near-shore depositional environments during the late glacial maximum, to a setting typical of offshore sediments with low reaction rates at the present day. Notably, the remnants of methane and dissolved iron pools produced in the past still shape the diagenetic processes at and below the sulfate-methane transition zone today. Since deglacial shelf-flooding and corresponding changes in sediment deposition occurred along continental margins worldwide, our analysis highlights the important role of non-steady state diagenetic processes in continental margin sediments and their relevance for paleoceanographic interpretation of sediment cores experiencing strong variations in sediment input.

5.1 Introduction

The siliciclastic and organic material delivered by rivers to the ocean accumulates at deposition centers near river mouths. The large influx of organic matter (OM) leads to fast biogeochemical turnover rates in these environments, marked by high sediment O_2 uptake (Glud 2008; Pastor et al. 2011, 2018). High sedimentation rates can increase burial rates of relatively reactive organic matter into the sediment (Müller and Suess 1979; Betts and Holland 1991; Canfield 1994), stimulating anaerobic turnover rates of OM. This includes the dissimilatory reduction of metal oxides (e.g., Aller et al. 1986; Taillefert et al. 2017; Pastor et al. 2018), sulfate reduction (Canfield 1989), and methanogenesis in deeper sediments (Martens and Klump 1984; Zhuang et al. 2018). Anaerobic oxidation of upward-diffusing methane (AOM) coupled to the reduction of downward-diffusing sulfate (SO_4^{2-}) creates a sulfate-methane transition zone (SMTZ; Martens and Berner 1977; Reeburgh 1980; Niewöhner et al. 1998; Boetius et al. 2000) where a number of biogeochemical transformations take place,

including the release of dissolved bicarbonate and hydrogen sulfide into the adjacent pore waters. The produced hydrogen sulfide (HS^-) can react with iron (oxyhydr)oxides or dissolved Fe_2^+, leading to the formation of iron sulfide minerals (Berner 1970, 1984). The resulting accumulation of such minerals (mainly in the form of pyrite, FeS_2) can serve as a proxy for the depth and migration of the SMTZ in sediment archives (März et al. 2008; Borowski et al. 2013; Roberts 2015). The position of the SMTZ in marine sediments tends to shift in response to changes in OM loading and sedimentation rates (e.g. Hensen et al. 2003; Kasten et al. 2003) as a higher methane (CH_4) flux can push the SMTZ upwards, while lower OM loadings and sedimentation rates can cause a deepening of the SMTZ (Contreras et al. 2013). Through their connection to the SMTZ iron sulfide minerals and their isotopic signature observed in sediment cores provide an important window into environmental conditions of the past. A major challenge, however, is to disentangle the impact of early diagenetic alterations from the climatic factors that are imprinted in the observed geochemical signal reminiscent of the past.

Non-steady state diagenesis in response to changes in paleoclimate and sedimentation patterns has been identified at several continental margins off major rivers like the Amazon or Rio de la Plata (Kasten et al. 1998; Riedinger et al. 2005) and at the Mozambique margin off the Zambezi (März et al. 2008; März et al. 2018).

In this study, we address the impact of early diagenetic alteration and quantify the effect of depositional history on the paleoclimatic signatures of a 33 m long sediment core taken off the shelf-break on the Mozambique continental slope. We fit an early diagenetic model that is subject to transient depositional forcing to the measured geochemical profiles. The model reconstructs the early diagenetic history of the last 27 kyr on the continental slope and evaluates the effect of OM input and sedimentation rates evoked by global paleoclimatic transitions on the depth of the SMTZ and the emerging signature of authigenic mineral accumulations.

5.2 Methods

5.2.1 Site description and sediment drilling

Site MOZ4-CS17 was cored on the Mozambique margin off the shelf-break $\sim$ 85 km off the Zambezi river mouth. The site is situated in the center of sediment deposition delivered by the Zambezi during Pleistocene sea-level lowstand but is not reached by the bulk of sediments deposited in modern times of high sea-levels.

The sediment core MOZ4-CS17 was collected with a Calypso piston corer aboard R/V Pourquoi pas? at 550 m water depth during the PAMELA-MOZ4 cruise (Fig. 5.1; Jouet and Deville 2015). The 33 m long core was cut into 1 m sections immediately after recovery on deck.

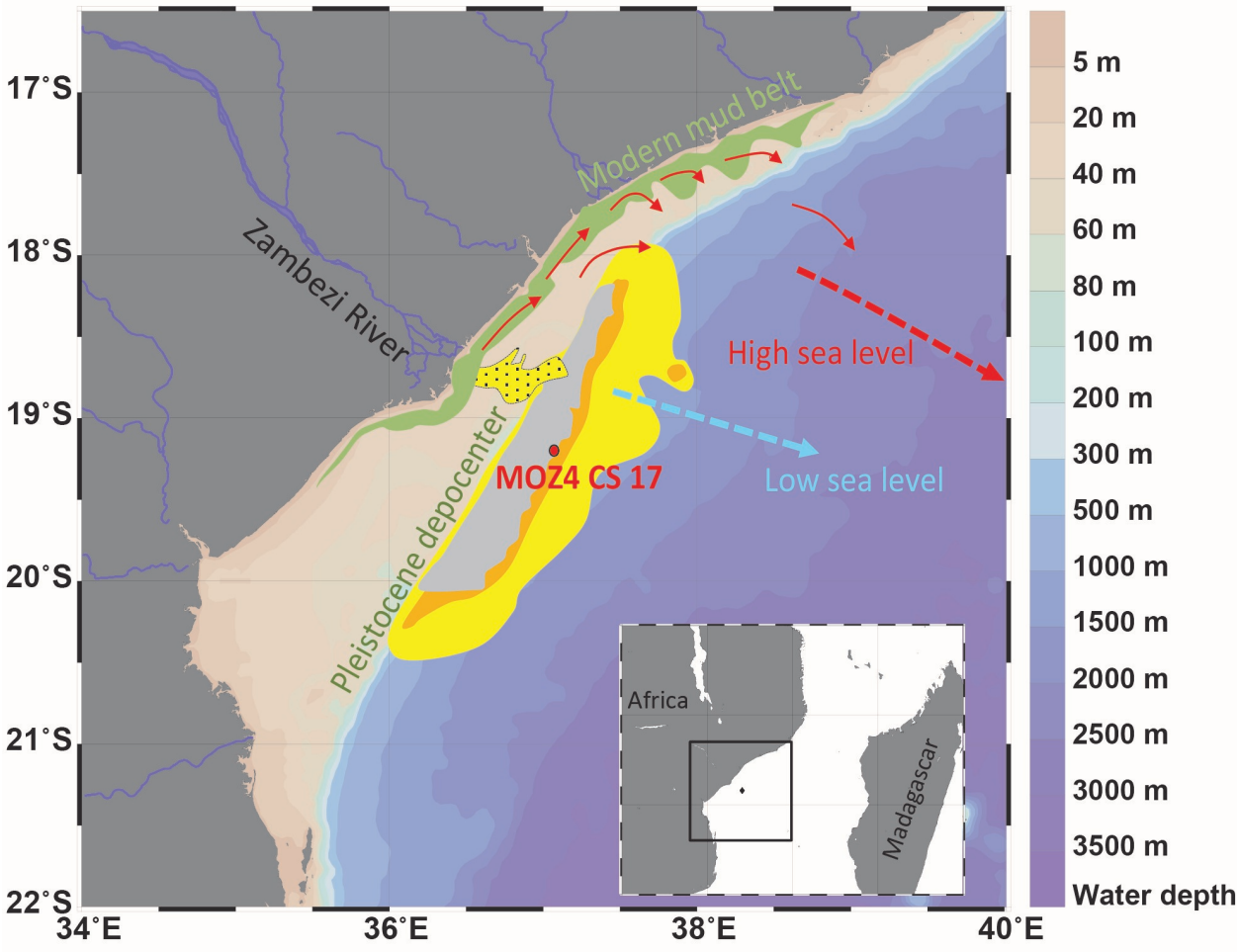

Figure 5.1: Map of the area of investigation. Red dot indicates position of Site CS17; arrows indicate direction of sediment transport during Pleistocene low sea-level (light blue); and during modern high sea-level (red) (Schulz et al. 2011); Thickness (increasing from yellow = 0 - 400 m to orange = 400 - 800 m to gray > 800 m shaded areas) of Pleistocene lowstand sediment deposition center centers inferred from the seismic investigations (Walford et al., 2005); modern sediment deposition (green mud-belt interpreted by Lubbe et al. (2014)); Paleo-Zambezi incised valley (yellow dotted area; Walford et al. 2005). The 100 m isobath approximately indicates dry shelf area during Pleistocene sea-level lowstand $\sim$ 20 kyr BP (brown hues). Bathymetric map created with Ocean Data View (Schlitzer 2015)

5.2.2 Analytical geochemistry

Sampling

Immediately after core cutting, 3 cm^3 of sediment were collected at the bottom of each section using a pre-cut syringe. The samples were directly transferred into 20 mL glass vials with 5 mL 1M NaOH, sealed and stored head-down at 4 °C before measurement for CH_4 concentrations. The presence of H_2S was measured at the bottom of each section using a Unisense sulfide electrode mounted with a steel needle with a detection limit of 0.3 µM. Each core section was then transferred to a cold room (at 8 °C). Pore-waters were extracted with Rhizon soil moisture sampler devices (10 cm length) inserted directly into small holes drilled into the core liner (3 per core section) down to the zone where no water could be extracted anymore (around 17.5 m sediment depth). Sediment samples were taken in $\sim$ 1m resolution. Depths of all samples in the core liner were corrected using the CINEMA2 software (Woerther et al. 2012) which allows estimating sediment disturbances by monitoring the coring kinematics.

Porewater analyses

A porewater split was acidified (to 0.4% HNO_3) and stored in acid-washed polypropylene vials at 4 °C before analysis onshore.

CH_4 concentrations were measured by headspace gas chromatography with a PR2100 gas chromatograph equipped with a flame ionization detector (GC/FID Perichrom, France) connected to a headspace injector (dani HSS 86.50; Sarradin and Caprais 1996). Results in ppmV headspace gas were converted to mM values using sample volume and measured porosity. The RSD value for this method is 3% and the limit of quantification is 0.1 µM. The stable carbon isotopic ratio of methane (δ^{13}C-CH_4) was determined with a G2201-i CRDS analyzer from Picarro. Isotopic composition is given in permil (‰) in the standard delta notation relative to the Vienna Pee-Dee Belemnite (V-PDB) composition. The global analytical precision was 0.1 ‰ with 2 replications per sample. To calibrate the ($\delta^{13}CH_4$ measurements, four different isotopic standards were used (Isometric Instruments,Inc., product numbers L-iso1, B-iso1, T-iso1, and H-iso1 at respectively -66.5‰, -54.5‰, -38.3‰ and -23.9‰).

SO_4^{2-} was measured with an ion-exchange chromatograph Dionex ICS-5000 from Thermo Scientific®, equipped with an Ionpac AG 22-SC precolumn, an Ionpac AS22-SC column, and an electrical conductivity detector. The eluent was Na_2CO_3 (5 mM) / $NaHCO_3$ (1.75 mM). IAPSO standard seawater was used for calibration and as a certified reference. Detection limit was 0.2 mM.

Concentrations of dissolved Fe^{2+} were analyzed by high resolution inductively coupled plasma mass spectrometry (HR-ICP-MS Element XR, Thermo Scientific). The calibration was based on the standard addition method of known amounts of each element in the IAPSO

standard seawater to avoid matrix effect. Indium (2ppm) was added in the dilution solution of 2% HNO_3 to correct for instrument drift.

Solid phase characterization

Sediment samples were freeze-dried and homogenized with an agate mortar and pestle. For total organic carbon content (TOC), around 250 mg of samples were first acidified with successive additions of HCl 1N at 40 °C until complete carbonate dissolution and rinsed twice with milli-Q water to remove residual acid. After freeze-drying, TOC was determined using a LECO TruMac®CNS auto-analyzer while $\delta^{13}C$ of the sedimentary OM was determined using Combustion Module-Cavity Ring Down Spectroscopy (CM-CRDS - Picarro; Balslev-Clausen et al. 2013). For the latter, calibration was performed using International Atomic Energy Agency (IAEA) reference materials: calcite (NBS-18), sucrose (CH-6) and lithium carbonate (LSVEC). An acetalinide standard (Costech) was inserted every ten samples to correct for the drift, with a measured value of -33.50 ± 0.02‰ (6 replicates). Precision was typically within 0.03 ‰ for a triplicate.

Pyrite was quantified with a Bragg-Brentano (D8 Advance Bruker) X-ray Diffractometer equipped with a Cu X-ray tube and a scanning detector with a Cu-kb filter in Ni (Vantec, BRUKER model). Measurements were made in 0.01˚steps at an angle of 5 to 70˚. Each step lasted 1s and was performed at 40kV and 30mA. Pyrite was also extracted following the protocol by Canfield et al. (1986) for S isotope measurements. Approximately 0.5 g of dried sediment was boiled with 12 ml 50 % HCl under a flow of nitrogen gas to dissolve the experimentally defined acid volatile sulfur (AVS) fraction which consists of Fe-monosulfides (predominantly mackinawite) and greigite (Fe_2S_3). After AVS extraction, 6 ml $CrCl_2$ were added to the boiling mixture to dissolve pyrite (FeS_2). In both steps, the released H_2S was trapped with $AgNO_3$ and the precipitated Ag_2S was stoichiometrically converted into moles S and sulfur-bound Fe. Standard error of this method was within 10% for three samples analyzed in triplicates and an inhouse standard (WHIT; Alcott et al. 2020), however, the standard error exceeded 30% for a fourth sample with a very low pyrite content. Sulfur isotopes (^{32}S and ^{32}S) of pyrite were analyzed in the Ag_2S precipitates. Around 200 µg of Ag_2S were analyzed using an Elementar Pyrocube coupled to a GC Isoprime stable isotope ration mass spectrometer. Results are given in the standard delta notation as $\delta^{34}S$ relative to the Vienna Canyon Diablo Troilite (V-CDT) international reference material and each sample was measured in duplicate. Samples were calibrated to the V-CDT scale using a lab seawater sulfate standard (SWS-3) an interlab chalcopyrite standard (CP1) and the international standard IAEA-S-3 with assigned values of +20.3, −4.56, and −32.06‰ respectively. SWS-3 was calibrated against the international standards (assigned values in brackets) NBS-127 (+20.3‰), NBS-123 (+17.01‰), IAEA S-1 (−0.30‰) and IAEA S-3 (−32.06‰). Repeat analyses of a barium sulfate check standard produce a standard deviation of < 0.3‰.

Reactive iron, i.e., mainly poorly crystalline and crystalline Fe-(oxyhydr)oxides, was semi-quantitatively determined by dithionite extraction (Kostka and Luther III 1994;Anschutz et al. 2000), followed by ICP-AES analysis of the extraction solution using a Horiba Jobin Yvon®Ultima 2 spectrometer. A certified sediment reference material (MESS-4, NRC-CNRC) was used to check the repeatability of the extractions through time. The global variability of MESS-4 was around 5% (standard error).

Chronology and sedimentation rates

The chronology of the calypso piston core MOZ4-CS17 is based on 16 ^{14}C dates. Sediments were sampled at regular intervals along a continuous and non-reworked typical hemipelagic sequence composed of fine clayey-silt typical for deltaic margins. The in-situ depths below seafloor were used to estimate sedimentation rates.

Sediment was dated using Accelerator mass spectrometer (AMS) standard radiocarbon methods on marine mollusk shells and the bulk assemblage of planktonic foraminifera. Analyses were performed at the Beta Analytic Laboratory (Florida, USA) and all ^{14}C ages were calibrated using the MARINE13.14C calibration curve (Reimer et al. 2013). A local marine reservoir correction of mean $\Delta R = 158 \pm 42$ years (Reimer and Reimer 2001) inferred from radiocarbon measurements in prebomb known-age shells and corals from the tropical SW Indian Ocean (Southon et al. 2002) was applied.

Sediment ages were interpolated in order to build an accurate age model and calculate linear sedimentation rates (SR in cm yr^{-1}) using the age-depth modeling software CLAM 2.2 (Blaauw 2010, 2010; R statistical software environment).

5.2.3 Modeling

The model simulates early diagenetic processes over the past 27.4 kyr. The governing equation accounting for diffusion, burial, and reaction of solutes is

$$\phi \frac{\partial C_i}{\partial t} = \frac{\partial}{\partial z}\left[\phi\left(\frac{D_i}{\theta^2} + D_b\right)\frac{\partial C_i}{\partial z} - \phi\omega C_i\right] + \sum_k s_k^i R^k \tag{5.1}$$

and that of solids is

$$\phi_s \frac{\partial C_j}{\partial t} = \frac{\partial}{\partial z}\left[\phi_s D_b \frac{\partial C_i}{\partial z} - \phi_s \omega C_i\right] + \sum_k s_k^j R^k \tag{5.2}$$

whereby ϕ is the sediment porosity, $\phi_s = 1 - \phi$ is the solid volume fraction, C_i and C_j are the concentrations of dissolved and solid species, respectively, z is the depth in the sediment, θ is the tortuosity, D_b is the bioturbation coefficient, ω is the burial velocity, and s_k^i and s_k^i are the stoichiometric coefficients of the reaction rates R_k (Boudreau 1997). The burial velocity

changed with time, as determined by sediment dating. The ionic/molecular diffusion coefficients were corrected for in-situ pressure, temperature, and salinity conditions (Boudreau 1997; Soetaert et al. 2016). The bioturbation coefficient is described as an exponentially decaying function

$$D_b(z) = D_{b0} e^{\frac{z}{q}} \tag{5.3}$$

where D_{b0} and q are given in Table 5.1. The porosity is assumed to be constant over time and described as an exponentially decreasing function with depth

$$\phi(z) = \phi_\infty + (\phi_0 - \phi_\infty) e^{\frac{z}{\gamma}} \tag{5.4}$$

where ϕ_0 and ϕ_∞ are the porosities at the sediment-water interface and at depth, respectively, and γ is a fitted coefficient (Table 5.1). As we assume steady-state compaction, the porosity is not a function of time. Following Boudreau (1996), the tortuosity is defined as:

$$\theta^2 = 1 - 2\log(\phi) \tag{5.5}$$

The solids in the model include organic matter, Fe-(oxyhydr)oxides and pyrite. OM is available in three fractions, where OM^α is the most labile fraction, OM^β is less reactive, and OM^γ has the lowest reactivity and is only reacts with O_2. Fe-(oxyhydr)oxides are represented by Fe_2O_3 and are divided into two fractions: $Fe_2O_3^\alpha$ can react with organic matter by organoclastic Fe reduction, while $Fe_2O_3^\beta$ does not react with organic matter. Both fractions react with HS^-. Authigenic Fe sulfides are represented by pyrite (FeS_2). The model also includes dissolved O_2, SO_4^{2-}, CH_4, HS^- and Fe^{2+}. This set of state variables was selected to represent the main aspects of C, O, Fe and S cycling at the study location.

The reaction network comprises 12 reaction pathways occurring during sedimentary organic matter degradation and authigenic mineral formation with a focus on the C, O, Fe and S cycles. The reaction stoichiometries and rate laws can be found in Tables 5.2 and 5.3 and the rate constants are listed in Table 5.1. OM remineralization can be coupled to O_2 (R_1), Fe_2O_3 (R_2) and SO_4^{2-} (R_3) reduction, and methanogenesis (R_4). CH_4 can be oxidized aerobically (R_5) and anaerobically (coupled to SO_4^{2-} reduction, R_6). The model accounts for the reoxidation of reduced metabolites (HS^-, R_7; Fe^{2+}, R_8) and sulfidic reduction of Fe_2O_3 (R_9). During authigenic pyrite formation (R_{10}) H_2 can be produced (Rickard 2012), which is assumed to be oxidized immediately by Fe_2O_3 (R_{10}^a) or SO_4^{2-} (R_{10}^b) or consumed by methanogenesis (R_{10}^c). Pyrite can react with oxygen (R_{11}). More reactive $Fe_2O_3^\alpha$ can convert into less reactive $Fe_2O_3^\beta$ (R_{12}).

Table 5.1: Model parameters

Description	Symbol	Value	Source
Environmental parameters			
Temperature	T	277 K	a
Sediment density	ρ_s	$2.5 \cdot 10^3$ kg m^{-3}	a
Salinity	S	35	a
Water depth		550 m	a
Porosity at sediment-water interface	ϕ_0	0.712	a
Porosity at depth	ϕ_∞	0.505	a
Porosity e-folding length	γ	0.023 m	a
Bioturbation coefficient at the sediment-water interface	D_{b0}	$1.82 \cdot 10^{-3}$ m^2 y^{-1}	b
E-folding length of bioturbation	q	$2 \cdot 10^{-2}$ m	b
Rate constants			
Rate constant for OM$^\alpha$ mineralization	k^α_{OM}	$1 \cdot 10^{-2}$ y^{-1}	a
Rate constant for OM$^\beta$ mineralization	$k_{\mathrm{OM}}\beta$	$6.2 \cdot 10^{-5}$ y^{-1}	a
Rate constant for OM$^\gamma$ mineralization	$k_{\mathrm{OM}}\gamma$	$6.2 \cdot 10^{-5}$ y^{-1}	a
Half-sat. constant aerobic respiration	$K_{\mathrm{m,O_2}}$	8 µM	c
Half-sat. constant Fe_2O_3 reduction	$K_{\mathrm{m,Fe(OH)_3}}$	$1.68 \cdot 10^2$ mM	c
Half-sat. constant organoclastic SO_4^{2-} reduction	$K_{\mathrm{m,SO_4}}$	$1 \cdot 10^{-1}$ mM	c
Half-sat. constant SO_4^{2-} in AOM	$K_{m,\mathrm{SO_4\text{-}AOM}}$	$1 \cdot 10^{-1}$ mM	c
Rate constant aerobic oxidation of methane	k_5	$1 \cdot 10^7$ m^3 mol^{-1} y^{-1}	c
Rate constant AOM	k_6	$1 \cdot 10^4$ y^{-1}	a
Rate constant HS^- oxidation	k_7	$1 \cdot 10^7$ m^3 mol^{-1} y^{-1}	d
Rate constant Fe^{2+} oxidation	k_8	$1.4 \cdot 10^6$ m^3 mol^{-1} y^{-1}	c
Rate constant sulfidic Fe_2O_3 reduction	k_9	$1 \cdot 10^{-1}$ m^3 mol^{-1} y^{-1}	a
Rate constant pyrite formation	k_{10}	$1 \cdot 10^3$ m^3 mol^{-1} y^{-1}	e
Rate constant pyrite oxidation	k_{11}	1 m^3 mol^{-1} y^{-1}	a

Continued on next page

Table 5.1 – continued from previous page

Description	Symbol	Value	Source
Rate constant Fe_2O_3 crystallization	k_{12}	$6 \cdot 10^{-1}$ y^{-1}	f
Parameters for solid-phase boundary conditions			
OM^{α} loading coefficients	$A_{OM\alpha}$	$3.125 \cdot 10^{2}$ kg m^{-3}	a
	$B_{OM\alpha}$	$3.75 \cdot 10^{-1}$ kg m^{-2} y^{-1}	a
OM^{β} loading coefficients*	$A_{OM\beta}$	$5.208 \cdot 10^{2}$ kg m^{-3}	a
	$B_{OM\beta}$	$6.25 \cdot 10^{-1}$ kg m^{-2} y^{-1}	a
$Fe_2O_3^{\alpha}$ loading coefficient	$C_{Fe_2O_3}$	$7.14 \cdot 10^{2}$ kg m^{-3}	a
OM^{γ} loading coefficient	$C_{OM\gamma}$	$2.31 \cdot 10^{3}$ kg m^{-3}	a

arameters and boundary conditions. Sources a = fitted/this study, b = Middelburg et al. (1997), c = Wang and Van Cappellen (1996), d = Meysman et al. (2015), e = Rooze et al. (2016), f = Berg et al. (2003); *parameters A and B relating to OM^{β} are set to lower values during particular time periods (see Table 3).

The OM loading of α and β phases at the sediment-water interface are modeled as fluxes that are partly a function of the sedimentation rate and partly constant:

$$F_j = A_j(1 - \phi_0)\omega(t) + B_j(1 - \phi_0) \tag{5.6}$$

The parameters A and B are generally kept constant (Table 5.1) except for three periods: from 20.5 to 18 kyr and from 15.3 to 14.5 kyr A and B of OM^{β} are lowered by 90%, and in the last 10 kyr B for OM^{β} is set to 0 (Table 5.4). The loading of the more refractory organic matter (OM^{γ}) and the $Fe_2O_3^{\alpha}$ phase are functions of the sedimentation rate:

$$G_j = C_j(1 - \phi_0)\omega(t) \tag{5.7}$$

where C is kept constant over the entire simulation period (Table 5.1). All solid Fe is initially deposited in the $Fe_2O_3^{\alpha}$ phase. The influx of pyrite is zero. For dissolved species, concentrations are fixed at the sediment-water interface, representative of conditions in the bottom water. The upper boundary concentration of O_2 is 0.225 mM, the concentration of SO_4^{2-} is 28 mM. All other solutes have an upper boundary concentration of 0. For all solids and solutes, zero-gradient boundary conditions are imposed at the bottom of the model domain. All CH_4 is produced in situ.

Initial conditions were set to 0 for all dissolved species, except for SO_4^{2-} (2.8 mM). The model was run with a 35 kyr spin-up (62.4 - 27.4 kyr BP) assuming a steady sedimentation rate (82 cm/kyr) and constant OM and Fe-oxide deposition. Since we cannot constrain the

Table 5.2: Reaction pathways

Primary redox reactions*	
R_1	$(CH_2O)_a(NH_3)_{b(aq)} + (a + 2\,b)\,O_2 \longrightarrow$
	$a\,CO_2 + (a + b)\,H_2O + b\,NO_3^- + b\,H^+$
R_2	$(CH_2O)_a(NH_3)_{b(aq)} + 2\,a\,Fe_2O_3^{\alpha+} 8\,a\,H^+ \longrightarrow$
	$a\,CO_2 + 4\,a\,Fe^{2+} + 5\,a\,H_2O + b\,NH_3$
R_3	$(CH_2O)_a(NH_3)_{b(aq)} + \frac{1}{2}aSO_4^{2-} \longrightarrow$
	$a\,CO_2 + \frac{1}{2}aHS^- + \frac{1}{2}aH_2O + \frac{1}{2}aOH^- + b\,NH_3$
R_4	$(CH_2O)_a(NH_3)_{b(aq)} \longrightarrow \frac{1}{2}aCH_4 + \frac{1}{2}aCO_2 + b\,NH_3$
Other reactions	
R_5	$2\,O_2 + CH_4 \longrightarrow CO_2 + 2\,H_2O$
R_6	$SO_4^{2-} + CH_4 + CO_2 \longrightarrow 2\,HCO_3^- + H_2S$
R_7	$HS + 2\,O_2 \longrightarrow SO_4^{2-} + H^+$
R_8	$2Fe^{2+} + \frac{1}{2}O_2 + 2\,H_2O \longrightarrow Fe_2O_3^{\alpha+}\,4\,H^+$
R_9	$\frac{1}{4}HS^- + Fe_2O_3^{\alpha,\beta}\frac{15}{4}H^+ \longrightarrow \frac{1}{4}SO_4^{2-} + 2\,Fe^{2+} + 2\,H_2O$
R_{10}	$Fe^{2+} + 2\,HS^- \longrightarrow FeS_2 + H_2$
R_{10}^a	$Fe_2O_3^{\alpha+}\,2\,HS^- + 4\,H^+ \longrightarrow FeS_2 + 2\,Fe^{2+} + 5\,H_2O$
R_{10}^b	$SO_4^{2-} + 4\,Fe^{2+} + 7\,HS^- + H^+ \longrightarrow 4\,FeS_2 + 4\,H_2O$
R_{10}^c	$CO_2 + 4\,Fe^{2+} + 8\,HS^- + 2\,H^+ \longrightarrow 4\,FeS_2 + CH_4 + 2\,H_2O$
R_{11}	$FeS_2 + \frac{7}{2}O_2 + H_2O \longrightarrow Fe^{2+} + 2\,SO_4^{2-} + 2\,H^+$
R_{12}	$Fe_2O_3^{\alpha} \longrightarrow Fe_2O_3^{\beta}$

* Subscript 'a' and 'b' denote the C:N ratio in organic matter, which was set to 106:16. Superscripts 'α' and 'β' indicate reactive and less reactive fractions of organic matter and iron oxides, whereas the 'γ' fraction only reacts with oxygen.

conditions during the spin-up (e.g., sedimentation rates, OM deposition), the first 5 kyr after the spin-up (27.4 - 22.4 kyr BP) are treated with caution and we only discuss model results produced for sediments younger than 22.4 kyr BP, which corresponds to the upper 20 m of the sediment core.

The initial model parameterization was developed based on literature values (see Table 5.1), combined with adjustments for local environmental conditions, the measured porosity profile, and a preliminary fit of the total organic carbon (TOC) profile. Subsequently, model parameters were adjusted to reproduce the observed contemporary predominantly ferruginous state of the pore-waters, to reasonably fit the measured solid phase profiles, and to match the present depth of the SMTZ. Keeping each parameter constant over the deposition period was not sufficient to fit the model to the data. Instead, extensive model simulation-data comparison indicated periods of lower-than-usual organic matter input, which was

Table 5.3: Rate laws

Primary redox reactions
$R_1^{\alpha,\beta} = k_{\mathrm{OM}}^{\alpha,\beta,\gamma}[\mathrm{OM}^{\alpha,\beta,\gamma}]\frac{[\mathrm{O_2}]}{[\mathrm{O_2}]+K_{\mathrm{m,O_2}}}$
$R_2 = k_{\mathrm{OM}}^{\alpha,\beta,\gamma}[\mathrm{OM}^{\alpha,\beta,\gamma}]\frac{K_{\mathrm{m,O_2}}}{[\mathrm{O_2}]+K_{\mathrm{m,O_2}}}\frac{[\mathrm{Fe_2O_3^\alpha}]}{[\mathrm{Fe_2O_3^\alpha}]+K_{\mathrm{m,Fe_2O_3}}}$
$R_3 = k_{\mathrm{OM}}^{\alpha,\beta,\gamma}[\mathrm{OM}^{\alpha,\beta,\gamma}]\frac{K_{\mathrm{m,O_2}}}{[\mathrm{O_2}]+K_{\mathrm{m,O_2}}}\frac{K_{\mathrm{m,Fe_2O_3}}}{[\mathrm{Fe_2O_3^\alpha}]+K_{\mathrm{m,Fe_2O_3}}}\frac{[\mathrm{SO_4^{2-}}]}{[\mathrm{SO_4^{2-}}]+K_{\mathrm{m,SO_4}}}$
$R_4 = k_{\mathrm{OM}}^{\alpha,\beta,\gamma}[\mathrm{OM}^{\alpha,\beta,\gamma}]\frac{K_{\mathrm{m,O_2}}}{[\mathrm{O_2}]+K_{\mathrm{m,O_2}}}\frac{K_{\mathrm{m,Fe_2O_3}}}{[\mathrm{Fe_2O_3^\alpha}]+K_{\mathrm{m,Fe_2O_3}}}\frac{K_{\mathrm{m,SO_4}}}{[\mathrm{SO_4^{2-}}]+K_{\mathrm{m,SO_4}}}$
Other reactions
$R_5 = k_5[\mathrm{O_2}][\mathrm{CH_4}]$
$R_6 = k_6\frac{[\mathrm{SO_4^{2-}}]}{[\mathrm{SO_4^{2-}}]+K_{m,\mathrm{SO_4}\text{-AOM}}}[\mathrm{CH_4}]$
$R_7 = k_7[\mathrm{O_2}][\mathrm{HS^-}]$
$R_8 = k_8[\mathrm{O_2}][\mathrm{Fe^{2+}}]$
$R_9^{\alpha,\beta} = k_9^{\alpha,\beta}[\mathrm{Fe_2O_3^{\alpha,\beta}}][\mathrm{HS^-}]$
$R_{10} = k_{10}[\mathrm{Fe^{2+}}][\mathrm{HS^-}]$
$R_{10}^a = R_{10}\frac{[\mathrm{Fe_2O_3^\alpha}]}{K_{\mathrm{m,Fe(OH)_3}}+[\mathrm{Fe_2O_3^\alpha}]}$
$R_{10}^b = (R_{10}-R_{10}^a)\frac{[\mathrm{SO_4^{2-}}]}{K_{\mathrm{m,SO_4}}+[\mathrm{SO_4^{2-}}]}$
$R_{10}^c = R_{10}-R_{10}^a-R_{10}^b$
$R_{11} = k_{11}[\mathrm{O_2}][\mathrm{FeS_2}]$
$R_{12} = k_{12}[\mathrm{Fe_2O_3^\alpha}]$

implemented as a 10-fold reduction of OM^β deposition between 20.5 kyr BP and 18 kyr BP, 15.3 kyr BP and 14.5 kyr BP, and after 10 kyr BP. Phases of OM^β deposition according to Eq. 5.6 will subsequently be named as (early to late) Phase I, III and V; intersecting phases of reduced OM deposition will be denoted Phase II, IV and VI (Table 5.4).

The model was implemented based on the early diagenetic modeling framework presented in Rooze et al. (2020). The size of the grid cells in the model increases exponentially from 1 mm at the top to 10 cm at 4.7 mbsf and remains constant from there on to the bottom of the domain at 29.8 mbsf. The time steps are variable, but limited to a maximum of 1 year.

5.3 Results

5.3.1 Geochemistry

Sediments at Site MOZ4-CS17 are mainly homogenous, featureless, hemipelagic mud of dark greenish to brownish gray color. The top 2 mbsf are of coarser grain size than the

remainder of the core. From the top of the core, SO_4^{2-} concentrations drop nearly linearly from seawater values (28 mM) to below detection limit at 12 mbsf (Fig. 5.2a). Throughout the core, no hydrogen sulfide was detected. While CH_4 has been detected in the topmost sample where it reaches 0.3 mM at 0.9 mbsf, it stays below 1 µM throughout nearly the entire sulfate-containing zone and only starts to rise again below 10 mbsf. It reaches 1.6 mM at 14 mbsf and stays elevated below that at around 1 mM, close to the methane saturation under shipboard conditions. An SMTZ is identified between ∼10 and ∼12 mbsf (Fig. 5.2a,b). Dissolved Fe concentrations are highly variable between 0 and 120 µM (Fig. 5.2c). Dissolved Fe is prevalent in two separated zones above and below the SMTZ. Within the SMTZ, dissolved Fe persists at low values < 10 µM. The $\delta^{13}C$ of CH_4 exhibits the most negative values of $\sim -100‰$ V-PDB within the SMTZ and increases downcore to $\sim -77‰$ at the bottom of the core. The CH_4 detected in the topmost sample exhibits the least negative measured$\delta^{13}C$ of $-75permil$ (Fig. 5.2d).

Pyrite is more abundant in the upper part of the record (Fig. 5.2e). The profile exhibits three maxima: around 3.5 mbsf (1.3 wt%); within the current SMTZ around 10 mbsf (2.1 wt%); and around 15 mbsf (1.8 wt%). Pyrite $\delta^{34}S$ is most negative at the sediment-water interface ($-40‰$) and gets steadily heavier downcore into the SMTZ where values of $-25‰$ are reached (Fig. 5.2f). The pyrite peak at 15 mbsf exhibits the least negative $\delta^{34}S$ of $-10‰$. Such values are again reached at $\sim$ 25 mbsf, without a corresponding pyrite peak. Reactive Fe ranges between 1 and 1.8 wt% (Fig. 5.2g). The highest values occur near the top and bottom of the core, and the lowest values between 15 and 20 mbsf. The measured TOC content exhibits an increase from 0.6 to 1.1 wt% from 1.2 to 3.5 mbsf, shows a slight decrease between 4 and 6 mbsf, and remains relatively constant at 1.14 ± 0.07 % below that (Fig. 5.2h).

The deepest cored interval at 33 mbsf has an age of 27.33 kyr. Sedimentation rates over the entire period of deposition vary by an order of magnitude. They reached values between 200 and 450 cm kyr^{-1} during the Late Glacial Maximum (LGM 26.5 - 20 kyr BP; Clark et al. 2009), dropped to 100 cm kyr^{-1} between 18 and 16.5 kyr BP, rose to 250 cm kyr^{-1} again at 16.5 kyr BP, and dropped stepwise until the top of the record. After 7500 kyr BP, sedimentation rates remained lower than 20 cm kyr^{-1} (Table 5.5; Fig. 5.3).

5.3.2 Modeling

Model simulations reproduce the main observed biogeochemical features, yielding a contemporary SMTZ positioned at $\sim$ 11 mbsf (Fig. 5.2a,b) and a pyrite profile exhibiting three distinct peaks at 3.3, 8.5 and 16.8 mbsf (Fig. 5.2e). Pore-waters are ferruginous over most of the sediment column except for the topmost few cm where oxic conditions prevail (Fig. 5.2b). In the topmost sediment layer, most OM is processed by aerobic degradation, which accounts for 0.04 mol C m^{-2} yr^{-1} (65 % of the total OM decomposition rate). Organoclastic sulfate reduction accounts for 0.018 mol C m^{-2} yr^{-1} (29%), while organoclastic iron reduc-

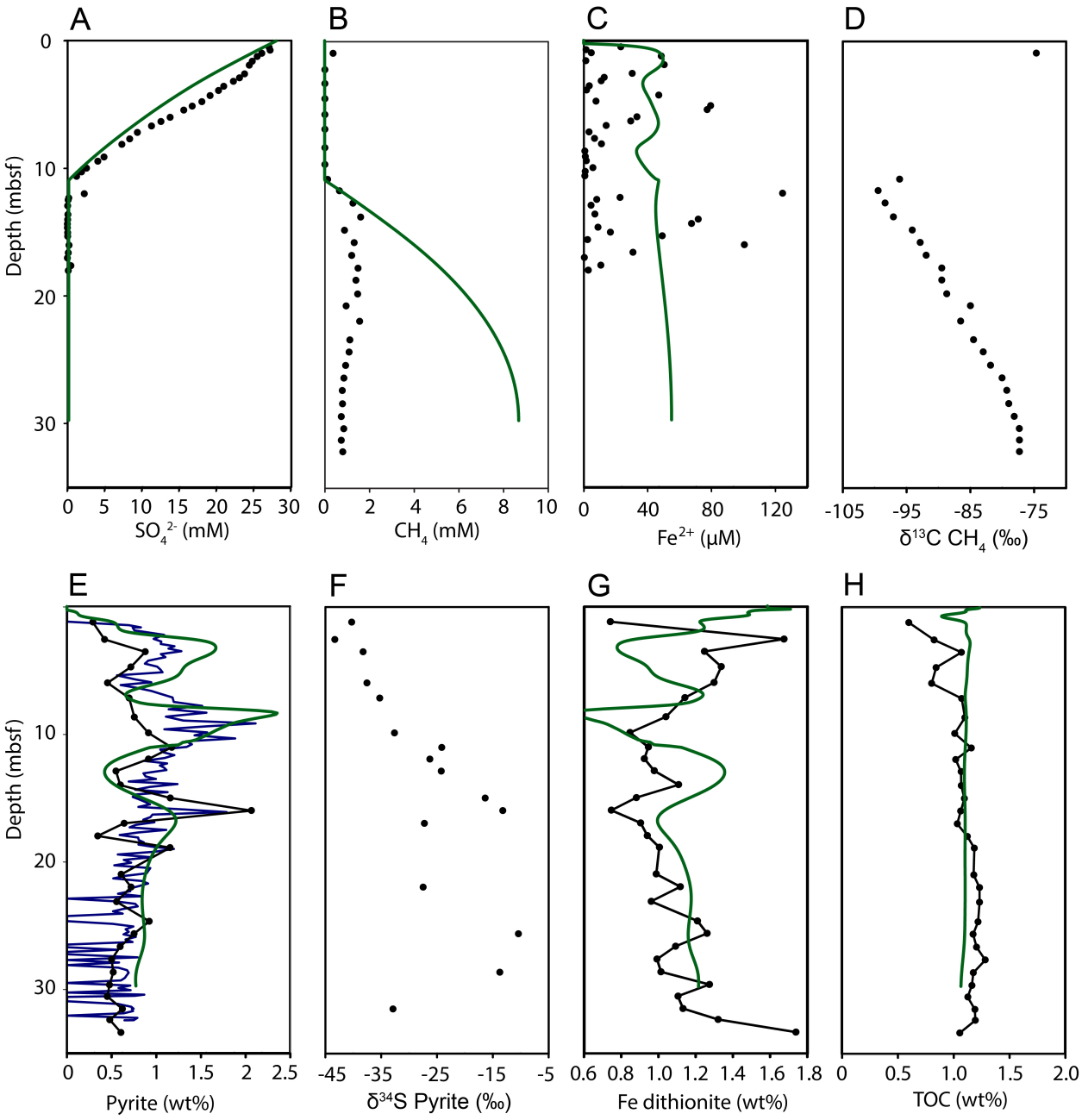

Figure 5.2: Geochemical profiles at Site MOZ4-CS17. Pore-water: a) SO_4^{2-} (black dots) in mM, b) CH_4 (black dots) in mM, c) Fe^{2+} (black dots) in µM, d) $\delta^{13}C$ of CH_4 in ‰ V-PDB. Solid phase: e) pyrite in wt % black line and dots from chromium reduction, blue line from XRD, f) $\delta^{34}S$ of pyrite in ‰ V-CDT, g) dithionite extractable Fe (black line and dots) in wt %, and h) TOC (black line and dots) in wt %. Solid green lines indicate model fits for SO_4^{2-}, CH_4, Fe^{2+}, pyrite, dithionite extractable Fe and TOC.

Table 5.4: Phases of model development in relation to the OM deposition pattern

Phase	Time of phase	Characteristics	Correspondence to paleo-event
I	before 20 kyr BP	High OM loading	LGM
II	20.5 - 18 kyr BP	Low OM loading	MWP 19 kyr
III	18 - 15.3 kyr BP	High OM loading	Early deglacial
IV	15.3 - 14.5 kyr BP	Low OM loading	MWP 1a
V	14.5 - 10 kyr BP	High OM loading	Bölling/Alleröd, Younger Dryas
VI	after 10 kyr BP	Low OM loading	Holocene

Phase boundaries have been aligned with calibrated ^{14}C dating points on core MOZ4-CS17. Correspondence to paleo-events are only used as a guideline. LGM = last glacial maximum, MWP = melt water pulse.

tion and methanogenesis process $7 \cdot 10^{-6}$ mol C m^{-2} yr^{-1} (¡1%) and 0.004 mol C m^{-2} yr^{-1} (6%), respectively. CH_4 producing processes (R_4 and R_{10c}) are currently generating 0.003 mol CH_4 m^{-2} yr^{-1} while 0.0077 mol CH_4 m^{-2} yr^{-1} are consumed by AOM, resulting in net CH_4 consumption of 0.0047 mol CH_4 m^{-2} yr^{-1}. This indicates that currently more CH_4 is consumed than produced in the model domain. The maximum rate of organoclastic sulfate reduction is found around 4 mbsf and a second peak is observed above the SMTZ. Methanogenesis starts in the SMTZ and remains elevated over the entire sediment column below the SMTZ, while AOM is restricted to the SMTZ (not shown). Pyrite is formed in the zones of AOM and organoclastic sulfate reduction.

The geochemical profiles exhibit strong transient features. The SMTZ migrated upwards during Phase I and II (20 to 18 kyr BP) from $\sim$ 11 mbsf to 7.8 mbsf (Fig. 5.4). From the beginning to the end of Phase III (18 - 15.3 kyr BP) it migrated downwards to a depth of $\sim$ 10 mbsf, and stayed there during Phase IV (15.3 - 14.5 kyr BP). Throughout Phase V (14.5 - 10 kyr BP) the SMTZ moved upward again until it reached $\sim$ 8 mbsf. In Phase VI (10 kyr BP - today) the depth of the SMTZ stayed initially stable at 8 mbsf, but then continually moved downwards from 6.5 kyr BP to today, where it is now at 11 mbsf.

A first pyrite peak emerged from 19 - 17 kyr BP (transition Phase II to III) at the depth of the SMTZ (8.2 mbsf) and was then preserved and buried to its current depth at 16.1 mbsf. From 16 - 14 kyr BP (Phase III – V), a small second peak was formed in the upper $\sim$ 5 m in the organoclastic sulfate reduction zone. This peak was buried and began to grow more rapidly around 12 kyr BP (Phase V) as it approached the SMTZ. From 10 - 5 kyr BP (Phase VI) the peak moved past the SMTZ, while new pyrite continued to precipitate

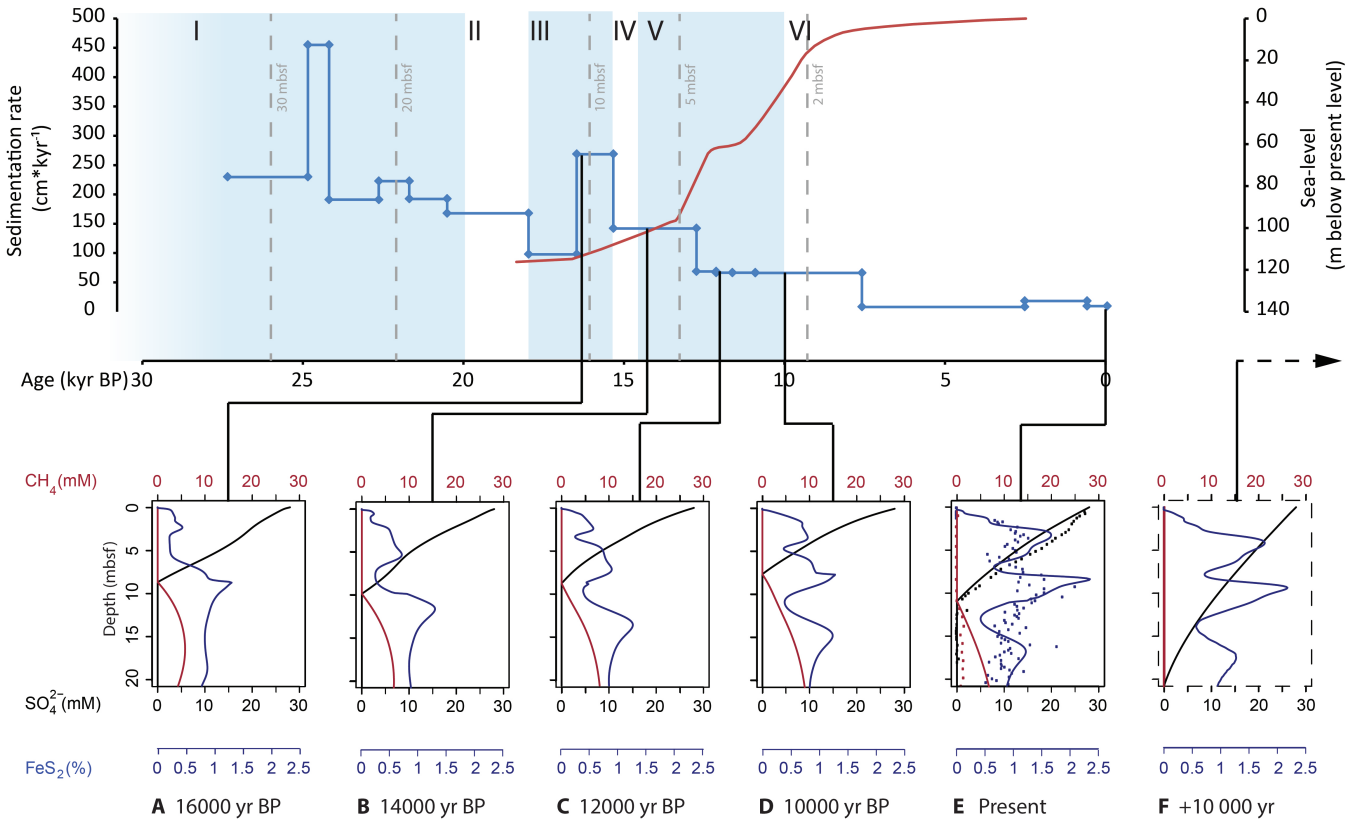

Figure 5.3: Temporal evolution of modeled (in small plots A-F) sulfate (black), methane (red), and pyrite (blue) in response to sedimentation rate (blue) and paleo-sea-level (red; Camoin et al. 2004) in the upper plot. Roman numerals indicate phases of OM deposition (see Table 5.4). Blue shaded background indicates phases of normal OM deposition; white shaded phases indicate phases of reduced OM deposition. Gray stippled vertical lines indicate corresponding depth in sediment core MOZ4-CS17.

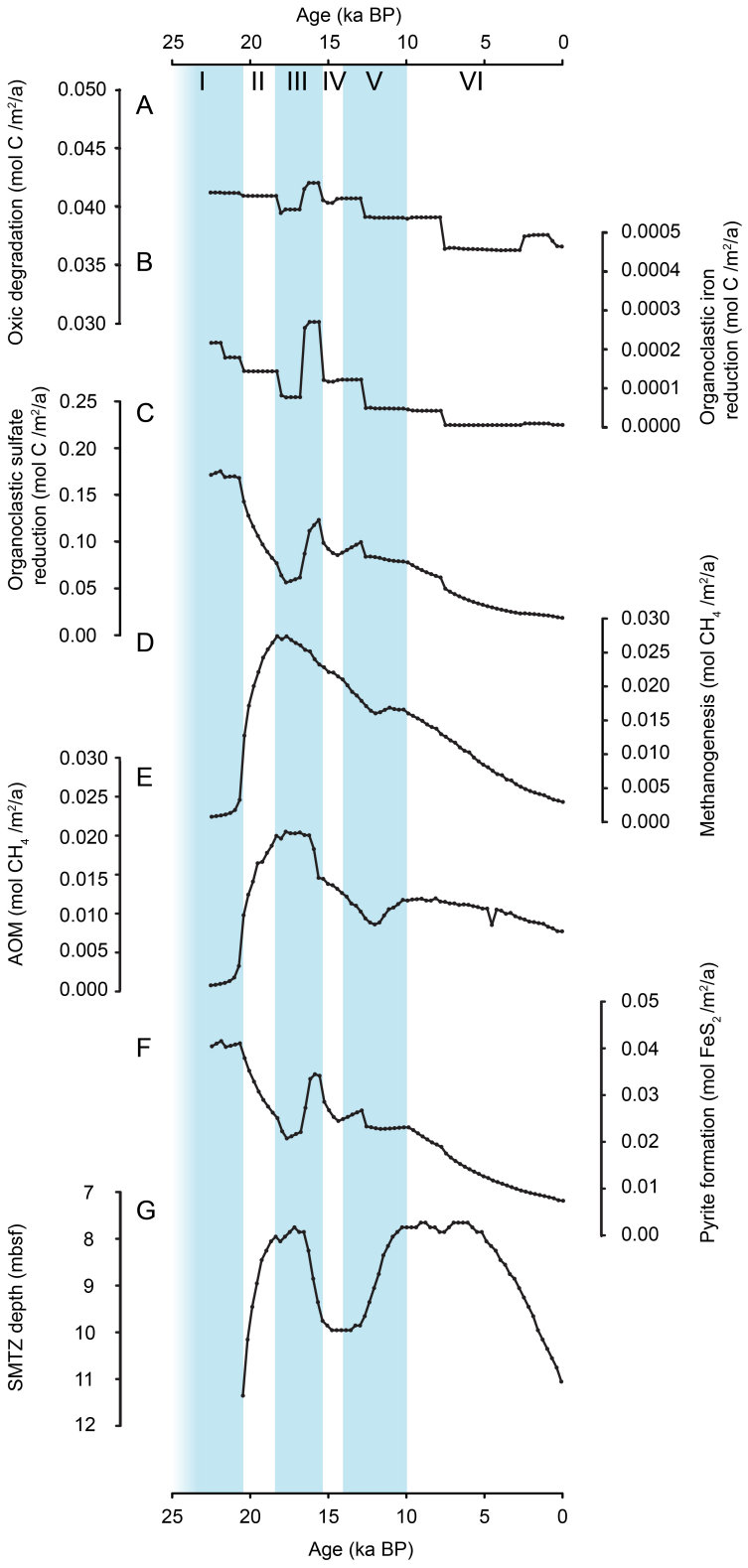

Figure 5.4: Depth-integrated reaction rates over time. a) oxic degradation, b) organoclastic iron reduction, c) organoclastic sulfate reduction, d) methanogenesis, e) AOM, f) pyrite formation, g) smtz depth (note reversed Y-axis) Blue shades correspond to phases of high OM deposition as in Table 3.

rapidly at the depth of the SMTZ, resulting in the overall skewed shape of the pyrite profile. The peak broadened over the last 5 kyr when downward migration of the SMTZ exceeded the burial velocity, leading to the separation between the pyrite peak at 8.5 mbsf and the SMTZ located at 11.3 mbsf today. Starting around 13.5 kyr BP (Phase V), the third peak emerged in the upper 3 m, and has continued to grow and migrate downwards to its present depth at 3.3 mbsf.

Reaction rates throughout the past 27 kyr were higher than today (Fig. 5.4). Organoclastic iron reduction, organoclastic sulfate reduction, and pyrite formation all exhibit maximum rates during Phase I and Phase III, coinciding with the highest sedimentation rates. At their highest, the reaction rates are $2.7 \cdot 10^{-4}$ mol C m^{-2} yr^{-1} (organoclastic iron reduction), 0.17 mol C m^{-2} yr^{-1} (organoclastic sulfate reduction) and 0.04 mol pyrite m^{-2} yr^{-1} (pyrite precipitation). Methanogenesis and AOM peak during Phase III with values of 0.027 mol CH4 m^{-2} yr^{-1} (methanogenesis) and 0.02 mol CH_4 m^{-2} yr^{-1} (AOM).

5.4 Discusion

5.4.1 Contemporary geochemical profiles

SO_4^{2-} concentrations decrease from 28 mM at the sediment surface to 0 in the SMTZ, with model results suggesting that organoclastic sulfate reduction mostly takes place in the upper $\sim$ 5 m of the sediment column. Deeper, towards the SMTZ, AOM predominates SO_4^{2-} consumption explaining the nearly linear SO_4^{2-} profile above the SMTZ (Borowski et al. 1996). Pyrite above the SMTZ (0.9 – 1.3 wt%) has more negative $\delta^{34}S$ values (-45 to -25‰), indicating that the sulfide was produced during organoclastic sulfate reduction and formed closer to the sediment-water interface (Hartmann and Nielsen 1968; Jørgensen 1979). The significant contribution of organoclastic sulfate reduction to the isotopic signal is supported by the model outcomes (see section 5.5).

Organoclastic iron reduction is a minor contributor to organic matter degradation over the entire simulated period. Yet, the porewaters are mostly in a ferruginous state with abundant dissolved Fe^{2+} but no free HS^-. In our model, most of the Fe^{2+} is produced by re-oxidation of HS^- with Fe_2O_3. To titrate out all HS^-, iron (oxyhydr)oxides must be able to persist beyond the depth of OM oxidation into the zone of AOM, which is consistent with our measurements (Fig. 5.2g) and accomplished in the model by the $Fe_2O_3^{\beta}$ pool that is unreactive towards OM (Reed et al. 2011; Rooze and Meile 2016). This emphasizes the importance of iron cycling in the sediment at depths > 10 m, and contrasts with findings at the Congo lobes where Taillefert et al. (2017) documented strong organoclastic iron reduction in the top meter of sediment.

The high pyrite and low dissolved Fe^{2+} concentrations at the depth of the current SMTZ (10 mbsf, Fig. 5.2a,b) indicate active pyrite formation, which is supported by the model.

The amount of pyrite in this interval relative to deeper in the core suggests that this SMTZ has been within the same sediment horizon for a longer time period, i.e., that the distance between the SMTZ and the sediment-water interface increases approximately at the speed of the burial velocity. This is only possible under the low sedimentation rate conditions dominating the last 10 kyr. The CH_4 budget shows net consumption, implying that the CH_4 currently diffusing upwards into the SMTZ has been produced in the past and the CH_4 pool is now progressively being depleted. As such, the SMTZ is expected to continue to migrate deeper into the sediment as sulfate diffusion into the sediment outpaces methane production. The $\delta^{13}C$ of CH_4 indicates that it has been produced by biogenic methanogenesis alone with no thermogenic contribution (Schoell 1980; Whiticar 1999). This has also been confirmed by Deville et al. (2020) and justifies the assumption of no methane influx from below.

5.4.2 Variations in sedimentation rate and organic matter input

Sea-level has risen by 120 m following the LGM (Fairbanks 1989; Camoin et al. 2004; Peltier and Fairbanks 2006), leading to flooding of the previously dry Mozambique continental shelf and a marine transgression shifting the coastline 50 - 100 km inland (Beiersdorf et al. 1980). Periods of rapid post-glacial and deglacial sea-level rise have been detected as melt water pulses in paleo-sea-level records (Fairbanks 1989Fairbanks, 1989; Bard et al. 1990; Deschamps et al. 2012). At the Mozambique margin sea-level changes have had major impacts on the distance from the Zambezi river mouth to the study site and the near-shore current system (Fig. 1). Changes in climate also affected rainfall, land erosion, vegetation along the river, and connectivity between different parts of the Zambezi catchment (Schefuß et al. 2011; Just et al. 2014). These factors can have had an impact on the delivery of sediments and OM to our study site.

During the last glacial sediments from the Zambezi were transported directly to deeper waters of the continental slope and displaced southward by the prevailing ocean currents (Lubbe et al. 2014). At Site CS17 highest sedimentation rates are observed between 25 and 24 kyr BP, during Phase I, potentially related to the LGM sea-level lowstand prior to the onset of the large-scale global sea-level rise (Ramsay and Cooper 2002).

The meltwater pulse (MWP) 19 kyr ago during phase II (Clark et al. 2004) is associated with 15 m sea-level rise from 120 to 105 m below present level, which was not sufficient to raise the sea-level over the Mozambique shelf break which today is between 90 and 100 m water depth (Beiersdorf et al. 1980). Hence, it did not cause a significant shoreline retreat. Thus, it also had a limited effect on sedimentation rates at Site MOZ4-CS17 (Fig. 5.3). However, fitting the geochemical profiles required a reduced OM deposition relative to the sedimentation rate during this time-interval (Table 5.4).

MWP 1A (14.6 kyr BP, during Phase IV, Table 5.4; Deschamps et al. 2012) is the major deglacial MWP associated with a significant shoreline retreat at the Mozambique margin (Wenau et al. 2020). This event also appears to have had a weak effect on the sedimentation

Table 5.5: Radiocarbon dating

Depth (m)	Species	^{14}C age (yr BP)	error (1σ)	Calendar age range (yr BP, 2σ)
0.06	bulk planktic	1,110	30	500-617
0.415	bulk planktic	2,910	30	2,345-2,612
0.835	bulk planktic	7,260	30	7,510-7,645
3.035	bulk planktic	10,090	30	10,744-11,044
3.510	bulk planktic	10,630	30	11,369-11,838
3.845	bulk planktic	10,850	30	11,893-12,276
4.265	shell	11,410	40	12,625-12,844
7.945	bulk planktic	13,370	50	15,096-15,477
11.015	bulk planktic	14,220	40	16,264-16,677
12.485	shell	15,320	40	17,802-18,109
16.470	shell	17,560	60	20,291-20,689
19.010	bulk planktic	18,460	50	21,489-21,875
21.125	bulk planktic	19,330	60	22,441-22,834
24.080	bulk planktic	20,670	70	23,948-24,391
27.085	bulk planktic	21,190	70	24,519-25,155
32.835	bulk planktic	23,570	100	27,112-27,540

Radiocarbon ages performed at the Beta Analytic Laboratory (Florida, USA) and calibrated age ranges at the 95% confidence interval used for the depth-age model. The MARINE13.14C curve (Reimer et al. 2013) was used to calibrate the ages after applying a marine reservoir correction (Reimer and Reimer 2001; Southon et al. 2002).

rate, but required a lower OM loading relative to the burial velocity (Table 5.4). The apparent weak imprint of MWP 19 kyr and MWP 1A on sedimentation rates observed at Site MOZ4-CS17 (Fig. 5.3) may in part be due to the resolution of our age model (and potentially also the sea level reconstructions), wherein sedimentation rates are averaged over thousands of years between individual dating points (Table 5.5). Their effect may also be obscured by high variability in sedimentation rates (Schulz et al. 2011) and deflections of the river plume. Previous studies showed that wetter periods in South-East Africa, i.e., Heinrich Stadial 1 (17-15 kyr BP) and the Younger Dryas (13-11.4 kyr BP), affected the predominant source area and composition of the material transported by the Zambezi (Schefuß et al. 2011; Just et al. 2014). However, these events appear to have neither strongly affected the sedimentation rates nor the OM loading at MOZ-CS17.

At the beginning of the Holocene, MWP 1B at 11.3 kyr BP (Phase VI, Table 5.4; Bard et al. 1990) led to flooding of a large part of the Mozambique shelf (vLubbe et al. 2014). From this time onwards, Zambezi sediments are transported by a strong countercurrent flowing on the shelf along the coast in northeasterly direction (Fig. 5.1), not reaching the main Pleistocene deposition centers beyond the shelf break anymore (Lubbe et al. 2014). This deflection of the main sediment source is reflected in the much lower sediment and OM deposition at Site MOZ4-CS17 during the last 10 kyr.

5.5 Response of early diagenetic processes and imprint on pyrite

The sedimentation rate affects pyrite accumulation directly by diluting and burying newly formed pyrite. The variation of the burial velocity over time thus contributes to the vertical variability seen in the pyrite profile, but is insufficient to cause the formation of distinct peaks. Instead, the sedimentation rate and the OM loading affect pyrite accumulation more strongly through their effect on organoclastic sulfate reduction and AOM, as pyrite precipitation under ferruginous conditions depends on the production of HS^-.

The contributions of both organoclastic sulfate reduction and AOM are supported by the measured isotopic composition of the pyrite peaks. The pyrite peak at 3.3 mbsf formed - according to the model simulations - in the zone of organoclastic sulfate reduction. It exhibits a more negative $\delta^{34}S$ isotope signature of $-40‰$ (Fig. 5.2f), which is consistent with open system conditions and a constant supply of fresh SO_4^{2-} (Hartmann and Nielsen 1968; Jørgensen 1979). The model displays growth of the pyrite peak currently located at 8.5 mbsf on top of an already existing peak formed by organoclastic sulfate reduction (Fig. 5.3). This is supported by the intermediate $\delta^{34}S$ value of $-25‰$, which indicates a mixed signal between organoclastic sulfate reduction and AOM-derived pyrite. The model simulations suggest that the deeper peak at 16 mbsf was mainly formed from AOM-derived sulfide. This is consistent with the much heavier $\delta^{34}S$ of $-10‰$, suggesting pyrite formation

under conditions with increasingly limited SO_4^{2-} supply (Borowski et al. 2013). This $\delta^{34}S$ value of $-10‰$ still has a 30‰ offset from seawater SO_4^{2-}. This would be at odds with the total SO_4^{2-} depletion in the SMTZ suggesting that some SO_4^{2-} produced by organoclastic sulfate reduction during an earlier depositional period contributes to this peak as well.

About 25 kyr BP, which is 5 - 6 kyr before the peak today located at 16 mbsf began to form, high sediment and OM deposition (Fig. 5.3) steepened the sulfate gradient, primarily through organoclastic sulfate reduction, but not AOM. Depth-integrated pyrite precipitation rates already peaked before 20 kyr BP (Fig. 5.4). When the SMTZ began to move upward $\sim$ 20 kyr BP, AOM rates increased and the formation of the pyrite peak commenced 1 kyr thereafter. The formation of the pyrite peak 19.4 - 17 kyr BP is driven by high sulfide production during AOM localized in the SMTZ, not by organoclastic sulfate rates spread out over a larger depth interval, despite having in general higher depth-integrated rates (Fig. 5.4).

The onset of the formation of the second pyrite peak in the upper sediments 16 - 14 kyr BP coincides with a doubling of the sulfate influx at the top which is driven by a steepened sulfate gradient into the sediment. This gradient results from higher organoclastic sulfate reduction rates closely following the increase in OM loading and sedimentation rates starting at $\sim$ 16.5 kyr BP (Fig. 5.3,5.4). Most of the growth of this peak occurred much later, driven by AOM-derived sulfide near the SMTZ. The peak shape is affected by the upward movement of the SMTZ 14.5 - 10 kyr BP, caused by high methanogenesis rates under increased sedimentation rates and OM loading 16.5 - 12.7 kyr BP (Phases III – V). This is followed by a downward movement of the SMTZ from $\sim$ 8 kyr BP and onwards, driven by lower methanogenesis rates under decreased sedimentation rates and OM loading, starting from 13 kyr BP (Fig. 5.3,5.4).

The emergence of the pyrite peak 13.5 kyr BP (located at 3.3 mbsf today) is associated with the upward movement of the SMTZ during that period, as a steeper sulfate concentration gradient leads to higher diffusive influx of sulfate, which in turn fuels pyrite formation with sulfide produced during organoclastic sulfate reduction. Further growth of this peak while the SMTZ moved downward in the last $\sim$ 6.5 kyr has been limited.

5.6 Synthesis

Along ocean margins, sedimentation rates and OM loading have varied substantially since the LGM with overall decreasing trends as sea-level rise increased the distance of previous depositional centers from the river mouth. On the Mozambique continental slope, abrupt decreases were observed $\sim$ 12.7 and 8 kyr BP, which were likely to be caused by subsequent changes in the current system on the shelf as it became gradually flooded. The re-routing of sediments in response to deglacial sea-level rise led to a transition from coastal conditions to a more open marine setting at our study site, characterized by lower depth-integrated

rates of organic mineralization including organoclastic sulfate reduction, AOM, and pyrite precipitation (Fig. 5.4). The simulations show that the methane being consumed today was produced in the past, causing the still ongoing downward migration of the SMTZ over the last 6500 years.

Our work shows that the sediment geochemical profiles are the result of repeated changes in depositional forcings driven by a global transition out of a glacial maximum climate state. The long-term evolution of the diagenetic system at Site MOZ4-CS17 can be described as follows (Fig. 5.5):

1. Before 20 kyr BP (Phase I): High sedimentation rates are associated to high OM deposition and high rates of methanogenesis. During the glacial period, high sedimentation rates dilute pyrite concentrations. In our simulations, this period is less well constrained, as it is influenced by environmental processes that occurred prior to the onset of our record.

2. 20 - 10 kyr BP (Phase II, III, IV and V): The post-glacial and deglacial are characterized by decreasing sedimentation rates and variable but overall low OM loading. Despite simultaneously decreasing pyrite formation rates, pyrite peaks form in specific intervals, as the lower sedimentation rate allows for higher pyrite accumulation and variations of OM loading keep the SMTZ stable in the same sediment interval over longer timescales.

3. 10 kyr BP - Present (Phase VI): Continuing low sedimentation rates, low OM input and decreasing CH_4 production at depth during the Holocene lead to gradual deepening of the SMTZ at approximately the speed of the burial velocity. Pyrite continues to accumulate in the SMTZ, which is fed by CH_4 formed during previous phases.

The most intense accumulation of diagenetic minerals at Site MOZ4-CS17 took place at the transition between the coastal/shelf-like high sedimentation and the deep-sea-like low sedimentation regimes. During periods of high sedimentation rates, the SMTZ was driven to shallower depth due to strong upward CH_4 diffusion, preventing the accumulation of pyrite in a single sediment interval. This can still be seen in the observed sedimentary pyrite profile below 20 mbsf where the pyrite concentrations are relatively uniform. During these time periods (e.g., Phase I), total sulfate consumption was ¿ 0.08 mol S m^{-2} yr^{-1}, typical for continental shelves or slopes (e.g. Bowles et al. 2014). When sedimentation rates dropped, the system was initially charged with pre-formed CH_4 and dissolved Fe^{2+}, which caused high overall SO_4^{2-} consumption rates (end of Phase III). The decreasing sedimentation rates, however, lowered total sulfate consumption to 0.017 mol m^{-2} yr^{-1} under modern conditions, representative for deep-sea environments, eventually causing a downward movement of the SMTZ in relation to the sediment surface, keeping the zone of pyrite formation within the same sediment interval. This led to initially stronger pyrite accumulations over the last 10 kyr in the respective sediment intervals. A back-of-the-envelope calculation using typical

modeled values for pyrite formation and sedimentation rates exemplifies this: A pyrite formation rate of 0.3 mol FeS_2 m^{-2} yr^{-1} at a sedimentation rate of 150 cm kyr^{-1} as observed during Phase II would cause a pyrite accumulation of 20 mol m^{-3} sediment. A pyrite formation rate of 0.01 mol m^{-2} yr^{-1} at a sedimentation rate of 10 cm kyr^{-1} as in Phase VI accumulates 100 mol pyrite m^{-3}. Provided that sedimentation rates and OM deposition remain low, methanogenesis will become negligible and the SMTZ will continue to move deeper into the sediment, AOM rates will decrease and new pyrite formation will stop. Eventually, the pyrite peaks formed in a paleo-SMTZ will be located above the position of the actual SMTZ (Fig. 5.3f). The stark difference in sulfate consumption rates stated above illustrate how fundamentally the depositional environment and the resulting diagenetic processes at Site MOZ4-CS17 have changed over the last deglacial period. Essentially, a sea-level change of only $\sim$ 120 m moved the diagenetic system (in terms of SO_4^{2-} consumption rates) an entire category in the framework of Bowles et al. (2014) towards biogeochemically lower activity.

Our analysis and quantitative interpretation of the sediment record on the Mozambique margin documents that global climate and associated sea level change is recorded in a massive shift in biogeochemical processes, which in turn affects and in part overprints the primary climatic signal recorded in the sedimentary record. As the sea-level related changes of sedimentation rates occurred along continental margins worldwide, this conceptual model is applicable to other settings as well. Therefore, our findings can help quantifying marine sedimentary C turnover along continental margins over the last glacial-interglacial transition. They can further provide a guideline for the interpretation of pyrite accumulations in marine sediments as indicators for changes in the depositional environment.

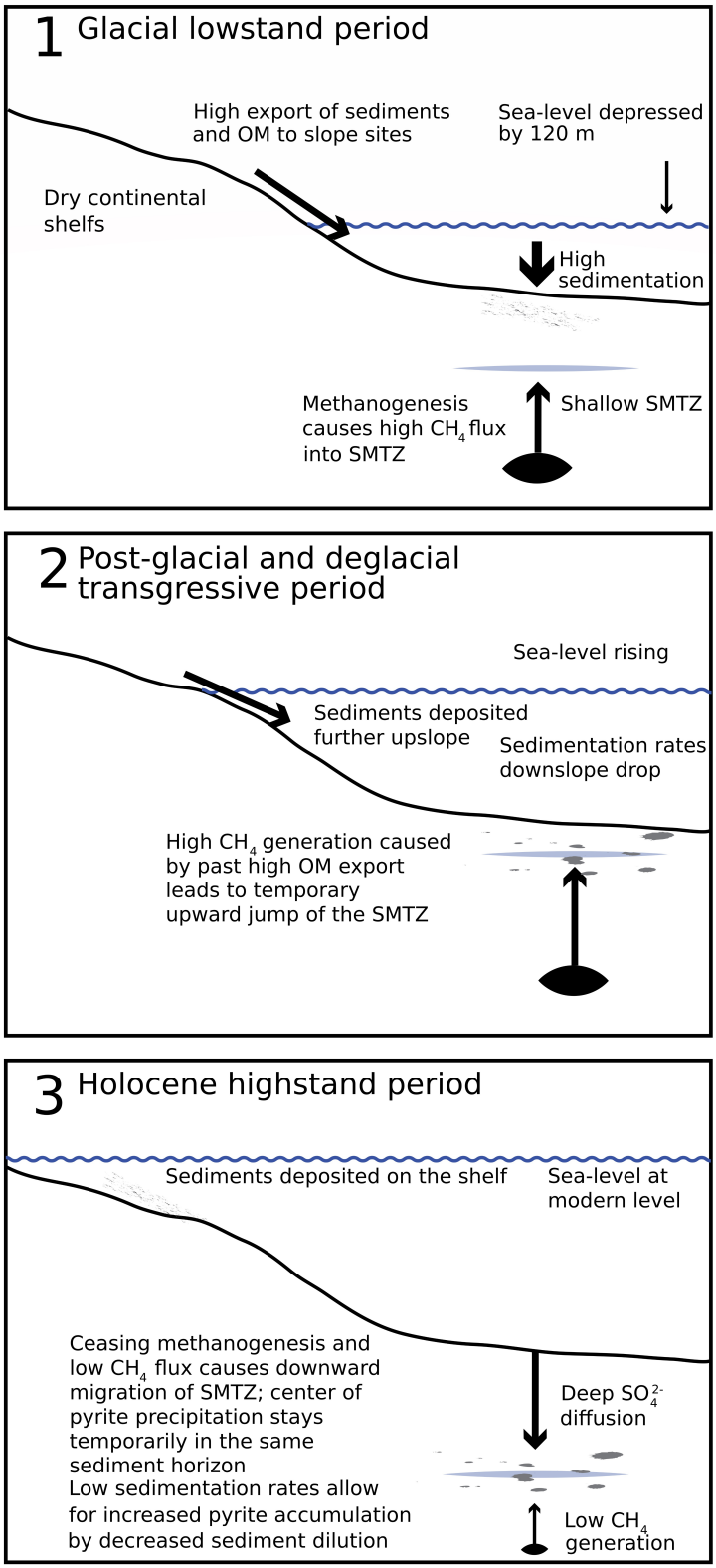

Figure 5.5: Schematic illustration for diagenetic evolution at the Mozambique margin (not to scale). Panels 1 - 3 correspond to the three-step conceptual model discussed in the text.

Chapter 6

Summary

This dissertation highlights the critical role transport processes, and advection in particular, play in biogeochemical dynamics in sediments. Despite large uncertainties in the parameterization of reaction rates, the studies (especially chapters 4 and 5) demonstrate that when the transport processes are constrained, reasonable estimates can be made with reaction-transport models of the biogeochemical turnover rates and sediment effluxes.

From prior work at cold seep sites, it is clear that stress at the sediment-water interface induced by variations in hydrostatic pressure can affect gas and water effluxes from the sediment. In chapter 2 we introduced a new concept in which these fluxes are directly modulated by compression and expansion of the gas phase. The reviewed observational data does not conclusively support that the flow dynamics are driven by this mechanism, as the tides can affect flow through other mechanisms as well: (1) Capillary activation of flow has been used to tentatively explain flow patterns both in-phase and out-phase with the tidal cycle (Wiggins et al. 2015; Leifer 2019). (2) Intermittent flow patterns have been related to sediment dilation and consolidation (e.g. Scandella et al. 2011; Sirhan et al. 2019). This concept has been supported by experimental and model studies, but may not explain situations with continuous seepage and out-phase water- and gas flow. (3) Gas hydrate dynamics may play an important role (e.g. MacDonald et al. 1994), but are poorly constrained and its relation to tidal cycles unclear. (4) Complex subsurface fault or fracture connectivity may further complicate flow patterns (Leifer 2019).

The model can be improved by incorporating non-ideal gas behavior and including dispersion of tidal pressure signals in the sediment. The relation of spatial correlations between flow from discrete seep locations fed by a single source can be explored by modeling more complicated flow conduit networks. Modeling site-specific subsurface structures obtained from seismic studies may allow measured gas and water flux time-series to be fitted.

Conservative tracers can be used to constrain average flow velocities in surficial seep sediments on the time-scales of months. This deviates from flow measured with flux meters, which can capture tidal signals and other temporal variations in flow at the sediment-water

interface. Even though tidal variations may lead to peak velocities ten times higher than the average flow velocity, the 2nd chapter showed that the vertical movement of water during a tidal cycle ($s = ut$) is very small, so may not directly affect the biogeochemistry in the sediment. The use of radium as a tracer has the advantage that it can also be used at non-brine seeps. It therefore complements the quantification of seepage velocities from chloride profiles, which requires a salinity gradient in the porewater due to either the presence of a brine fluid, or freshening of porewaters due to dehydration reactions at depth. Chapter 3 further showed that large uncertainties are associated with flow estimates based on chemical tracers due to uncertainties in the sediment tortuosity and randomness in the permeability field. The significant upward flow constrained from a radium profile sampled at GC699 was surprising, as it was designated as a control site, where visual indicators of upward flow were absent (Peterson 2019). For future research, it will be useful to test more control sites and to ground truth estimates based on conservative tracers with direct measurements of flow at the same location and over a time span similar to tracer residence time in the upper sediment.

Bioirrigation forms an important driver of flow in coastal sediments. In chapter 4, we demonstrated its effect on the N isotope effect of benthic fixed nitrogen removal, fitting the model to data of Brandes and Devol (1997). In line with other studies the chapter highlighted the importance of coupling between nitrogen consuming chemical reaction pathways for the overall benthic N isotope effect. This makes constraining the nitrogen isotope effect experimentally more challenging as it requires measuring the isotopic composition of various nitrogen species (Lehmann et al. 2007; Alkhatib et al. 2012; Dale et al. 2014). The behavior of burrowing organisms leads to spatiotemporal variability, potentially demanding the need to sample at multiple locations and times. The nitrogen isotope effects of various biogeochemical pathways in the model are mostly based on pure culture studies or N isotope effects measured in oxygen minimum zones in the open ocean. Kritee et al. (2012) showed that the N isotope effect of denitrifiers may depend on environmental factors. As the model results depend on reaction pathway-specific N isotope effects, in-situ measurements of intrinsic N isotope effects in sediments can potentially improve model predictions.

The chapter about the Zambezi delta showed how sedimentation affects early diagenetic processes and ultimately pyrite formation over millenial time-scales. With the aid of the model the importance of legacy effects was identified, as there is a lag in the effect of changes in sedimentation rates and organic matter loading on pyrite formation on the order of 5,000 years. Also, methane that accumulated millenia ago still fuels methanogenesis today. The data used in the study comes from one location in the delta. The changing distance from the river mouth, local random variations in sedimentation, and the effect of currents on local deposition are likely to impact the results. To study the history of diagenesis in the Zambezi delta in general, it will be useful to analyze data from other sampling locations as well. As the changes in the organic matter loading were mainly imposed to fit the pyrite profile, it

will be of particular interest to test if the same transient scenario pertains to other locations in the delta. This will help to identify the role of climate change and distinguish it from randomness in deposition trends. Also it will be interesting to compare the evolution of early diagenetic patterns at the Zambezi delta during deglaciation with those at other river deltas and possibly the Baltic Sea.

Appendix A

Tidally Oscillating Flow Model[1]

```
import numpy as np
from scipy.integrate import odeint
import matplotlib.pyplot as plt
import pdb
import pickle

#general equations
def gas_density(p):
    return gas_dens_ref + compressibility * p

#Van Genuchten relative permeabilities
def relativeperm_gas(water_sat, n = 3.0, gamma = 1.0/3.0, res_watersat = 0.0,
    res_gassat = 0.0):
    eff_water_sat = (water_sat - res_watersat) / (1 - res_watersat -
    res_gassat)
    eff_gas_sat = 1 - eff_water_sat
    return (eff_gas_sat**gamma) * (1 - (1 - eff_gas_sat)**(n/(n-1)))**(2*(n-1)
    /n)

def relativeperm_water(water_sat, n = 3.0, eps = 0.5, res_watersat = 0.0,
    res_gassat = 0.0):
    eff_water_sat = (water_sat - res_watersat) / (1 - res_watersat -
    res_gassat)
    return (eff_water_sat**eps) * (1 - (1 - eff_water_sat**(n/(n-1)))**((n-1)/
    n))**2

#Van Genuchten capillary pressure
def capillary_pres(water_sat, n = 3.0, alpha = 0.33):
    m = 1 - 1/n
    a = 1/alpha
    b = -1/m
```

[1]Supplement in relation to chapter 2

```
    c = 1/n
    return a * (water_sat**b - 1)**c

#derivative of capillary pressure w.r.t. water saturation
def dcapillary_pres_dsaturation(water_sat, n = 3.0, alpha = 0.33):
    m = 1 - 1/n
    a = 1/alpha
    b = -1/m
    c = 1/n
    Sw = water_sat
    return a*c*(Sw**b - 1)**(c-1) * b*Sw**(b-1)

def tidal_pressure(t):
    return water_dens * g * amplitude * np.sin(2 * np.pi * t / time_period)

#Finite volume approximation of Darcy flow for gas and water
def FV_Darcyflow(water_pres, water_sat, t):
    pw = water_pres #pressure water-phase
    Sw = water_sat #water saturation
    pg = pw + capillary_pres(Sw) #pressure gas-phase

    #finite differences for spatial derivatives
    dpw_dz = np.convolve(pw, [1, -1], 'same') / dz
    dpg_dz = np.convolve(pg, [1, -1], 'same') / dz
    #upper b.c. p(0,t) = f(t)
    dpw_dz[0] = 2 * (pw[0] - tidal_pressure(t)) / dz
    #ignore capillary pressure of gas-water interface in ocean
    dpg_dz[0] = 2 * (pg[0] - tidal_pressure(t)) / dz

    #gas density mid cells (where pressure is computed)
    gas_dens = gas_density(pg) #kg/m3
    #gas density at cell boundaries
    gas_dens_up = gas_density(tidal_pressure(t))
    gas_dens_mid = 0.5 * (gas_dens[0:(N-1)] + gas_dens[1:N])
    gas_dens_bnd = np.append(gas_dens_up, gas_dens_mid)

    #excess pressure of water and gas
    excess_dP_dz_water = dpw_dz - water_dens * g
    excess_dP_dz_gas = dpg_dz - gas_dens_bnd * g

    #water mobility and Darcy velocity at boundaries
    wmob_up = relativeperm_water(Sw[0]) / water_visc
    wmob_mid = relativeperm_water(0.5 * (Sw[0:(N-1)] + Sw[1:N])) / water_visc
    wmob_bnd = np.append(wmob_up, wmob_mid)

    #wmob_bnd = relativeperm_water(Sw) / water_visc #upwind
    q_water_bnd = - wmob_bnd * abs_perm * excess_dP_dz_water
```

```
    #gas mobility and Darcy velocity at boundaries
    gmob_up = ((relativeperm_gas(1) * (excess_dP_dz_gas[0] <= 0)) + \
               (relativeperm_gas(Sw[0]) * (excess_dP_dz_gas[0] > 0))) /
    gas_visc
    gmob_mid = relativeperm_gas(0.5 * (Sw[0:(N-1)] + Sw[1:N])) / gas_visc
    gmob_bnd = np.append(gmob_up, gmob_mid)
    q_gas_bnd = - gmob_bnd * abs_perm * excess_dP_dz_gas

    #lower boundary condition for gas
    #calculate water pressure gradient at bottom
    wmob_down = relativeperm_water(Sw_bot) / water_visc
    dpw_dz_bot = q_water_inflowbot / (wmob_down * abs_perm) + water_dens * g
    #approximate gas density at lower boundary
    dcappres_dz_bot = 2 * (capillary_pres(Sw_bot) - capillary_pres(Sw[-1])) /
    dz
    dpg_dz_bot = dpw_dz_bot + dcappres_dz_bot
    pg_bot = pg[-1] + dpg_dz_bot * 0.5 * dz
    gas_dens_bot = gas_density(pg_bot)
    #calculate bottom gas flux
    gmob_down = relativeperm_gas(Sw_bot) / gas_visc
    q_gas_down = -gmob_down * abs_perm * (dpg_dz_bot - gas_dens_bot * g)

    return(np.append(q_water_bnd, -q_water_inflowbot), np.append(q_gas_bnd,
    q_gas_down), \
           gas_dens, np.append(gas_dens_bnd, gas_dens_bot))

#model formulation
def model(statevars, t, debug = False):
    #read in state variables
    pw = statevars[0:N] #pressure
    Sw = statevars[N:(2*N)] #water_saturation

    #calculate density * Darcy velocity for both phases
    dummy = FV_Darcyflow(pw, Sw, t)
    q_water = dummy[0]
    q_gas = dummy[1]
    gas_dens = dummy[2]
    gas_dens_bnd = dummy[3]

    #calculate temporal derivative for phase saturations
    dSw_dt = - (1/por) * (q_water[1:(N+1)] - q_water[0:N]) / dz
    dSg_dt = - dSw_dt

    #multiply gas Darcy velocity by gas density
    gas_mass_flux = q_gas * gas_dens_bnd
```

```
    #calculate gas mass flux divergence
    gas_div = (gas_mass_flux[1:(N+1)] - gas_mass_flux[0:N]) / dz

    #calculate change in gas pressure
    dpg_dt = - (gas_div + por*gas_dens*dSg_dt) / (por * (1 - Sw) *
    compressibility)

    #calculate change in capillary pressure
    dpcap_dt = dcapillary_pres_dsaturation(Sw) * dSw_dt

    #calculate change in water pressure
    dpw_dt = dpg_dt - dpcap_dt

    #for troubleshooting
    if (debug == True):
        pdb.set_trace()

    return np.concatenate([dpw_dt, dSw_dt])

#caller for lsoda integrator
def solution(statevars_init, t):
    sol = odeint(model, statevars_init, t, mxstep = 10000,
            full_output = 1, atol = 1e-6, rtol = 1e-6, hmax = 60.0)
    return sol

#stencil
L = 10.0 #length domain [m]
N =  50 #number of nodes
dz = L / N #[m]
z = (np.linspace(0, N-1, N) + 0.5) * dz #[m]

#model parameters
abs_perm = 1e-13 #[m2]
g = 9.8 #[m/s2]
water_dens = 1e3 #[kg/m3]
gas_dens_ref = 1 #[kg/m3]
water_visc = 1e-3 #[Pa s]
gas_visc = 1e-5 #[Pa s]
molecular_weight_CH4 = 16 * 1e-3 #[kg/mol]
tempK = 283 #[K]
gas_const = 8.3145 #[J/mol/K]
compressibility = molecular_weight_CH4 / (gas_const * tempK) #[s2/m2]
por = 0.8
amplitude = 0*1 #[m]
time_period = 12 * 60**2 #[s]

#lower boundary condition
```

```
q_water_inflowbot = 0.1 / (60**2*24*365) #[m/y]->[m/s] positive value for
    inflow
Sw_bot = 0.5

#initial conditons
Sw_const = Sw_bot
Sw_init = np.repeat(Sw_const, N)

wmob_down = relativeperm_water(Sw_bot) / water_visc
dpw_dz_bot = q_water_inflowbot / (wmob_down * abs_perm) + water_dens * g
pw_init = dpw_dz_bot * z

statevars_init = np.concatenate([pw_init, Sw_init])

#time settings
t_days = 1
t_end_hours = t_days * 24
t_end = t_end_hours * 60**2 #[s]
t = np.linspace(0, t_end, 2*t_end_hours+1)

#run simulation
print("Start simulation.")
sol = solution(statevars_init, t)
print("Simulation finished.")
```

Listing A.1: Model code

Appendix B

Porewater Flow Patterns: Additional Analysis[1]

B.1 Assessment of flow with random permeability fields

To verify the robustness of the observed flow patterns and to compare 2D with 3D simulations, 100 random permeability fields were generated for 5 different variances ($\sigma^2_{\log\kappa}$), ranging between 0.2 and 1.0, and for each realization the steady-state flow field was directly resolved (Fig. B.1). In line with Griffiths and Fenton (1997), the simulated upward flow velocities in the grid cells follow a log-normal distribution (Fig B.1a,b), and the variance of the upward velocities was on average in the 3D simulations slightly greater than in the 2D simulations (Fig. B.1c).

After computing the flow field for each random permeability field, the steady-state tracer distribution was simulated. Vertical tracer profiles were then extracted for each volume element at the sediment water interface and used to determine the vertical flow velocity (eq. 3.4). We then compute the variances for tracer-based vertical velocities for each realization j ($s^2_{t,j}$), as well as the variances for the column-averages of the fluid flow velocities ($s^2_{f,j}$). Finally, we average these variances across the 100 realizations, and report the ratio (Table B.1). The results show that the variance of the tracer-based velocities is smaller than the variance of the actual flow field. This is attributed to the effect of lateral diffusion on the distribution of the tracer, reducing the lateral variability in the tracer and leading to more uniform estimates of vertical flow velocities.

[1]Supplementary information in relation to chapter 3

Table B.1: Comparison of the variance in the fitted flow estimates based on tracer profiles ($\bar{s}_t^2$) to computed flow ($\bar{s}_f^2$).

$\sigma^2_{\log\kappa}$	2D: $\bar{s}_t^2/\bar{s}_f^2$	3D: $\bar{s}_t^2/\bar{s}_f^2$
0.2	0.84	0.74
0.4	0.74	0.65
0.6	0.68	0.62
0.8	0.64	0.49
1.0	0.59	0.51

B.2 Sensitivity analysis with regard to temporal evolution of the flow

The sensitivity analysis allows an assessment of the effect of various parameters on solid formation and the evolution of flow on longer timescales. The analysis was carried out in 1D. This was motivated by the shorter simulation times and the results from simulations with a flow conduit, which illustrate that the flow in the high permeability conduit evolves largely independently from that in the bulk sediment (compare dashed and dotted lines in Fig. 3.6b).

The results of the sensitivity analysis indicate that the deceleration of flow over time is sensitive to the burial velocity, the rate of anaerobic methane oxidation, and the exponent in the permeability function (eq. 3.14), but rather insensitive towards the rate constant of carbonate precipitation (Fig. B.2).

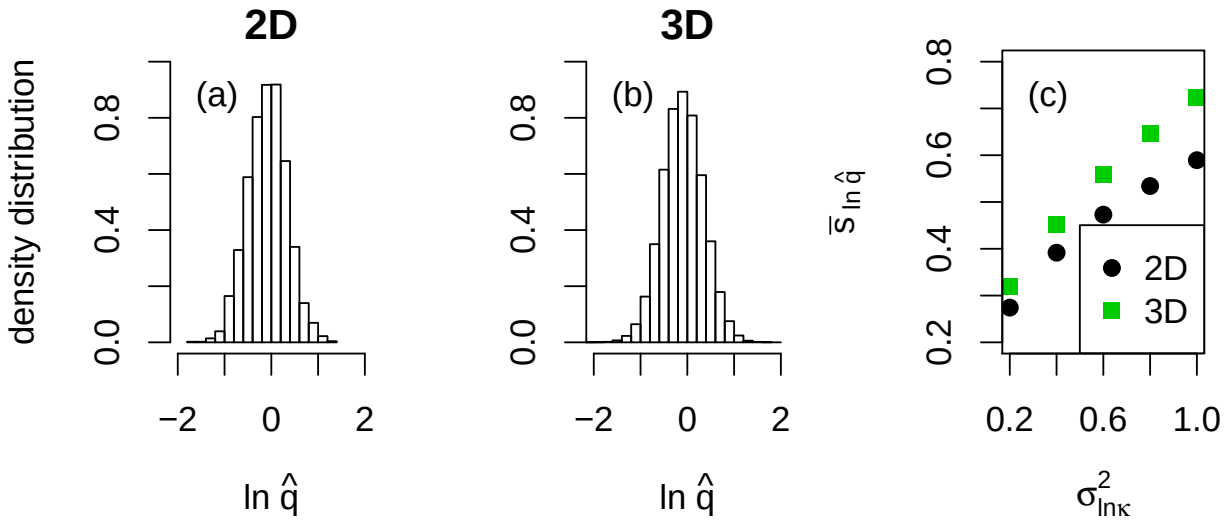

Figure B.1: Simulated steady-state flow and tracer distributions. Panels (a) and (b) show the distribution after taking the log of normalized upward velocities ($\hat{q} = q/\bar{q}$) for a 2D and a 3D simulation, respectively, with $\sigma^2_{\log \kappa}$; panel (c) shows the standard deviation corresponding to the log-normal distribution of the upward Darcy velocities, averaged over 100 generated random permeability fields.

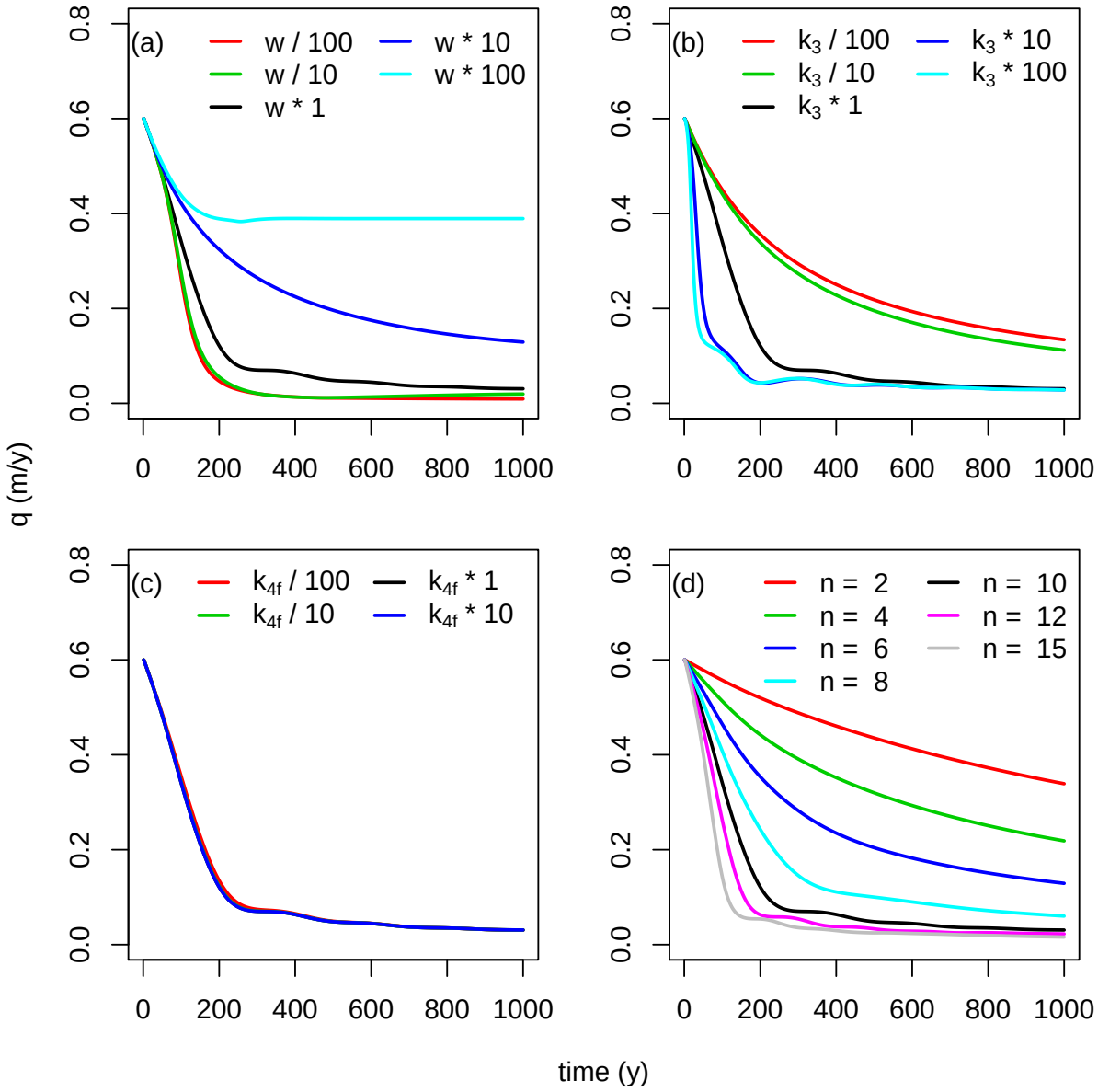

Figure B.2: Sensitivity analysis with respect to (a) the burial velocity (w, Table 3.1); (b) the rate constant of anaerobic methane oxidation (k_3); (c) the rate constant of carbonate precipitation (k_{4f}); (d) the exponent in the permeability equation (n; eq. 3.14).

Bibliography

Aharon, P. and B. Fu (2000). "Microbial sulfate reduction rates and sulfur and oxygen isotope fractionations at oil and gas seeps in deepwater Gulf of Mexico". In: *Geochimica et Cosmochimica Acta* 64.2, pp. 233–246.

Aiello, I. W., R. E. Garrison, J. C. Moore, M. Kastner, and D. S. Stakes (2001). "Anatomy and origin of carbonate structures in a Miocene cold-seep field". In: *Geology* 29.12, pp. 1111–1114.

Alcott, L. J., A. J. Krause, E. U. Hammarlund, C. J. Bjerrum, F. Scholz, Y. Xiong, A. J. Hobson, L. Neve, B. J. Mills, C. März, et al. (2020). "Development of Iron Speciation Reference Materials for Palaeoredox Analysis". In: *Geostandards and Geoanalytical Research*. DOI: 10.1111/ggr.12342.

Algar, C. K., B. P. Boudreau, and M. A. Barry (2011). "Initial rise of bubbles in cohesive sediments by a process of viscoelastic fracture". In: *Journal of Geophysical Research: Solid Earth* 116.B4.

Alkhatib, M., M. Lehmann, and P. Del Giorgio (2012). "The nitrogen isotope effect of benthic remineralization-nitrification-denitrification coupling in an estuarine environment". In: *Biogeosciences* 9, pp. 1633–1646.

Aller, R., J. Mackin, and R. Cox Jr (1986). "Diagenesis of Fe and S in Amazon inner shelf muds: apparent dominance of Fe reduction and implications for the genesis of ironstones". In: *Continental Shelf Research* 6.1-2, pp. 263–289.

Aller, R. C. (2001). "Transport and Reactions in the Bioirrigated Zone". In: *The benthic boundary layer: Transport processes and biogeochemistry*. Ed. by B. P. Boudreau and B. B. Jørgensen. Oxford University Press. Chap. 11, p. 269.

Aller, R. C. and J. Y. Aller (1998). "The effect of biogenic irrigation intensity and solute exchange on diagenetic reaction rates in marine sediments". In: *Journal of Marine Research* 56.4, pp. 905–936.

Altabet, M. A., D. W. Murray, and W. L. Prell (1999). "Climatically linked oscillations in Arabian Sea denitrification over the past 1 my: Implications for the marine N cycle". In: *Paleoceanography* 14.6, pp. 732–743.

Anschutz, P., B. Sundby, L. LEFRANcois, G. W. Luther III, and A. Mucci (2000). "Interactions between metal oxides and species of nitrogen and iodine in bioturbated marine sediments". In: *Geochimica et Cosmochimica Acta* 64.16, pp. 2751–2763.

Archer, D. and A. Devol (1992). "Benthic oxygen fluxes on the Washington shelf and slope: A comparison of in situ microelectrode and chamber flux measurements". In: *Limnology and Oceanography* 37.3, pp. 614–629.

Arndt, S., B. B. Jørgensen, D. E. LaRowe, J. Middelburg, R. Pancost, and P. Regnier (2013). "Quantifying the degradation of organic matter in marine sediments: a review and synthesis". In: *Earth-science reviews* 123, pp. 53–86.

Balslev-Clausen, D., T. W. Dahl, N. Saad, and M. T. Rosing (2013). "Precise and accurate δ 13 C analysis of rock samples using Flash Combustion–Cavity Ring Down Laser Spectroscopy". In: *Journal of Analytical Atomic Spectrometry* 28.4, pp. 516–523.

Bard, E., B. Hamelin, R. G. Fairbanks, and A. Zindler (1990). "Calibration of the 14 C timescale over the past 30,000 years using mass spectrometric U–Th ages from Barbados corals". In: *Nature* 345.6274, pp. 405–410.

Barnes, C., M. Best, F. Johnson, and B. Pirenne (2015). "NEPTUNE Canada: Installation and initial operation of the world's first regional cabled ocean observatory". In: *Seafloor Observatories*. Springer, pp. 415–438.

Bastian, P. (1999). "Numerical computation of multiphase flows in porous media". PhD thesis. Univeristät Kiel. 222 pp.

Baumann, M., S. Moran, R. Kelly, M. Lomas, and D. Shull (2013). "234Th balance and implications for seasonal particle retention in the eastern Bering Sea". In: *Deep Sea Research Part II: Topical Studies in Oceanography* 94, pp. 7–21.

Bayrakci, G., C. Scalabrin, S. Dupré, I. Leblond, J.-B. Tary, N. Lanteri, J.-M. Augustin, L. Berger, E. Cros, A. Ogor, et al. (2014). "Acoustic monitoring of gas emissions from the seafloor. Part II: a case study from the Sea of Marmara". In: *Marine Geophysical Research* 35.3, pp. 211–229.

Beal, E. J., C. H. House, and V. J. Orphan (2009). "Manganese-and iron-dependent marine methane oxidation". In: *Science* 325.5937, pp. 184–187.

Bear, J. (1972). *Dynamics of fluids in porous media*. Dover Publications, New York, NY. 764 pp.

Beiersdorf, H., H. R. Kudrass, and U. von Stackelberg (1980). "Placer deposits of ilmenite and zircon on the Zambezi shelf". In: *Geologisches Jahrbuch* D36, pp. 5–85.

Bender, M. L. (1990). "The δ18O of dissolved O2 in seawater: A unique tracer of circulation and respiration in the deep sea". In: *Journal of Geophysical Research: Oceans* 95.C12, pp. 22243–22252.

Berg, P., M. L. Delgard, R. N. Glud, M. Huettel, C. E. Reimers, and M. L. Pace (2017). "Non-invasive flux measurements at the benthic interface: The aquatic eddy covariance technique". In: *Limnology and Oceanography e-Lectures* 7.1, pp. 1–50.

Berg, P., S. Rysgaard, and B. Thamdrup (2003). "Dynamic modeling of early diagenesis and nutrient cycling. A case study in an artic marine sediment". In: *American Journal of Science* 303.10, pp. 905–955.

Bergquist, D. C., J. P. Andras, T. McNelis, S. Howlett, M. J. Van Horn, and C. R. Fisher (2003). "Succession in Gulf of Mexico cold seep vestimentiferan aggregations: the importance of spatial variability". In: *Marine Ecology* 24.1, pp. 31–44.

Berner, R. A. (1970). "Sedimentary pyrite formation". In: *American journal of science* 268.1, pp. 1–23.

— (1980). *Early diagenesis: a theoretical approach*. 1. Princeton University Press.

— (1984). "Sedimentary pyrite formation: an update". In: *Geochimica et cosmochimica Acta* 48.4, pp. 605–615.

Betts, J. and H. Holland (1991). "The oxygen content of ocean bottom waters, the burial efficiency of organic carbon, and the regulation of atmospheric oxygen". In: *Palaeogeography, Palaeoclimatology, Palaeoecology* 97.1-2, pp. 5–18.

Bianchi, D., J. P. Dunne, J. L. Sarmiento, and E. D. Galbraith (2012). "Data-based estimates of suboxia, denitrification, and N2O production in the ocean and their sensitivities to dissolved O2". In: *Global Biogeochemical Cycles* 26.2.

Blaauw, M. (2010). "Methods and code for 'classical'age-modelling of radiocarbon sequences". In: *quaternary geochronology* 5.5, pp. 512–518.

Boetius, A., K. Ravenschlag, C. J. Schubert, D. Rickert, F. Widdel, A. Gieseke, R. Amann, B. B. Jørgensen, U. Witte, and O. Pfannkuche (2000). "A marine microbial consortium apparently mediating anaerobic oxidation of methane". In: *Nature* 407.6804, pp. 623–626.

Boetius, A. and F. Wenzhöfer (2013). "Seafloor oxygen consumption fuelled by methane from cold seeps". In: *Nature Geoscience* 6.9, pp. 725–734.

Bohlen, L., A. W. Dale, and K. Wallmann (2012). "Simple transfer functions for calculating benthic fixed nitrogen losses and C: N: P regeneration ratios in global biogeochemical models". In: *Global biogeochemical cycles* 26.3.

Boles, J., J. Clark, I. Leifer, and L. Washburn (2001). "Temporal variation in natural methane seep rate due to tides, Coal Oil Point area, California". In: *Journal of Geophysical Research: Oceans* 106.C11, pp. 27077–27086.

Booij, K., W. Helder, and B. Sundby (1991). "Rapid redistribution of oxygen in a sandy sediment induced by changes in the flow velocity of the overlying water". In: *Netherlands Journal of Sea Research* 28.3, pp. 149–165.

Borowski, W. S., C. K. Paull, and W. Ussler III (1996). "Marine pore-water sulfate profiles indicate in situ methane flux from underlying gas hydrate". In: *Geology* 24.7, pp. 655–658.

Borowski, W. S., N. M. Rodriguez, C. K. Paull, and W. Ussler III (2013). "Are 34S-enriched authigenic sulfide minerals a proxy for elevated methane flux and gas hydrates in the geologic record?" In: *Marine and Petroleum Geology* 43, pp. 381–395.

Boudreau, B. P. (1994). "Is burial velocity a master parameter for bioturbation?" In: *Geochimica et Cosmochimica Acta* 58.4, pp. 1243–1249.

— (1996). "The diffusive tortuosity of fine-grained unlithified sediments". In: *Geochimica et cosmochimica acta* 60.16, pp. 3139–3142.

— (1997). *Diagenetic models and their implementation*. Vol. 410. Springer, Berlin.

— (2001). "Solute transport above the sediment-water interface". In: *The benthic boundary layer: Transport processes and biogeochemistry*. Ed. by B. P. Boudreau and B. B. Jørgensen. Oxford University Press. Chap. 5, pp. 104–126.

Boudreau, B. P., C. Algar, B. D. Johnson, I. Croudace, A. Reed, Y. Furukawa, K. M. Dorgan, P. A. Jumars, A. S. Grader, and B. S. Gardiner (2005). "Bubble growth and rise in soft sediments". In: *Geology* 33.6, pp. 517–520.

Boudreau, B. P., M. Huettel, S. Forster, R. A. Jahnke, A. McLachlan, J. J. Middelburg, P. Nielsen, F. Sansone, G. Taghon, W. Van Raaphorst, et al. (2001). "Permeable marine sediments: overturning an old paradigm". In: *EOS, Transactions American Geophysical Union* 82.11, pp. 133–136.

Bowles, M. W., J. M. Mogollón, S. Kasten, M. Zabel, and K.-U. Hinrichs (2014). "Global rates of marine sulfate reduction and implications for sub–sea-floor metabolic activities". In: *Science* 344.6186, pp. 889–891.

Boyun, G., C. William, G. Ali Ghalambor, et al. (2007). *Petroleum production engineering: a computer-assisted approach*.

Brandes, J. A. and A. H. Devol (1995). "Simultaneous nitrate and oxygen respiration in coastal sediments: evidence for discrete diagenesis". In: *Journal of Marine Research* 53.5, pp. 771–797.

— (1997). "Isotopic fractionation of oxygen and nitrogen in coastal marine sediments". In: *Geochimica et Cosmochimica Acta* 61.9, pp. 1793–1801.

— (2002). "A global marine-fixed nitrogen isotopic budget: Implications for Holocene nitrogen cycling". In: *Global biogeochemical cycles* 16.4, pp. 67–1.

Brandes, J. A., A. H. Devol, T. Yoshinari, D. Jayakumar, and S. Naqvi (1998). "Isotopic composition of nitrate in the central Arabian Sea and eastern tropical North Pacific: A tracer for mixing and nitrogen cycles". In: *Limnology and Oceanography* 43.7, pp. 1680–1689.

Briggs, K. B., P. D. Jackson, R. J. Holyer, R. C. Flint, J. Sandidge, and D. K. Young (1998). "Two-dimensional variability in porosity, density, and electrical resistivity of Eckernförde Bay sediment". In: *Continental shelf research* 18.14-15, pp. 1939–1964.

Brunner, B., S. Contreras, M. F. Lehmann, O. Matantseva, M. Rollog, T. Kalvelage, G. Klockgether, G. Lavik, M. S. Jetten, B. Kartal, et al. (2013). "Nitrogen isotope effects induced by anammox bacteria". In: *Proceedings of the National Academy of Sciences* 110.47, pp. 18994–18999.

Camoin, G., L. Montaggioni, and C. Braithwaite (2004). "Late glacial to post glacial sea levels in the Western Indian Ocean". In: *Marine Geology* 206.1-4, pp. 119–146.

Canfield, D., E. Kristensen, and B. Thamdrup (2005). *Aquatic geomicrobiology*. Elsevier.

Canfield, D. E. (1989). "Sulfate reduction and oxic respiration in marine sediments: implications for organic carbon preservation in euxinic environments". In: *Deep Sea Research Part A. Oceanographic Research Papers* 36.1, pp. 121–138.

— (1994). "Factors influencing organic carbon preservation in marine sediments". In: *Chemical geology* 114.3-4, pp. 315–329.

Canfield, D. E., R. Raiswell, J. T. Westrich, C. M. Reaves, and R. A. Berner (1986). "The use of chromium reduction in the analysis of reduced inorganic sulfur in sediments and shales". In: *Chemical geology* 54.1-2, pp. 149–155.

Cardenas, M. B., P. L. Cook, H. Jiang, and P. Traykovski (2008). "Constraining denitrification in permeable wave-influenced marine sediment using linked hydrodynamic and biogeochemical modeling". In: *Earth and Planetary Science Letters* 275.1-2, pp. 127–137.

Carpenter, E. J., H. R. Harvey, B. Fry, and D. G. Capone (1997). "Biogeochemical tracers of the marine cyanobacterium Trichodesmium". In: *Deep Sea Research Part I: Oceanographic Research Papers* 44.1, pp. 27–38.

Carstensen, J., D. J. Conley, E. Bonsdorff, B. G. Gustafsson, S. Hietanen, U. Janas, T. Jilbert, A. Maximov, A. Norkko, J. Norkko, et al. (2014). "Hypoxia in the Baltic Sea: Biogeochemical cycles, benthic fauna, and management". In: *Ambio* 43.1, pp. 26–36.

Casciotti, K. L. (2009). "Inverse kinetic isotope fractionation during bacterial nitrite oxidation". In: *Geochimica et Cosmochimica Acta* 73.7, pp. 2061–2076.

Castellini, D. G., G. R. Dickens, G. T. Snyder, and C. D. Ruppel (2006). "Barium cycling in shallow sediment above active mud volcanoes in the Gulf of Mexico". In: *Chemical Geology* 226.1-2, pp. 1–30.

Cathles, L., Z. Su, and D. Chen (2010). "The physics of gas chimney and pockmark formation, with implications for assessment of seafloor hazards and gas sequestration". In: *Marine and petroleum Geology* 27.1, pp. 82–91.

Cavagna, S., P. Clari, F. D. Pierre, L. Martire, and M. Natalicchio (2015). "Sluggish and steady focussed flows through fine-grained sediments: The methane-derived cylindrical concretions of the Tertiary Piedmont Basin (NW Italy)". In: *Marine and Petroleum Geology* 66, pp. 596–605.

Cerco, C. F. and T. Cole (1993). "Three-dimensional eutrophication model of Chesapeake Bay". In: *Journal of Environmental Engineering* 119.6, pp. 1006–1025.

Chaturvedi, E., K. Patidar, M. Srungavarapu, S. Laik, and A. Mandal (2018). "Thermodynamics and kinetics of methane hydrate formation and dissociation in presence of calcium carbonate". In: *Advanced Powder Technology* 29.4, pp. 1025–1034.

Choi, J.-H., Y. Seol, R. Boswell, and R. Juanes (2011). "X-ray computed-tomography imaging of gas migration in water-saturated sediments: From capillary invasion to conduit opening". In: *Geophysical Research Letters* 38.17.

Clark, P. U., A. S. Dyke, J. D. Shakun, A. E. Carlson, J. Clark, B. Wohlfarth, J. X. Mitrovica, S. W. Hostetler, and A. M. McCabe (2009). "The last glacial maximum". In: *science* 325.5941, pp. 710–714.

Clark, P. U., A. M. McCabe, A. C. Mix, and A. J. Weaver (2004). "Rapid rise of sea level 19,000 years ago and its global implications". In: *Science* 304.5674, pp. 1141–1144.

Clayton, C. and S. Hay (1994). "Gas migration mechanisms from accumulation to surface". In: *Bulletin of the Geological Society of Denmark* 41.1, pp. 12–23.

Clennell, M. B., A. Judd, and M. Hovland (2000). "Movement and accumulation of methane in marine sediments: relation to gas hydrate systems". In: *Natural gas hydrate*. Springer, pp. 105–122.

Contreras, S., P. Meister, B. Liu, X. Prieto-Mollar, K.-U. Hinrichs, A. Khalili, T. G. Ferdelman, M. M. Kuypers, and B. B. Jørgensen (2013). "Cyclic 100-ka (glacial-interglacial) migration of subseafloor redox zonation on the Peruvian shelf". In: *Proceedings of the National Academy of Sciences* 110.45, pp. 18098–18103.

Conway, T. M. and S. G. John (2014). "Quantification of dissolved iron sources to the North Atlantic Ocean". In: *Nature* 511.7508, pp. 212–215.

Cook, P. L., F. Wenzhöfer, S. Rysgaard, O. S. Galaktionov, F. J. Meysman, B. D. Eyre, J. Cornwell, M. Huettel, and R. N. Glud (2006). "Quantification of denitrification in permeable sediments: Insights from a two-dimensional simulation analysis and experimental data". In: *Limnology and Oceanography: Methods* 4.9, pp. 294–307.

Cordes, E. E., D. C. Bergquist, and C. R. Fisher (2009). "Macro-ecology of Gulf of Mexico cold seeps". In: *Annual Review of Marine Science* 1, pp. 143–168.

Crémière, A., A. Lepland, S. Chand, D. Sahy, D. J. Condon, S. R. Noble, T. Martma, T. Thorsnes, S. Sauer, and H. Brunstad (2016). "Timescales of methane seepage on the Norwegian margin following collapse of the Scandinavian Ice Sheet". In: *Nature communications* 7.1, pp. 1–10.

D'Andrea, A. F. and T. H. DeWitt (2009). "Geochemical ecosystem engineering by the mud shrimp Upogebia pugettensis (Crustacea: Thalassinidae) in Yaquina Bay, Oregon: Density-dependent effects on organic matter remineralization and nutrient cycling". In: *Limnology and Oceanography* 54.6, pp. 1911–1932.

Dähnke, K. and B. Thamdrup (2013). "Nitrogen isotope dynamics and fractionation during sedimentary denitrification in Boknis Eck, Baltic Sea". In: *Biogeosciences (BG)* 10.5, pp. 3079–3088.

Dale, A. W., S. Sommer, E. Ryabenko, A. Noffke, L. Bohlen, K. Wallmann, K. Stolpovsky, J. Greinert, and O. Pfannkuche (2014). "Benthic nitrogen fluxes and fractionation of

nitrate in the Mauritanian oxygen minimum zone (Eastern Tropical North Atlantic)". In: *Geochimica et Cosmochimica Acta* 134, pp. 234–256.

Davenport, E. S., D. H. Shull, and A. H. Devol (2012). "Roles of sorption and tube-dwelling benthos in the cycling of phosphorus in Bering Sea sediments". In: *Deep Sea Research Part II: Topical Studies in Oceanography* 65, pp. 163–172.

Davis, E., K. Becker, K. Wang, and B. Carson (1995). "Long-term observations of pressure and temperature in Hole 892B, Cascadia accretionary prism". In: *Proceedings of the Ocean Drilling Program. Scientific results*. Vol. 146, pp. 299–311.

Delhomme, J. (1978). "Kriging in the hydrosciences". In: *AdWR* 1.5, pp. 251–266.

Dennis Jr, J. and R. Schnabel (1983). *Numerical Methods for Unconstrained Optimization and Nonlinear Equations*. Prentice-Hall, Englewood Cliffs, NJ.

Deschamps, P., N. Durand, E. Bard, B. Hamelin, G. Camoin, A. L. Thomas, G. M. Henderson, J. Okuno, and Y. Yokoyama (2012). "Ice-sheet collapse and sea-level rise at the Bølling warming 14,600 years ago". In: *Nature* 483.7391, pp. 559–564.

Deutsch, C., D. M. Sigman, R. C. Thunell, A. N. Meckler, and G. H. Haug (2004). "Isotopic constraints on glacial/interglacial changes in the oceanic nitrogen budget". In: *Global Biogeochemical Cycles* 18.4.

Deville, E., C. Scalabrin, G. Jouet, A. Cattaneo, A. Battani, S. Noirez, H. Vermesse, K. Olu, L. Corbari, M. Boulard, et al. (2020). "Fluid seepage associated with slope destabilization along the Zambezi margin (Mozambique)". In: *Marine Geology*, p. 106275.

Di, P., D. Feng, and D. Chen (2014). "In-situ and on-line measurement of gas flux at a hydrocarbon seep from the northern South China Sea". In: *Continental shelf research* 81, pp. 80–87.

Diercks, A.-R., L. Macelloni, M. D'Emidio, S. Lucker, A. Woolsey, and M. U. Woolsey (2019). "High-resolution seismo-acoustic characterization of Green Canyon 600, a perennial hydrocarbon seep in Gulf of Mexico deep water". In: *Marine Geophysical Research* 40.3, pp. 357–370.

Dornhoffer, T., G. Waldbusser, and C. Meile (2015). "Modeling lugworm irrigation behavior effects on sediment nitrogen cycling". In: *Marine Ecology Progress Series* 534, pp. 121–134.

Duan, Z., D. Li, Y. Chen, and R. Sun (2011). "The influence of temperature, pressure, salinity and capillary force on the formation of methane hydrate". In: *Geoscience Frontiers* 2.2, pp. 125–135.

Emery, K. (1968). "Relict sediments on continental shelves of world". In: *AAPG Bulletin* 52.3, pp. 445–464.

Fairbanks, R. G. (1989). "A 17,000-year glacio-eustatic sea level record: influence of glacial melting rates on the Younger Dryas event and deep-ocean circulation". In: *Nature* 342.6250, pp. 637–642.

Felmy, A. R. and J. H. Weare (1991). "Calculation of multicomponent ionic diffusion from zero to high concentration: I. The system Na-K-Ca-Mg-Cl-SO4-H2O at 25 C". In: *Geochimica et Cosmochimica Acta* 55.1, pp. 113–131.

Fennel, K., D. Brady, D. DiToro, R. W. Fulweiler, W. S. Gardner, A. Giblin, M. J. McCarthy, A. Rao, S. Seitzinger, M. Thouvenot-Korppoo, et al. (2009). "Modeling denitrification in aquatic sediments". In: *Biogeochemistry* 93.1-2, pp. 159–178.

Fischer, D., J. M. Mogollón, M. Strasser, T. Pape, G. Bohrmann, N. Fekete, V. Spiess, and S. Kasten (2013). "Subduction zone earthquake as potential trigger of submarine hydrocarbon seepage". In: *Nature Geoscience* 6.8, pp. 647–651.

Froelich, P., G. Klinkhammer, M. L. Bender, N. Luedtke, G. R. Heath, D. Cullen, P. Dauphin, D. Hammond, B. Hartman, and V. Maynard (1979). "Early oxidation of organic matter in pelagic sediments of the eastern equatorial Atlantic: suboxic diagenesis". In: *Geochimica et cosmochimica acta* 43.7, pp. 1075–1090.

Gay, A., R. Mourgues, C. Berndt, D. Bureau, S. Planke, D. Laurent, S. Gautier, C. Lauer, and D. Loggia (2012). "Anatomy of a fluid pipe in the Norway Basin: Initiation, propagation and 3D shape". In: *Marine Geology* 332, pp. 75–88.

Germanovich, L. N., R. S. Hurt, J. E. Smith, G. Genc, and R. P. Lowell (2015). "Measuring fluid flow and heat output in seafloor hydrothermal environments". In: *Journal of Geophysical Research: Solid Earth* 120.12, pp. 8031–8055.

Glud, R. N. (2008). "Oxygen dynamics of marine sediments". In: *Marine Biology Research* 4.4, pp. 243–289.

Glud, R. N., S. Forster, and M. Huettel (1996). "Influence of radial pressure gradients on solute exchange in stirred benthic chambers". In: *Marine Ecology Progress Series* 141, pp. 303–311.

Granger, J., D. M. Sigman, M. F. Lehmann, and P. D. Tortell (2008). "Nitrogen and oxygen isotope fractionation during dissimilatory nitrate reduction by denitrifying bacteria". In: *Limnology and Oceanography* 53.6, pp. 2533–2545.

Griffiths, D. and G. A. Fenton (1997). "Three-dimensional seepage through spatially random soil". In: *Journal of geotechnical and geoenvironmental engineering* 123.2, pp. 153–160.

Groot, T. de, H. Maazallahi, T. Röckmann, S. Walter, M. Menoud, B. Meijninger, C. Mesdag, D. Rush, and H. Niemann (2019). "Tidal dynamics control microbial methane oxidation in the water column above an active cold seep (Doggerbank, North Sea)." In: *Geophysical Research Abstracts*. Vol. 21.

Grundmanis, V. and J. W. Murray (1977). "Nitrification and denitrification in marine sediments from Puget Sound 1". In: *Limnology and Oceanography* 22.5, pp. 804–813.

Gu, Y.-G., J. Ouyang, J.-J. Ning, and Z.-H. Wang (2017). "Distribution and sources of organic carbon, nitrogen and their isotopes in surface sediments from the largest mariculture zone of the eastern Guangdong coast, South China". In: *Marine Pollution Bulletin* 120.1-2, pp. 286–291.

Guo, Q., C. Wang, R. Wei, G. Zhu, M. Cui, and C. P. Okolic (2020). "Qualitative and quantitative analysis of source for organic carbon and nitrogen in sediments of rivers and lakes based on stable isotopes". In: *Ecotoxicology and Environmental Safety* 195, p. 110436.

Haas, A., J. Peckmann, M. Elvert, H. Sahling, and G. Bohrmann (2010). "Patterns of carbonate authigenesis at the Kouilou pockmarks on the Congo deep-sea fan". In: *Marine Geology* 268.1-4, pp. 129–136.

Haeckel, M., B. P. Boudreau, and K. Wallmann (2007). "Bubble-induced porewater mixing: A 3-D model for deep porewater irrigation". In: *Geochimica et Cosmochimica Acta* 71.21, pp. 5135–5154.

Haffert, L. and M. Haeckel (2019). "Quantification of non-ideal effects on diagenetic processes along extreme salinity gradients at the Mercator mud volcano in the Gulf of Cadiz". In: *Geochimica et Cosmochimica Acta* 244, pp. 366–382.

Haffert, L., M. Haeckel, V. Liebetrau, C. Berndt, C. Hensen, M. Nuzzo, A. Reitz, F. Scholz, J. Schönfeld, C. Perez-Garcia, et al. (2013). "Fluid evolution and authigenic mineral paragenesis related to salt diapirism–The Mercator mud volcano in the Gulf of Cadiz". In: *Geochimica et Cosmochimica Acta* 106, pp. 261–286.

Hagens, M. and J. J. Middelburg (2016). "Generalised expressions for the response of pH to changes in ocean chemistry". In: *Geochimica et Cosmochimica Acta* 187, pp. 334–349.

Hamersley, M. R. and B. L. Howes (2004). "Evaluation of the N2 flux approach for measuring sediment denitrification". In: *Estuarine, Coastal and Shelf Science* 62.4, pp. 711–723.

Hartmann, M. and H. Nielsen (1968). "δ 34S-Werte in rezenten Meeressedimenten und ihre Deutung am Beispiel einiger Sedimentprofile aus der westlichen Ostsee". In: *Geologische Rundschau* 58.2, pp. 621–655.

Hartnett, H. E. and A. H. Devol (2003). "Role of a strong oxygen-deficient zone in the preservation and degradation of organic matter: A carbon budget for the continental margins of northwest Mexico and Washington State". In: *Geochimica et Cosmochimica Acta* 67.2, pp. 247–264.

Henry, P., J.-P. Foucher, X. Le Pichon, M. Sibuet, K. Kobayashi, P. Tarits, N. Chamot-Rooke, T. Furuta, and P. Schultheiss (1992). "Interpretation of temperature measurements from the Kaiko-Nankai cruise: Modeling of fluid flow in clam colonies". In: *Earth and Planetary Science Letters* 109.3-4, pp. 355–371.

Henry, P., X. Le Pichon, S. Lallemant, S. Lance, J. B. Martin, J.-P. Foucher, A. Fiala-Médioni, F. Rostek, N. Guilhaumou, V. Pranal, et al. (1996). "Fluid flow in and around a mud volcano field seaward of the Barbados accretionary wedge: results from Manon cruise". In: *Journal of Geophysical Research: Solid Earth* 101.B9, pp. 20297–20323.

Hensen, C., M. Zabel, K. Pfeifer, T. Schwenk, S. Kasten, N. Riedinger, H. D. Schulz, and A. Boetius (2003). "Control of sulfate pore-water profiles by sedimentary events and the significance of anaerobic oxidation of methane for the burial of sulfur in marine sediments". In: *Geochimica et Cosmochimica Acta* 67.14, pp. 2631–2647.

Hindmarsh, A. C. (1983). "ODEPACK, a systematized collection of ODE solvers". In: *Scientific computing*, pp. 55–64.

Hindmarsh, A. C., P. N. Brown, K. E. Grant, S. L. Lee, R. Serban, D. E. Shumaker, and C. S. Woodward (2005). "SUNDIALS: Suite of nonlinear and differential/algebraic equation solvers". In: *ACM Transactions on Mathematical Software (TOMS)* 31.3, pp. 363–396.

Hofmann, A. F., K. Soetaert, J. J. Middelburg, and F. J. Meysman (2010). "AquaEnv: An Aqua tic Acid–Base Modelling Env ironment in R". In: *Aquatic Geochemistry* 16.4, pp. 507–546.

Holmkvist, L., T. G. Ferdelman, and B. B. Jørgensen (2011). "A cryptic sulfur cycle driven by iron in the methane zone of marine sediment (Aarhus Bay, Denmark)". In: *Geochimica et Cosmochimica Acta* 75.12, pp. 3581–3599.

Hovland, M. (2002). "On the self-sealing nature of marine seeps". In: *Continental Shelf Research* 22.16, pp. 2387–2394.

Hovland, M., S. Jensen, and C. Fichler (2012). "Methane and minor oil macro-seep systems—their complexity and environmental significance". In: *Marine Geology* 332, pp. 163–173.

Hüttel, M. (1990). "Influence of the lugworm Arenicola marina on porewater nutrient profiles of sand flat sediments." In: *Marine ecology progress series. Oldendorf* 62.3, pp. 241–248.

Hüttel, M., H. Røy, E. Precht, and S. Ehrenhauss (2003). "Hydrodynamical impact on biogeochemical processes in aquatic sediments". In: *The Interactions between Sediments and Water*. Springer, pp. 231–236.

Jain, A. and R. Juanes (2009). "Preferential mode of gas invasion in sediments: Grain-scale mechanistic model of coupled multiphase fluid flow and sediment mechanics". In: *Journal of Geophysical Research: Solid Earth* 114.B8.

Jakobsen, R. and D. Postma (1999). "Redox zoning, rates of sulfate reduction and interactions with Fe-reduction and methanogenesis in a shallow sandy aquifer, Rømø, Denmark". In: *Geochimica et Cosmochimica Acta* 63.1, pp. 137–151.

Janssen, F., M. Huettel, and U. Witte (2005). "Pore-water advection and solute fluxes in permeable marine sediments (II): Benthic respiration at three sandy sites with differ-

ent permeabilities (German Bight, North Sea)". In: *Limnology and Oceanography* 50.3, pp. 779–792.

Jin, Q. and C. M. Bethke (2005). "Predicting the rate of microbial respiration in geochemical environments". In: *Geochimica et Cosmochimica Acta* 69.5, pp. 1133–1143.

Johansen, C., L. Macelloni, M. Natter, M. Silva, M. Woosley, A. Woolsey, A. Diercks, J. Hill, R. Viso, E. Marty, V. Lobodin, W. Shedd, S. Joye, and I. MacDonald (2020). "Hydrocarbon migration pathway and methane budget for a Gulf of Mexico natural seep site: Green Canyon 600". In: *Earth and Planetary Science Letters* 545, p. 116411.

Johansen, C., A. C. Todd, and I. R. MacDonald (2017). "Time series video analysis of bubble release processes at natural hydrocarbon seeps in the Northern Gulf of Mexico". In: *Marine and Petroleum Geology* 82, pp. 21–34.

Johnson, B. D., B. P. Boudreau, B. S. Gardiner, and R. Maass (2002). "Mechanical response of sediments to bubble growth". In: *Marine Geology* 187.3-4, pp. 347–363.

Jones, S. and C. Jago (1993). "In situ assessment of modification of sediment properties by burrowing invertebrates". In: *Marine biology* 115.1, pp. 133–142.

Jørgensen, B. B. (1979). "A theoretical model of the stable sulfur isotope distribution in marine sediments". In: *Geochimica et Cosmochimica Acta* 43.3, pp. 363–374.

— (2000). "Bacteria and marine biogeochemistry". In: *Marine geochemistry*. Springer, pp. 173–207.

Jouet, G. and E. Deville (2015). *PAMELA-MOZ04 cruise, RV Pourquoi pas*. DOI: 10.17600/15000700.

Jourabchi, P., I. L'Heureux, C. Meile, and P. Van Cappellen (2010). "Physical and chemical steady-state compaction in deep-sea sediments: Role of mineral reactions". In: *Geochimica et Cosmochimica Acta* 74.12, pp. 3494–3513.

Joye, S. B. (2018). *Sediment geochemistry and process rate measurements collected during R/V Endeavor cruise EN559 in the northern Gulf of Mexico from 2015-05-29 to 2015-06-20*. Distributed by: Gulf of Mexico Research Initiative Information and Data Cooperative (GRIIDC), Harte Research Institute, Texas A&M University–Corpus Christi. DOI: 10.7266/N7348HG7.

Joye, S. B., A. Boetius, B. N. Orcutt, J. P. Montoya, H. N. Schulz, M. J. Erickson, and S. K. Lugo (2004). "The anaerobic oxidation of methane and sulfate reduction in sediments from Gulf of Mexico cold seeps". In: *Chemical Geology* 205.3-4, pp. 219–238.

Jung, H. and C. Meile (2019). "Upscaling of microbially driven first-order reactions in heterogeneous porous media". In: *Journal of contaminant hydrology* 224, p. 103483.

Just, J., E. Schefuß, H. Kuhlmann, J.-B. W. Stuut, and J. Pätzold (2014). "Climate induced sub-basin source-area shifts of Zambezi River sediments over the past 17 ka". In: *Palaeogeography, Palaeoclimatology, Palaeoecology* 410, pp. 190–199.

Kasten, S., T. Freudenthal, F. X. Gingele, and H. D. Schulz (1998). "Simultaneous formation of iron-rich layers at different redox boundaries in sediments of the Amazon deep-sea fan". In: *Geochimica et Cosmochimica Acta* 62.13, pp. 2253–2264.

Kasten, S., M. Zabel, V. Heuer, and C. Hensen (2003). "Processes and signals of nonsteady-state diagenesis in deep-sea sediments and their pore waters". In: *The South Atlantic in the Late Quaternary*. Springer, pp. 431–459.

Kato, S., K. Hashimoto, and K. Watanabe (2012). "Microbial interspecies electron transfer via electric currents through conductive minerals". In: *Proceedings of the National Academy of Sciences* 109.25, pp. 10042–10046.

Katsman, R. (2015). "Correlation of shape and size of methane bubbles in fine-grained muddy aquatic sediments with sediment fracture toughness". In: *Journal of Structural Geology* 70, pp. 56–64.

— (2019). "Methane bubble escape from gas horizon in muddy aquatic sediment under periodic wave loading". In: *Geophysical Research Letters* 46.12, pp. 6507–6515.

Kessler, A. J., L. A. Bristow, M. B. Cardenas, R. N. Glud, B. Thamdrup, and P. L. Cook (2014). "The isotope effect of denitrification in permeable sediments". In: *Geochimica et Cosmochimica Acta* 133, pp. 156–167.

Kessler, A. J., R. N. Glud, M. B. Cardenas, M. Larsen, M. F. Bourke, and P. L. Cook (2012). "Quantifying denitrification in rippled permeable sands through combined flume experiments and modeling". In: *Limnology and Oceanography* 57.4, pp. 1217–1232.

Kossel, E., C. Deusner, N. Bigalke, and M. Haeckel (2018). "The dependence of water permeability in quartz sand on gas hydrate saturation in the pore space". In: *Journal of Geophysical Research: Solid Earth* 123.2, pp. 1235–1251.

Kostka, J. E. and G. W. Luther III (1994). "Partitioning and speciation of solid phase iron in saltmarsh sediments". In: *Geochimica et Cosmochimica Acta* 58.7, pp. 1701–1710.

Kristensen, E. (2001). "Impact of polychaetes (Nereis spp. and Arenicola marina) on carbon biogeochemistry in coastal marine sedimentsPresented during the ACS Division of Geochemistry symposium 'Biogeochemical Consequences of Dynamic Interactions Between Benthic Fauna, Microbes and Aquatic Sediments', San Diego, April 2001." In: *Geochemical Transactions* 2.12, pp. 92–103.

Kritee, K., D. M. Sigman, J. Granger, B. B. Ward, A. Jayakumar, and C. Deutsch (2012). "Reduced isotope fractionation by denitrification under conditions relevant to the ocean". In: *Geochimica et Cosmochimica Acta* 92, pp. 243–259.

Künitzer, A., D. Basford, J. Craeymeersch, J. Dewarumez, J. Dörjes, G. Duineveld, A. Eleftheriou, C. Heip, P. Herman, P. Kingston, et al. (1992). "The benthic infauna of the North Sea: species distribution and assemblages". In: *ICES Journal of Marine Science* 49.2, pp. 127–143.

Lapham, L. L., M. Alperin, J. Chanton, and C. Martens (2008a). "Upward advection rates and methane fluxes, oxidation, and sources at two Gulf of Mexico brine seeps". In: *Marine Chemistry* 112.1-2, pp. 65–71.

Lapham, L. L., J. P. Chanton, C. S. Martens, P. D. Higley, H. W. Jannasch, and J. R. Woolsey (2008b). "Measuring temporal variability in pore-fluid chemistry to assess gas hydrate stability: development of a continuous pore-fluid array". In: *Environmental science & technology* 42.19, pp. 7368–7373.

LaRowe, D. E., A. W. Dale, D. R. Aguilera, I. L'Heureux, J. P. Amend, and P. Regnier (2014). "Modeling microbial reaction rates in a submarine hydrothermal vent chimney wall". In: *Geochimica et Cosmochimica Acta* 124, pp. 72–97.

Larson, B., J. Houghton, R. Lowell, A. Farough, and C. Meile (2015). "Subsurface conditions in hydrothermal vents inferred from diffuse flow composition, and models of reaction and transport". In: *Earth and Planetary Science Letters* 424, pp. 245–255.

Le Bars, M. and M. G. Worster (2006). "Interfacial conditions between a pure fluid and a porous medium: implications for binary alloy solidification". In: *Journal of Fluid Mechanics* 550, pp. 149–173.

Lehmann, M. F., D. M. Sigman, and W. M. Berelson (2004). "Coupling the 15N/14N and 18O/16O of nitrate as a constraint on benthic nitrogen cycling". In: *Marine Chemistry* 88.1-2, pp. 1–20.

Lehmann, M. F., D. M. Sigman, D. C. McCorkle, J. Granger, S. Hoffmann, G. Cane, and B. G. Brunelle (2007). "The distribution of nitrate 15N/14N in marine sediments and the impact of benthic nitrogen loss on the isotopic composition of oceanic nitrate". In: *Geochimica et Cosmochimica Acta* 71.22, pp. 5384–5404.

Leifer, I. (2019). "A Synthesis Review of Emissions and Fates for the Coal Oil Point Marine Hydrocarbon Seep Field and California Marine Seepage". In: *Geofluids* 2019.

Leifer, I. and J. Boles (2005). "Turbine tent measurements of marine hydrocarbon seeps on subhourly timescales". In: *Journal of Geophysical Research: Oceans* 110.C1.

Leifer, I. and K. Wilson (2004). "Quantified marine oil emissions with a video-monitored, oil seep-tent". In: *Marine Technology Society Journal* 38.3, pp. 44–53.

— (2007). "The tidal influence on oil and gas emissions from an abandoned oil well: Nearshore Summerland, California". In: *Marine pollution bulletin* 54.9, pp. 1495–1506.

Lessard-Pilon, S., M. D. Porter, E. E. Cordes, I. MacDonald, and C. R. Fisher (2010). "Community composition and temporal change at deep Gulf of Mexico cold seeps". In: *Deep Sea Research Part II: Topical Studies in Oceanography* 57.21-23, pp. 1891–1903.

Levin, L. A., A. R. Baco, D. A. Bowden, A. Colaco, E. E. Cordes, M. R. Cunha, A. W. Demopoulos, J. Gobin, B. M. Grupe, J. Le, et al. (2016). "Hydrothermal vents and methane seeps: rethinking the sphere of influence". In: *Frontiers in Marine Science* 3, p. 72.

Lie, U. (1968). "A quantitative study of benthic infauna in Puget Sound, Washington, USA, in 1963-1964". In: *Fiskeridirektoratets Skrifter (Serie Havundersøkelser)* 14, pp. 229–556.

Linke, P., O. Pfannkuche, M. Torres, R. Collier, U. Witte, J. McManus, D. Hammond, K. Brown, M. Tryon, and K.-i. Nakamura (1999). "Variability of benthic flux and discharge

rates at vent sites determined by in situ instruments". In: *EOS transactions* 80.46 Fall Meet. Suppl, F509.

Liu, L., J. Wilkinson, K. Koca, C. Buchmann, and A. Lorke (2016). "The role of sediment structure in gas bubble storage and release". In: *Journal of Geophysical Research: Biogeosciences* 121.7, pp. 1992–2005.

Liu, X. and P. Flemings (2009). "Dynamic response of oceanic hydrates to sea level drop". In: *Geophysical Research Letters* 36.17.

Lønborg, C. and M. Søndergaard (2009). "Microbial availability and degradation of dissolved organic carbon and nitrogen in two coastal areas". In: *Estuarine, Coastal and Shelf Science* 81.4, pp. 513–520.

Lowell, R. P. and L. N. Germanovich (2004). "Hydrothermal processes at mid-ocean ridges: Results from scale analysis and single-pass models". In: *GMS* 148, pp. 219–244.

Lubbe, J. H. J. L. van der, R. Tjallingii, M. A. Prins, G.-J. A. Brummer, S. J. Jung, D. Kroon, and R. R. Schneider (2014). "Sedimentation patterns off the Zambezi River over the last 20,000 years". In: *Marine Geology* 355, pp. 189–201.

Luff, R., J. Greinert, K. Wallmann, I. Klaucke, and E. Suess (2005). "Simulation of long-term feedbacks from authigenic carbonate crust formation at cold vent sites". In: *Chemical Geology* 216.1-2, pp. 157–174.

Luff, R. and K. Wallmann (2003). "Fluid flow, methane fluxes, carbonate precipitation and biogeochemical turnover in gas hydrate-bearing sediments at Hydrate Ridge, Cascadia Margin: numerical modeling and mass balances". In: *Geochimica et Cosmochimica Acta* 67.18, pp. 3403–3421.

MacDonald, I., N. Guinasso Jr, R. Sassen, J. Brooks, L. Lee, and K. Scott (1994). "Gas hydrate that breaches the sea floor on the continental slope of the Gulf of Mexico". In: *Geology* 22.8, pp. 699–702.

Malinverno, A. (2010). "Marine gas hydrates in thin sand layers that soak up microbial methane". In: *Earth and Planetary Science Letters* 292.3-4, pp. 399–408.

Mariotti, A., J. Germon, P. Hubert, P. Kaiser, R. Letolle, A. Tardieux, and P. Tardieux (1981). "Experimental determination of nitrogen kinetic isotope fractionation: some prin-

ciples; illustration for the denitrification and nitrification processes". In: *Plant and soil* 62.3, pp. 413–430.

Martens, C. S. and R. A. Berner (1977). "Interstitial water chemistry of anoxic Long Island Sound sediments. 1. Dissolved gases 1". In: *Limnology and Oceanography* 22.1, pp. 10–25.

Martens, C. S. and J. V. Klump (1984). "Biogeochemical cycling in an organic-rich coastal marine basin 4. An organic carbon budget for sediments dominated by sulfate reduction and methanogenesis". In: *Geochimica et Cosmochimica Acta* 48.10, pp. 1987–2004.

Martens, C. S., H. P. Mendlovitz, H. Seim, L. Lapham, and M. D'Emidio (2016). "Sustained in situ measurements of dissolved oxygen, methane and water transport processes in the benthic boundary layer at MC118, northern Gulf of Mexico". In: *Deep Sea Research Part II: Topical Studies in Oceanography* 129, pp. 41–52.

Martin, J. H., G. A. Knauer, D. M. Karl, and W. W. Broenkow (1987). "VERTEX: carbon cycling in the northeast Pacific." In: *Deep-Sea Research* 34.2, pp. 267–285.

März, C., J. Hoffmann, U. Bleil, G. J. de Lange, and S. Kasten (2008). "Diagenetic changes of magnetic and geochemical signals by anaerobic methane oxidation in sediments of the Zambezi deep-sea fan (SW Indian Ocean)". In: *Marine Geology* 255.3-4, pp. 118–130.

März, C., N. Riedinger, C. Sena, and S. Kasten (2018). "Phosphorus dynamics around the sulphate-methane transition in continental margin sediments: Authigenic apatite and Fe (II) phosphates". In: *Marine Geology* 404, pp. 84–96.

Meile, C., K. Tuncay, and P. Van Cappellen (2003). "Explicit representation of spatial heterogeneity in reactive transport models: application to bioirrigated sediments". In: *Journal of Geochemical Exploration* 78, pp. 231–234.

Meile, C. and P. V. Cappellen (2003). "Global estimates of enhanced solute transport in marine sediments". In: *Limnology and Oceanography* 48.2, pp. 777–786.

Meile, C., C. M. Koretsky, and P. Van Cappellen (2001). "Quantifying bioirrigation in aquatic sediments: an inverse modeling approach". In: *Limnology and oceanography* 46.1, pp. 164–177.

Meysman, F. J. R., B. P. Boudreau, and J. J. Middelburg (2005a). "Modeling reactive transport in sediments subject to bioturbation and compaction". In: *Geochimica et Cosmochimica Acta* 69.14, pp. 3601–3617.

Meysman, F. J. R., O. S. Galaktionov, and J. J. Middelburg (2005b). "Irrigation patterns in permeable sediments induced by burrow ventilation: a case study of Arenicola marina". In: *Marine Ecology Progress Series* 303, pp. 195–212.

Meysman, F. J. R., J. J. Middelburg, and C. H. R. Heip (2006a). "Bioturbation: a fresh look at Darwin's last idea". In: *Trends in Ecology & Evolution* 21.12, pp. 688–695.

Meysman, F. J., O. S. Galaktionov, B. Gribsholt, and J. J. Middelburg (2006b). "Bioirrigation in permeable sediments: Advective pore-water transport induced by burrow ventilation". In: *Limnology and Oceanography* 51.1, pp. 142–156.

Meysman, F. J., N. Risgaard-Petersen, S. Y. Malkin, and L. P. Nielsen (2015). "The geochemical fingerprint of microbial long-distance electron transport in the seafloor". In: *Geochimica et Cosmochimica Acta* 152, pp. 122–142.

Middelburg, J. J., K. Soetaert, and P. M. J. Herman (1997). "Empirical relationships for use in global diagenetic models". In: *Deep Sea Research Part I: Oceanographic Research Papers* 44.2, pp. 327–344.

Middelburg, J. J., K. Soetaert, P. M. J. Herman, and C. H. R. Heip (1996). "Denitrification in marine sediments: A model study". In: *Global Biogeochemical Cycles* 10.4, pp. 661–673. DOI: 10.1029/96GB02562.

Mikolaj, P. G. and J. P. Ampaya (1973). "Tidal effects on the activity of natural submarine oil seeps". In: *Mar. Technol. Soc. J* 7, pp. 25–28.

Minagawa, M. and E. Wada (1986). "Nitrogen isotope ratios of red tide organisms in the East China Sea: a characterization of biological nitrogen fixation". In: *Marine chemistry* 19.3, pp. 245–259.

Mogollón, J. M., I. L'Heureux, A. W. Dale, and P. Regnier (2009). "Methane gas-phase dynamics in marine sediments: A model study". In: *American Journal of Science* 309.3, pp. 189–220.

Montoya, J. (2015). *R/V Endeavor: EN559 Hydrographic (CTD) Data, Gulf of Mexico, May 29, 2015 to June 21, 2015*. Distributed by: Gulf of Mexico Research Initiative Information and Data Cooperative (GRIIDC), Harte Research Institute, Texas A&M University–Corpus Christi. DOI: 10.7266/N7PV6HQ4.

Montoya, J. P. (2008). "Nitrogen stable isotopes in marine environments". In: *Nitrogen in the marine environment*. Ed. by D. G. Capone, D. A. Bronk, M. R. Mulholland, and E. J. Carpenter. Elsevier. Chap. 29, pp. 1277–1302.

Moore, W. S. (1976). "Sampling 228Ra in the deep ocean". In: *Deep Sea Research and Oceanographic Abstracts*. Vol. 23. 7. Elsevier, pp. 647–651.

Müller, P. J. and E. Suess (1979). "Productivity, sedimentation rate, and sedimentary organic matter in the oceans—I. Organic carbon preservation". In: *Deep Sea Research Part A. Oceanographic Research Papers* 26.12, pp. 1347–1362.

Mulsow, S., B. P. Boudreau, and J. A. Smith (1998). "Bioturbation and porosity gradients". In: *Limnology and Oceanography* 43.1, pp. 1–9.

Na, T., B. Gribsholt, O. S. Galaktionov, T. Lee, and F. J. Meysman (2008). "Influence of advective bio-irrigation on carbon and nitrogen cycling in sandy sediments". In: *Journal of Marine Research* 66.5, pp. 691–722.

National Research Council (2003). *Oil in the sea III: inputs, fates, and effects*. National Academies Press (US).

Nauhaus, K., A. Boetius, M. Krüger, and F. Widdel (2002). "In vitro demonstration of anaerobic oxidation of methane coupled to sulphate reduction in sediment from a marine gas hydrate area". In: *Environmental microbiology* 4.5, pp. 296–305.

Nichols, F. H. (2003). "Interdecadal change in the deep Puget Sound benthos". In: *Hydrobiologia* 493.1-3, pp. 95–114.

Niemann, H., P. Linke, K. Knittel, E. MacPherson, A. Boetius, W. Brückmann, G. Larvik, K. Wallmann, U. Schacht, E. Omoregie, et al. (2013). "Methane-carbon flow into the benthic food web at cold seeps–a case study from the Costa Rica subduction zone". In: *PLoS One* 8.10, e74894.

Niewöhner, C., C. Hensen, S. Kasten, M. Zabel, and H. Schulz (1998). "Deep sulfate reduction completely mediated by anaerobic methane oxidation in sediments of the upwelling area off Namibia". In: *Geochimica et cosmochimica acta* 62.3, pp. 455–464.

NOAA (2020). *NOAA Tides & Currents*. URL: `tidesandcurrents.noaa.gov`. Visited on 07/18/2020.

O'Hara, S., P. Dando, U. Schuster, A. Bennis, J. Boyle, F. Chui, T. Hatherell, S. Niven, and L. Taylor (1995). "Gas seep induced interstitial water circulation: observations and environmental implications". In: *Continental Shelf Research* 15.8, pp. 931–948.

Omlin, M., R. Brun, and P. Reichert (2001). "Biogeochemical model of Lake Zürich: sensitivity, identifiability and uncertainty analysis". In: *Ecological Modelling* 141.1-3, pp. 105–123.

Orcutt, B. N., L. L. Lapham, J. Delaney, N. Sarode, K. S. Marshall, K. J. Whaley-Martin, G. Slater, C. G. Wheat, and P. R. Girguis (2017). "Microbial response to oil enrichment in Gulf of Mexico sediment measured using a novel long-term benthic lander system". In: *Elem Sci Anth* 5.

Oueslati, W., S. Van de Velde, M. A. Helali, A. Added, L. Aleya, and F. J. Meysman (2019). "Carbon, iron and sulphur cycling in the sediments of a Mediterranean lagoon (Ghar El Melh, Tunisia)". In: *Estuarine, Coastal and Shelf Science* 221, pp. 156–169.

Palastanga, V., C. Slomp, and C. Heinze (2011). "Long-term controls on ocean phosphorus and oxygen in a global biogeochemical model". In: *Global Biogeochemical Cycles* 25.3.

Pallud, C. and P. Van Cappellen (2006). "Kinetics of microbial sulfate reduction in estuarine sediments". In: *Geochimica et Cosmochimica Acta* 70.5, pp. 1148–1162.

Pastor, L., B. Deflandre, E. Viollier, C. Cathalot, E. Metzger, C. Rabouille, K. Escoubeyrou, E. Lloret, A. M. Pruski, G. Vétion, et al. (2011). "Influence of the organic matter composition on benthic oxygen demand in the Rhône River prodelta (NW Mediterranean Sea)". In: *Continental Shelf Research* 31.9, pp. 1008–1019.

Pastor, L., C. Rabouille, E. Metzger, A. T. de Chanvalon, E. Viollier, and B. Deflandre (2018). "Transient early diagenetic processes in Rhône prodelta sediments revealed in contrasting flood events". In: *Continental Shelf Research* 166, pp. 65–76.

Paull, C. K., B. Hecker, R. Commeau, R. Freeman-Lynde, C. Neumann, W. Corso, S. Golubic, J. Hook, E. Sikes, and J. Curray (1984). "Biological communities at the Florida Escarpment resemble hydrothermal vent taxa". In: *Science* 226.4677, pp. 965–967.

Pebesma, E. J. (2004). "Multivariable geostatistics in S: the gstat package". In: *Computers & geosciences* 30.7, pp. 683–691.

Peltier, W. and R. G. Fairbanks (2006). "Global glacial ice volume and Last Glacial Maximum duration from an extended Barbados sea level record". In: *Quaternary Science Reviews* 25.23-24, pp. 3322–3337.

Peterson, L. E. (2019). "Evaluating Fluid Fluxes From Deep-Sea Seepage Habitats". PhD thesis. Coastal Carolina University. 221 pp.

Peterson, R. N., W. C. Burnett, N. Dimova, and I. R. Santos (2009). "Comparison of measurement methods for radium-226 on manganese-fiber". In: *Limnology and Oceanography: Methods* 7.2, pp. 196–205.

Pfeffer, C., S. Larsen, J. Song, M. Dong, F. Besenbacher, R. L. Meyer, K. U. Kjeldsen, L. Schreiber, Y. A. Gorby, M. Y. El-Naggar, et al. (2012). "Filamentous bacteria transport electrons over centimetre distances". In: *Nature* 491.7423, pp. 218–221.

Polerecky, L., U. Franke, U. Werner, B. Grunwald, and D. de Beer (2005). "High spatial resolution measurement of oxygen consumption rates in permeable sediments". In: *Limnology and Oceanography: Methods* 3.2, pp. 75–85.

Postma, D. and R. Jakobsen (1996). "Redox zonation: equilibrium constraints on the Fe (III)/SO4-reduction interface". In: *Geochimica et Cosmochimica Acta* 60.17, pp. 3169–3175.

Ramsay, P. J. and J. A. G. Cooper (2002). "Late Quaternary sea-level change in South Africa". In: *Quaternary Research* 57.1, pp. 82–90.

Reeburgh, W. S. (1980). "Anaerobic methane oxidation: rate depth distributions in Skan Bay sediments". In: *Earth and Planetary Science Letters* 47.3, pp. 345–352.

Reed, A. H., K. B. Briggs, and D. L. Lavoie (2002). "Porometric properties of siliciclastic marine sand: A comparison of traditional laboratory measurements with image analysis

and effective medium modeling". In: *IEEE journal of oceanic engineering* 27.3, pp. 581–592.

Reed, D. C., C. P. Slomp, and B. G. Gustafsson (2011). "Sedimentary phosphorus dynamics and the evolution of bottom-water hypoxia: A coupled benthic–pelagic model of a coastal system". In: *Limnology and Oceanography* 56.3, pp. 1075–1092.

Regnier, P., A. W. Dale, S. Arndt, D. LaRowe, J. Mogollón, and P. Van Cappellen (2011). "Quantitative analysis of anaerobic oxidation of methane (AOM) in marine sediments: a modeling perspective". In: *Earth-Science Reviews* 106.1-2, pp. 105–130.

Reimer, P. J., E. Bard, A. Bayliss, J. W. Beck, P. G. Blackwell, C. B. Ramsey, C. E. Buck, H. Cheng, R. L. Edwards, M. Friedrich, et al. (2013). "IntCal13 and Marine13 radiocarbon age calibration curves 0–50,000 years cal BP". In: *Radiocarbon* 55.4, pp. 1869–1887.

Reimer, P. J. and R. W. Reimer (2001). "A marine reservoir correction database and on-line interface". In: *Radiocarbon* 43.2A, pp. 461–463.

Reitze, M. and U. Schöttler (1989). "The time dependence of adaption to reduced salinity in the lugworm Arenicola marina L.(Annelida: Polychaeta)". In: *Comparative Biochemistry and Physiology Part A: Physiology* 93.3, pp. 549–559.

Rickard, D. (2012). *Sulfidic sediments and sedimentary rocks*. Newnes.

Riedinger, N., K. Pfeifer, S. Kasten, J. F. L. Garming, C. Vogt, and C. Hensen (2005). "Diagenetic alteration of magnetic signals by anaerobic oxidation of methane related to a change in sedimentation rate". In: *Geochimica et Cosmochimica Acta* 69.16, pp. 4117–4126.

Riisgard, H. and G. Banta (1998). "Irrigation and deposit feeding by the lugworm Arenicola marina, characteristics and secondary effects on the environment. A review of current knowledge". In: *Vie et milieu* 48.4, pp. 243–258.

Roberts, A. P. (2015). "Magnetic mineral diagenesis". In: *Earth-Science Reviews* 151, pp. 1–47.

Roberts, H. H. and P. Aharon (1994). "Hydrocarbon-derived carbonate buildups of the northern Gulf of Mexico continental slope: a review of submersible investigations". In: *Geo-Marine Letters* 14.2-3, pp. 135–148.

Roberts, H. H. and R. S. Carney (1997). "Evidence of episodic fluid, gas, and sediment venting on the northern Gulf of Mexico continental slope". In: *Economic Geology* 92.7-8, pp. 863–879.

Rocha, C. (2008). "Sandy sediments as active biogeochemical reactors: compound cycling in the fast lane". In: *Aquatic Microbial Ecology* 53.1, pp. 119–127.

Römer, M., M. Riedel, M. Scherwath, M. Heesemann, and G. D. Spence (2016). "Tidally controlled gas bubble emissions: A comprehensive study using long-term monitoring data from the NEPTUNE cabled observatory offshore Vancouver Island". In: *Geochemistry, Geophysics, Geosystems* 17.9, pp. 3797–3814.

Rooze, J. and C. Meile (2016). "The effect of redox conditions and bioirrigation on nitrogen isotope fractionation in marine sediments". In: *Geochimica et Cosmochimica Acta* 184, pp. 227–239.

Rooze, J., M. Zindorf, C. März, G. Jouet, R. Newton, C. Brandily, and L. Pastor (submitted). "The Evolution of Early Diagenetic Processes and Signatures During the Last Glacial-Interglacial Climate Transition at the Mozambique Margin". In: *Geochimica et Cosmochimica Acta*.

Rooze, J., M. Egger, I. Tsandev, and C. P. Slomp (2016). "Iron-dependent anaerobic oxidation of methane in coastal surface sediments: Potential controls and impact". In: *Limnology and Oceanography* 61.S1, S267–S282.

Rooze, J., L. Peterson, R. N. Peterson, and C. Meile (2020). "Porewater flow patterns in surficial cold seep sediments inferred from conservative tracer profiles and early diagenetic modeling". In: *Chemical Geology* 536, p. 119468.

Rosenberry, D. O., P. H. Glaser, and D. I. Siegel (2006). "The hydrology of northern peatlands as affected by biogenic gas: current developments and research needs". In: *Hydrological Processes* 20.17, pp. 3601–3610.

Ryan, W., S. Carbotte, J. Coplan, S. O'Hara, A. Melkonian, R. Arko, R. Weissel, V. Ferrini, A. Goodwillie, F. Nitsche, J. Bonczkowski, and R. Zemsky (2009). "Global Multi Resolution Topography Synthesis". In: *Geochemistry, Geophysics, Geosystems* 10.Q03014, p. 9.

Saltelli, A. (1999). "Sensitivity analysis: Could better methods be used?" In: *Journal of Geophysical Research: Atmospheres* 104.D3, pp. 3789–3793.

Santos, I. R., B. D. Eyre, and M. Huettel (2012). "The driving forces of porewater and groundwater flow in permeable coastal sediments: A review". In: *Estuarine, Coastal and Shelf Science* 98, pp. 1–15.

Sarmiento, J. L. and N. Gruber (2006). *Ocean biogeochemical dynamics*. Princeton University Press.

Sarradin, P.-M. and J.-C. Caprais (1996). "Analysis of dissolved gases by headspace sampling gas chromatography with column and detector switching. Preliminary results". In: *Analytical Communications* 33.10, pp. 371–373.

Sassen, R., H. H. Roberts, R. Carney, A. V. Milkov, D. A. DeFreitas, B. Lanoil, and C. Zhang (2004). "Free hydrocarbon gas, gas hydrate, and authigenic minerals in chemosynthetic communities of the northern Gulf of Mexico continental slope: relation to microbial processes". In: *Chemical Geology* 205.3-4, pp. 195–217.

Scandella, B. P., C. Varadharajan, H. F. Hemond, C. Ruppel, and R. Juanes (2011). "A conduit dilation model of methane venting from lake sediments". In: *Geophysical Research Letters* 38.6.

Scandella, B. P. (2010). "Numerical modeling of methane venting from lake sediments". MA thesis. Massachusetts Institute of Technology.

Schefuß, E., H. Kuhlmann, G. Mollenhauer, M. Prange, and J. Pätzold (2011). "Forcing of wet phases in southeast Africa over the past 17,000 years". In: *Nature* 480.7378, pp. 509–512.

Schlitzer, R. (2015). *Ocean data view*.

Schnabel, R. B., J. E. Koonatz, and B. E. Weiss (1985). "A modular system of algorithms for unconstrained minimization". In: *ACM Transactions on Mathematical Software (TOMS)* 11.4, pp. 419–440.

Schoell, M. (1980). "The hydrogen and carbon isotopic composition of methane from natural gases of various origins". In: *Geochimica et Cosmochimica Acta* 44.5, pp. 649–661.

Schulz, H., A. Lückge, K.-C. Emeis, and A. Mackensen (2011). "Variability of Holocene to Late Pleistocene Zambezi riverine sedimentation at the upper continental slope off Mozambique, 15–21 S". In: *Marine Geology* 286.1-4, pp. 21–34.

Schumann, K., M. Stipp, J. H. Behrmann, D. Klaeschen, and D. Schulte-Kortnack (2014). "P and S wave velocity measurements of water-rich sediments from the Nankai Trough, Japan". In: *Journal of Geophysical Research: Solid Earth* 119.2, pp. 787–805.

Shearer, G., J. D. Schneider, and D. H. Kohl (1991). "Separating the efflux and influx components of net nitrate uptake by Synechococcus R2 under steady-state conditions". In: *Journal of General Microbiology* 137.5, pp. 1179–1184.

Shum, K. (1992). "Wave-induced advective transport below a rippled water-sediment interface". In: *Journal of Geophysical Research: Oceans* 97.C1, pp. 789–808.

Sigman, D. M., R. Robinson, A. Knapp, A. Van Geen, D. McCorkle, J. Brandes, and R. Thunell (2003). "Distinguishing between water column and sedimentary denitrification in the Santa Barbara Basin using the stable isotopes of nitrate". In: *Geochemistry, Geophysics, Geosystems* 4.5.

Sirhan, S. T., R. Katsman, and M. Lazar (2019). "Methane bubble ascent within fine-grained cohesive aquatic sediments: dynamics and controlling factors". In: *Environmental science & technology* 53.11, pp. 6320–6329.

Smith, A. J., P. B. Flemings, and P. M. Fulton (2014). "Hydrocarbon flux from natural deepwater Gulf of Mexico vents". In: *Earth and Planetary Science Letters* 395, pp. 241–253.

Soetaert, K., T. Petzoldt, and F. Meysman (2016). *marelac: Tools for aquatic sciences. R package version 2.1. 6.*

Soetaert, K., P. M. Herman, and J. J. Middelburg (1996). "A model of early diagenetic processes from the shelf to abyssal depths". In: *Geochim. Cosmochim. Acta* 60.6, pp. 1019–1040.

Soetaert, K., A. F. Hofmann, J. J. Middelburg, F. J. Meysman, and J. Greenwood (2007). "Reprint of "The effect of biogeochemical processes on pH"". In: *Marine Chemistry* 106.1-2, pp. 380–401.

Soetaert, K. and F. Meysman (2012). "Reactive transport in aquatic ecosystems: Rapid model prototyping in the open source software R". In: *Environmental Modelling & Software* 32, pp. 49–60.

Soetaert, K., T. Petzoldt, et al. (2010). "Inverse modelling, sensitivity and Monte Carlo analysis in R using package FME". In: *Journal of Statistical Software* 33.3, pp. 1–28.

Soetaert, K., T. Petzoldt, and F. Meysman (2010). *Marelac: Tools for aquatic sciences.*

Solomon, E. A., M. Kastner, H. Jannasch, G. Robertson, and Y. Weinstein (2008). "Dynamic fluid flow and chemical fluxes associated with a seafloor gas hydrate deposit on the northern Gulf of Mexico slope". In: *Earth and Planetary Science Letters* 270.1-2, pp. 95–105.

Somes, C. J., A. Oschlies, and A. Schmittner (2013). "Isotopic constraints on the pre-industrial oceanic nitrogen budget". In: *Biogeosciences* 10, pp. 5889–5910.

Sommer, S., O. Pfannkuche, P. Linke, R. Luff, J. Greinert, M. Drews, S. Gubsch, M. Pieper, M. Poser, and T. Viergutz (2006). "Efficiency of the benthic filter: Biological control of the emission of dissolved methane from sediments containing shallow gas hydrates at Hydrate Ridge". In: *Global Biogeochemical Cycles* 20.2.

Southon, J., M. Kashgarian, M. Fontugne, B. Metivier, and W. W. Yim (2002). "Marine reservoir corrections for the Indian Ocean and Southeast Asia". In: *Radiocarbon* 44.1, pp. 167–180.

Steefel, C. I. and K. T. MacQuarrie (1996). *Approaches to modeling of reactive transport in porous media.* Ed. by P. C. Lichtner, C. I. Steefel, and E. H. Oelkers. Reviews in Mineralogy and Geochemistry. De Gruyter. Chap. 2, pp. 83–130. DOI: 10.1515/9781501509797.

Steefel, C., C. Appelo, B. Arora, D. Jacques, T. Kalbacher, O. Kolditz, V. Lagneau, P. Lichtner, K. U. Mayer, J. Meeussen, et al. (2015). "Reactive transport codes for subsurface environmental simulation". In: *Computational Geosciences* 19.3, pp. 445–478.

Stief, P. (2013). "Stimulation of microbial nitrogen cycling in aquatic ecosystems by benthic macrofauna: mechanisms and environmental implications." In: *Biogeosciences* 10.12.

Stockdale, A., W. Davison, and H. Zhang (2009). "Micro-scale biogeochemical heterogeneity in sediments: a review of available technology and observed evidence". In: *Earth-Science Reviews* 92.1-2, pp. 81–97.

Stüeken, E. E., M. A. Kipp, M. C. Koehler, and R. Buick (2016). "The evolution of Earth's biogeochemical nitrogen cycle". In: *Earth-Science Reviews* 160, pp. 220–239.

Suess, E. (2010). "Marine cold seeps". In: *Handbook of hydrocarbon and lipid microbiology*.

Sun, Q., S. Wu, J. Cartwright, and D. Dong (2012). "Shallow gas and focused fluid flow systems in the Pearl River Mouth Basin, northern South China Sea". In: *Marine Geology* 315, pp. 1–14.

Sun, Y. and T. Torgersen (1998). "The effects of water content and Mn-fiber surface conditions on 224Ra measurement by 220Rn emanation". In: *Marine Chemistry* 62.3-4, pp. 299–306.

Taillefert, M., J. S. Beckler, C. Cathalot, P. Michalopoulos, R. Corvaisier, N. Kiriazis, J.-C. Caprais, L. Pastor, and C. Rabouille (2017). "Early diagenesis in the sediments of the Congo deep-sea fan dominated by massive terrigenous deposits: part II–iron–sulfur coupling". In: *Deep Sea Research Part II: Topical Studies in Oceanography* 142, pp. 151–166.

Talukder, A. R. (2012). "Review of submarine cold seep plumbing systems: leakage to seepage and venting". In: *Terra Nova* 24.4, pp. 255–272.

Teichert, B., A. Eisenhauer, G. Bohrmann, A. Haase-Schramm, B. Bock, and P. Linke (2003). "U/Th systematics and ages of authigenic carbonates from Hydrate Ridge, Cascadia Margin: recorders of fluid flow variations". In: *Geochimica et Cosmochimica Acta* 67.20, pp. 3845–3857.

Thullner, M., A. W. Dale, and P. Regnier (2009). "Global-scale quantification of mineralization pathways in marine sediments: A reaction-transport modeling approach". In: *Geochemistry, Geophysics, Geosystems* 10.10.

Torres, M. E., K. Brown, R. W. Collier, M. deAngelis, D. Hammond, J. McManus, G. Rehder, and A. Trehu (1998). "Geochemical observations on Hydrate Ridge, Cascadia Margin during R/V BROWN-ROPOS cruise: August 1998". In:

Tréhu, A. M., P. E. Long, M. E. Torres, G. Bohrmann, F. R. Rack, T. S. Collett, D. S. Goldberg, A. V. Milkov, M. Riedel, P. Schultheiss, et al. (2004). "Three-dimensional distribution of gas hydrate beneath southern Hydrate Ridge: constraints from ODP Leg 204". In: *Earth and Planetary Science Letters* 222.3-4, pp. 845–862.

Treude, T., A. Boetius, K. Knittel, K. Wallmann, and B. B. Jørgensen (2003). "Anaerobic oxidation of methane above gas hydrates at Hydrate Ridge, NE Pacific Ocean". In: *Marine Ecology Progress Series* 264, pp. 1–14.

Treude, T., S. Krause, J. Maltby, A. W. Dale, R. Coffin, and L. J. Hamdan (2014). "Sulfate reduction and methane oxidation activity below the sulfate-methane transition zone in Alaskan Beaufort Sea continental margin sediments: Implications for deep sulfur cycling". In: *Geochimica et Cosmochimica Acta* 144, pp. 217–237.

Tryon, M., K. Brown, and M. Torres (2002). "Fluid and chemical flux in and out of sediments hosting methane hydrate deposits on Hydrate Ridge, OR, II: Hydrological processes". In: *Earth and Planetary Science Letters* 201.3-4, pp. 541–557.

Tryon, M. D. and K. M. Brown (2001). "Complex flow patterns through Hydrate Ridge and their impact on seep biota". In: *Geophysical Research Letters* 28.14, pp. 2863–2866.

— (2004). "Fluid and chemical cycling at Bush Hill: Implications for gas-and hydrate-rich environments". In: *Geochemistry, Geophysics, Geosystems* 5.12.

Tryon, M. D., K. M. Brown, M. E. Torres, A. M. Tréhu, J. McManus, and R. W. Collier (1999). "Measurements of transience and downward fluid flow near episodic methane gas vents, Hydrate Ridge, Cascadia". In: *Geology* 27.12, pp. 1075–1078.

Van Cappellen, P. and Y. Wang (1995). "Metal Cycling in Surface Sediments: Modeling the Interplay of Transport and Reaction". In: *Metal Speciation and Contamination of Aquatic Sediments*. Ed. by H. E. Allen. CRC Press, pp. 21–64.

— (1996). "Cycling of iron and manganese in surface sediments; a general theory for the coupled transport and reaction of carbon, oxygen, nitrogen, sulfur, iron, and manganese". In: *American Journal of Science* 296.3, pp. 197–243.

Van der Kamp, G. and J. Gale (1983). "Theory of earth tide and barometric effects in porous formations with compressible grains". In: *Water Resources Research* 19.2, pp. 538–544.

Van Kessel, T. and W. Van Kesteren (2002). "Gas production and transport in artificial sludge depots". In: *Waste Management* 22.1, pp. 19–28.

Vanderborght, J.-P., I. M. Folmer, D. R. Aguilera, T. Uhrenholdt, and P. Regnier (2007). "Reactive-transport modelling of C, N, and O2 in a river–estuarine–coastal zone system: Application to the Scheldt estuary". In: *Marine chemistry* 106.1-2, pp. 92–110.

Vanneste, H., B. A. Kelly-Gerreyn, D. P. Connelly, R. H. James, M. Haeckel, R. E. Fisher, K. Heeschen, and R. A. Mills (2011). "Spatial variation in fluid flow and geochemical fluxes across the sediment–seawater interface at the Carlos Ribeiro mud volcano (Gulf of Cadiz)". In: *Geochimica et Cosmochimica Acta* 75.4, pp. 1124–1144.

Versteeg, H. K. and W. Malalasekera (2007). *An introduction to computational fluid dynamics: the finite volume method*. Pearson education.

Volkenborn, N., S. Hedtkamp, J. Van Beusekom, and K. Reise (2007). "Effects of bioturbation and bioirrigation by lugworms (Arenicola marina) on physical and chemical sediment properties and implications for intertidal habitat succession". In: *Estuarine, Coastal and Shelf Science* 74.1-2, pp. 331–343.

Volkenborn, N., C. Meile, L. Polerecky, C. A. Pilditch, A. Norkko, J. Norkko, J. E. Hewitt, S. F. Thrush, D. S. Wethey, and S. A. Woodin (2012). "Intermittent bioirrigation and oxygen dynamics in permeable sediments: an experimental and modeling study of three tellinid bivalves". In: *Journal of Marine Research* 70.6, pp. 794–823.

Volkenborn, N., L. Polerecky, D. S. Wethey, and S. Woodin (2010). "Oscillatory porewater bioadvection in marine sediments induced by hydraulic activities of Arenicola marina". In: *Limnology and oceanography* 55.3, pp. 1231–1247.

Walford, H., N. White, and J. Sydow (2005). "Solid sediment load history of the Zambezi Delta". In: *Earth and Planetary Science Letters* 238.1-2, pp. 49–63.

Wang, K. and E. E. Davis (1996). "Theory for the propagation of tidally induced pore pressure variations in layered subseafloor formations". In: *Journal of Geophysical Research: Solid Earth* 101.B5, pp. 11483–11495.

Wang, K., E. E. Davis, and G. van der Kamp (1998). "Theory for the effects of free gas in subsea formations on tidal pore pressure variations and seafloor displacements". In: *Journal of Geophysical Research: Solid Earth* 103.B6, pp. 12339–12353.

Wang, Y. and P. Van Cappellen (1996). "A multicomponent reactive transport model of early diagenesis: Application to redox cycling in coastal marine sediments". In: *Geochimica et Cosmochimica Acta* 60.16, pp. 2993–3014.

Wellman, R., F. Cook, and H. Krouse (1968). "Nitrogen-15: microbiological alteration of abundance". In: *Science* 161.3838, pp. 269–270.

Wenau, S., B. Preu, and V. Spiess (2020). "Geological development of the Limpopo Shelf (southern Mozambique) during the last sealevel cycle". In: *Geo-Marine Letters*, pp. 1–15.

Whiticar, M. J. (1999). "Carbon and hydrogen isotope systematics of bacterial formation and oxidation of methane". In: *Chemical Geology* 161.1-3, pp. 291–314.

Wiggins, S. M., I. Leifer, P. Linke, and J. A. Hildebrand (2015). "Long-term acoustic monitoring at North Sea well site 22/4b". In: *Marine and Petroleum Geology* 68, pp. 776–788.

Woerther, P., J. Bourillet, G. Damy, L. Dussud, and N. Sultan (2012). "Improving in piston coring quality with acceleration and pressure measurements and new insights on quality of the recovery". In: *Proceedings 8th International Marine Technicians Symposium*. Vol. 25.

Xiao, K.-Q., F. Beulig, H. Røy, B. B. Jørgensen, and N. Risgaard-Petersen (2018). "Methylotrophic methanogenesis fuels cryptic methane cycling in marine surface sediment". In: *Limnology and Oceanography* 63.4, pp. 1519–1527.

Zhang, Y., J.-P. Henriet, J. Bursens, and N. Boon (2010). "Stimulation of in vitro anaerobic oxidation of methane rate in a continuous high-pressure bioreactor". In: *Bioresource Technology* 101.9, pp. 3132–3138.

Zhuang, G.-C., A. Montgomery, R. J. Sibert, M.-K. Rogener, V. A. Samarkin, and S. B. Joye (2018). "Effects of pressure, methane concentration, sulfate reduction activity, and temperature on methane production in surface sediments of the Gulf of Mexico". In: *Limnology and Oceanography* 63.5, pp. 2080–2092.

Zindorf, M., C. März, T. Wagner, S. P. Gulick, H. Strauss, J. Benowitz, J. Jaeger, B. Schnetger, L. Childress, L. LeVay, et al. (2019). "Deep Sulfate-Methane-Transition and sediment diagenesis in the Gulf of Alaska (IODP Site U1417)". In: *Marine Geology* 417, p. 105986.